DETECTION OF HYDROGEN EMBRITTLEMENT IN STEEL AND STEEL ALLOYS USING METHODS OF NEUTRON RADIOGRAPHY

by

ANDREW STEPHEN BARRITT

Dipl. Maschineningenieur
Eidgenössische Technische Hochschule, Zürich, Switzerland
(1987)

SUBMITTED TO THE DEPARTMENT OF
NUCLEAR ENGINEERING IN PARTIAL FULFILLMENT OF
THE REQUIREMENT FOR THE DEGREE OF

MASTER OF SCIENCE IN NUCLEAR ENGINEERING

at the

MASSACHUSETTS INSTITUTE OF TECHNOLOGY
January, 1994

Signature of Author _____
Department of Nuclear Engineering
January, 1994

Certified by _____
Dr. Richard C. Lanza
Thesis Supervisor
Principle Research Scientist, Department of Nuclear Engineering

Certified by _____
Kent F. Hansen
Thesis Reader
Professor, Department of Nuclear Engineering

Accepted by _____
Allan F. Henry, Chairman
Department of Nuclear Engineering Graduate Committee

DETECTION OF HYDROGEN EMBRITTLEMENT IN STEEL AND STEEL ALLOYS USING METHODS OF NEUTRON RADIOGRAPHY

by

ANDREW STEPHEN BARRITT

Submitted to the Department of Nuclear Engineering on January 14, 1994, in partial fulfillment of the requirements for the degree of Master of Science in Nuclear Engineering.

ABSTRACT

A theoretical study of a thermal neutron radiography system for non-destructive testing of steel pipes as used in power plants was carried out. The system uses a neutron detecting scintillator screen and a cooled CCD-camera connected to a small computer as imaging devices. All components of the system are described by a set of equations representing the physical and optical properties. The equations are incorporated into a computer spreadsheet program to model the system. The input parameters are varied to check for the correctness of the model and to supply the basis for modifications. The influence of dark, readout and system noise is studied. The modeled equipment represents a Princeton Instruments, Inc. camera with a EEV 1152 x 1242 pixel CCD-chip and a ST-138 controller.

The results from the modeling show that due to the large dynamic range and very low noise levels, hydrogen can be detected in the inside wall of a steel pipe. The limit for spatial resolution without accounting for scattering effects is about 100 μm, for the detection of hydrogen between 50 to 100 ppm. Contrast resolution is dependent on the exposure time but reaches a limit at approximately 0.5 % of the mass attenuation coefficient for very long exposures. When scattering effects are taken into account, the contrast resolution is reduced by a factor g_s, which is dependent on the type of material and the thickness. For the model case, g_s reduces contrast resolution considerably (Order of magnitude: 100 x), so that improvements to the original system are indicated. These include, but are not limited to, an optimized object-scintillator-CCD geometry, scattering grids and the use of a cold neutron source.

The sources available at this time for thermal neutrons are either not powerful enough or too bulky to be of any use for a system for the testing of non-removable steel pipes in a power plant. This means that the system will not be useful in the proposed task until long and cost-intensive development further development of sources has taken place. On the other hand, the assessment of steel pipes in a power plant constitutes only a very small

part of non-destructive testing of materials. Therefore, the described system has many other applications where the large dynamic range, high spatial resolution and low noise levels can be fully utilized.

Thesis Supervisor: Dr. Richard C. Lanza
Title: Principle Research Scientist, Nuclear Engineering

ACKNOWLEDGMENTS

here to pursue a Masters Degree. I hope the knowledge I have gained here will help the plant to continue operating in a safe and efficient manner for a long time.

I am grateful for the friends I encountered in fellow students here at MIT. It makes life easier and much more pleasant if one has good friends to talk to when problems arise or just to share views about politics, economics or life in general. Life would be boring without you!

Last but not least I would like to thank my family. My wife Vera for being kind and understanding when I did not have the time to be an attentive husband and for making our apartment in Arlington a home I always liked to return to. My son Patrick for being a friendly, joyful and healthy little boy and sleeping through the night since he has been 2½ months old! Furthermore, my parents, for our family that gave me the character development and support to pursue my dreams. It is only when one gets to be a father oneself that one can really start to realize all the support given by the parents.

TABLE OF CONTENTS

LIST OF ILLUSTRATIONS

Figure   Page

LIST OF TABLES

LIST OF ABBREVIATIONS

#p:	Total number of pixels on CCD-chip
A/D:	Analog to Digital
A:	Mass number
A_i:	Image area on scintillator screen
B:	Background photon flux
bcc:	Body-centered cubic
BWR:	Boiling Water Reactor
CCD:	Charge Coupled Device
D:	Dark noise
D_{min}:	Minimum distance of two points in object plane
ε_d:	Detection efficiency of the scintillator screen
EEV:	English Electric Valve Company
ε_l:	Lens efficiency
ε_q:	Quantum efficiency of CCD-chip
F:	F-number, aperture of an optical lens
f:	Focal length of an optical lens
f:	Fraction of hydrogen
fcc:	Face-centered cubic
g_s:	Scattering factor
H_i:	Image height
H_o:	Object height
IGSCC:	Inter-Granular Stress Corrosion Cracking
L:	Light capture fraction

LP:	Line-pair
L_{pixel}:	Pixel size
μ:	Attenuation coefficient
m:	Minification
MPP:	Multi-Pinned Phase
μ_{res}:	Resulting mass attenuation coefficient for steel containing hydrogen
n:	Number of atoms per unit volume
N_0:	Source flux
N_c:	Number of photons incident on CCD per neutron
N_d:	Neutrons detected by scintillator screen
NDT:	Non-Destructive Testing
N_e:	Signal at output of CCD-chip
N_γ:	Transformation factor of scintillator screen
$N_i(x)$:	Attenuated neutron flux
n_0:	Avogadro's number
N_r:	Readout noise
p:	Distance object to lens
p:	Fraction of hydrogen in ppm
P:	Photon flux incident on CCD-chip
PI:	Princeton Instruments, Inc.
ppm:	Parts per million
PWR:	Pressurized Water Reactor
q:	Image distance
ρ:	Density
r0:	Inside radius of a pipe
r1:	Radius of hydrogen loading in a pipe wall

r2:	Outside radius of a pipe
$\sigma(t)$:	Total noise of imaging system
SBIG:	Santa Barbara Instrument Group, Inc.
SCC:	Stress Corrosion Cracking
SEM:	Scanning Electron Microscope
σ_e:	Total noise of system measured in electrons
σ_n:	Total noise of imaging system measured in neutrons
SNR:	Signal To Noise Ratio
σ_t:	Total cross-section
t:	time
TI:	Texas Instruments, Inc.
y:	Length of attenuation of neutron beam in pipe wall
Z:	Atomic number

CHAPTER 1

INTRODUCTION

1.1 Statement of Problem

Degradation of construction materials by environmental attack is a concern for any operator of engineered systems made of metals. The most obvious form is rusting of iron or steel due to the exposure to air and moisture. Other forms of environmentally assisted degradation of metals are connected with the formation of hydrogen compounds or the inclusion of hydrogen in atomic form into the micro structure of the metal itself. Examples of this are hydrates, hydrogen embrittlement and closely related, intergranular stress corrosion cracking. Due to the nature of these processes, visible inspection of a component may not give any indication of the degradation, a potential weakness in a structure can go unnoticed.

A non-destructive testing method for components susceptible to hydrogen-related degradation is needed. Neutron Radiography, based on the significantly larger mass attenuation coefficient of hydrogen in comparison to the attenuation coefficients of the base metal, has been proposed and used. One example is the inspection of aluminum aircraft components to find corrosion products which contain large amounts of hydrogen. For iron and steel, hydrogen embrittlement and stress corrosion cracking are the main concern, though formation of hydrogen compounds in larger cracks (e.g. H_2S) can also be troublesome.

Many of the components tested with neutron radiography are parts of aircraft, therefore of light construction with small wall thicknesses. Due to the physical-metallurgical properties and price of steel, components tend to be more massive and whole structures

larger. Examples are the piping and vessels in chemical processing and power plants. Often, single components cannot be dismantled for non-destructive testing and have to be inspected in situ. For this, a transportable, for political and institutional reasons preferably non-nuclear neutron source and test equipment has to be used.

Under these aspects a system for testing steel pipes, has to be given a detailed evaluation. Fields of interest are the attenuation of the neutron-flux on traversing the pipe walls, spatial and physical-metallurgical resolution as well as detection, visualization and evaluation of results using a CCD-camera and computer-based system.

1.2 Approach

The major emphasis of this investigation is to evaluate a CCD-camera based system for its suitability as an instrument for non-destructive testing of steel components for hydrogen embrittlement. The necessary background for detection of hydrogen in metals using methods of neutron radiography is surveyed. A general view at who would be interested in the results of such testing and at some earlier experiments is taken. The metallurgical background of hydrogen in metals is surveyed to find a basis for the form and amount of hydrogen to be expected. A detailed description of the system to be used includes a general view at the physics involved to be able to model the system for a computer simulation. This simulation is utilized to study the response of the system to various internal and external parameters. Parallel to this, some preliminary work is undertaken to prepare for practical experiments which will be used to validate the results of the computer simulation and evaluate system performance. Specific CCD-camera systems by various manufacturers are compared and some tested in short practical experiments. A specific system is then chosen which is the most suitable to the task. Recommendations for future neutron radiography experiments using the chosen CCD-camera system are given.

The work and tasks done in the course of this investigation are described in the following pages, which have been subdivided into 7 chapters and an appendix. Chapter 1 is this introduction. In chapter 2, the background information on problems caused by hydrogen and recent experiments on hydrogen detection are described. In chapter 3 the whole proposed detection system, its possibilities and limitations are outlined. Chapter 4 contains a computer model of the system and studies the influences of various system parameters. The chapter 5 gives information on preliminary experiments, practical components of the system and planned experiments. In chapter 6, the results of chapter 3 and 4 are analyzed and discussed. The final chapter gives conclusions based on the finding and recommendations s for further study.

CHAPTER 2

BACKGROUND

2.1 Areas of Degradation of Structures by Hydrogen

The degradation of construction materials by environmental influences is a great concern to any designer, builder and operator of structures made of metals. The damages can take on a multitude of forms and express themselves as a loss in reliability, a reduction in safety or increased costs due to additional maintenance, higher down time or replacement of failed components. A classical example is the rusting of iron which causes thousands of motor vehicles to be taken out of service every year while other mechanical components might still be in usable working order.

The reduction of a material's physical abilities by hydrogen is less obvious and hardly perceived by the general public. The reduced optical obviousness results in greater operational uncertainty and higher effort for detection.

At least three phenomenological different mechanisms can be attributed to the degradation of a material in which hydrogen plays an important role:

a.) Surface corrosion with formation of hydrogen-compounds (e.g. Aluminum)

b.) Stress corrosion cracking, where an anodic dissolution with formation of hydrogen occurs along the crack ($Metal^+ + H_2O \rightarrow Metal\text{-}OH + H^+$). Example: SCC near welds in early BWR piping.

c.) Hydrogen embrittlement with the reduction of the ductility of a metal by hydrogen atoms or molecules in the granular structure of the material.

The distinction between b.) and c.) is not evident and is causing a large amount of discussion in the Materials Sciences [[1], [2]]. A subform of a.) is also found in systems where hydrates or hydrogen-compounds form in existing surface imperfections like small cracks and pits and cause growth of these imperfections through surface processes. Often all three mechanisms are present on one structure and a clear distinction can not be easily made. For the operator the actual process involved is not of primary concern, his interest lies much more in the initial detection and the extent of the degradation. In a secondary step the mechanism becomes important, when countermeasures have to be developed.

In the following, some examples are described, and the implications for the operation of the structure are given:

- Civil aircraft: Corrosion through hydrate formation of the surfaces between two bonded or riveted aluminum plates. The stability of the connection is decreased, the structure is weakened. High loading on the structure may cause it to fail prematurely. FAA regulations require the airline to take the aircraft out of service until necessary repairs have been undertaken.

- Military aircraft: On modern combat aircraft, bonding of surfaces is becoming more and more frequent. Composite materials and/or mixed structures (Plates and honeycomb) are in widespread use. Ingress of moisture or condensation causes corrosion and separation of layers, leading to a weakening of the structure. High g-loading during aerial combat or carrier starts and landings can lead to

---

[1]Latanision R.M., Gastine O.H., Compeau C.R. Stress Corrosion Cracking and Hydrogen Embrittlement: Differences and Similarities. Proceedings of the Symposium on Environment Sensitive Fracture of Engineering Materials, Fall AIME Meeting, 24-26 October 1977.

[2]Parkins R.N. Current Understanding of Stress-Corrosion Cracking. Journal of Metals. December 1992

catastrophic failure, disrupting the mission. Detection of degradation at an early stage is crucial to enable effective repairs.

- Shipbuilding, Crude Oil transportation by "Supertanker": The most obvious form of environmental attack on a sea-going vessel is rusting. Quite apart from this, operators of supertankers also face problems with Stress Corrosion Cracking and hydrogen embrittlement. SCC occurs in the heat affected zone around welds, while hydrogen embrittlement can occur anywhere in the structure. Loss of ductility due to embrittlement seriously impairs the capability of the ship to absorb the loads of a rough sea or a large swell. As these large vessels can not ride the waves, they flex quite considerably in a rough sea. This flexibility is given by the design and type of steel used. Hydrogen embrittlement can therefore lead to the breaking of parts of the structure with catastrophic results to the environment and profit margins of the ships owner.

- Petrochemical Industry: Large refineries contain hundreds of miles of pipes and a multitude of reaction vessels. These can contain hydrocarbon-compounds at high temperature and pressure. This combination of the transported fluid and physical properties makes the materials used for construction very susceptible to any form of degradation by hydrogen. The pipes are often very long and due to temperature and pressure changes have to posses a certain degree of flexibility. A brittle region in a pipe is thus a potential breaking point. Pipe breaks can lead to large production losses, the bursting of a reaction vessel has the potential for serious risk to life and the environment. A fast, reliable way of testing the pipes would help to secure operations and allow the timely replacement of degraded components. A factor to be considered for neutron radiography is that the fluid transported has a high hydrogen content. This may be limiting for resolution purposes, on the other hand it may help to detect cracks and/or internal breaks.

- Power plants (Nuclear and fossil-fueled): Similar to the example above, a multitude of pipes are used to transport fluids at various temperatures and pressures (e.g. hot water under high pressure, superheated steam under high pressure and cold water under low pressure). Additionally, in nuclear power plants, these pipes are one of the barriers between fission products in the primary coolant system and the environment. Internal and external forces act on these pipes during operation, so they need to display a certain elasticity/ductility to cope with these forces. Hydrogen embrittlement can be caused by dissociation of the water/steam or, in a smaller extent, by H_2-gas dissolved in the water (e.g. adding H_2 to bind O_2 in BWR to fight IGSCC). Detecting degraded lengths of piping before damage occurs is not only an operational consideration, but also an important issue for nuclear safety. In this application, the type of neutron source used (i.e. nuclear or non-nuclear) is of smaller importance, all the same, a "non-nuclear" source would facilitate operations. Difficulties for NDT of these pipes by neutron radiography are the thermal insulation often found on the outer diameter and general accessibility.

2.2 Other Areas of Interest for Detection of Hydrogen

There is not only a metallurgical interest in detecting hydrogen and hydrogen-compounds with neutron radiography. Other areas of science can also use this technology to facilitate operations. Some examples are:

- Detection of various levels of moisture and water in drilling cores. This would be useful for site characterization plans for repositories for radioactive waste. Another use might be the measurement of diffusion/water flow through a rock sample to evaluate porosity.

- Detection of oil in drilling cores. This is similar to the above idea, oil companies could use this technology to evaluate sites for their suitability for future exploitation.

- Testing of manufacturing processes for compound materials, like Aluminum-Carbonfiber mixtures. The inclusion of the carbonfiber array into the compound plate could be visualized and manufacturing defects found. Carbon and aluminum have mass attenuation coefficients which are different by about one order of magnitude. Even though the difference is smaller than in the hydrogen-steel system, it can be sufficient for such testing.

- Detection of explosives, for example in air baggage. Explosives are organic compounds, one of the main elements is hydrogen. This is a much more specific method to search for bombs than X-rays, as these can only give density differences helping to find specific geometries. The main problem here is that baggage usually is filled with organics, which makes detection difficult. A solution to this is to search for nitrogen, which is the usual signature for explosives. Nitrogen can be detected with fast neutron technology by measuring the characteristic (gamma) radiation resulting from inelastic collisions. Considerable research is going into this field and some systems are in operation. Detailed information is classified.

2.3 Two Examples of Recent Research

a.)A multi-dimensional tomographic imaging device for non-destructive testing of materials and complex assemblies was built and operated. The results are described in [3]. The function of a simple system involving a reactor neutron

---

[3] McFarland E.W., Lanza R.C., Poulos G.W. Multi-Dimensional Neutron-Computed Tomography Using Cooled Charge-Coupled Devices. IEEE Transactions on Nuclear Science. April 1991, Vol. 38, Number 2.

source, an object handling device, a scintillator screen detector and a CCD-imaging system was tested under various conditions. Limits on spatial resolution where found to be in the 100 μm section in small samples.

With these experiments, the basic feasibility of a system using a CCD-camera could be shown. A great advantage over film-based methods is an increase in the dynamic range by a factor of at least 100. This factor can be increased by further development of the system and the use of better components.

b.)Detection of corrosion on aircraft components and hydrogen ingress on Zircalloy fuel cladding tubes by neutron radiography. For these experiments [4], cold neutrons were used which enhance the differences in the attenuation coefficients between aluminum and hydrogen giving higher sensitivity. The experiments were done to quantify the detection capabilities of a subthermal neutrons system and looked at corroded aluminum aircraft components. Also, for nuclear power applications, zircalloy tubes were examined. The imaging system utilized was a gadolinium screen with single coated X-ray film. Excellent results were achieved even with the limited dynamic range of this system on the corroded aircraft components in detecting surface, subsurface and pit corrosion. With the zircalloy tube, neutron radiography showed hydrogen ingress into the inside of the tube. Various loadings of hydrogen could be detected when compared to a calibrated reference object. This part of these experiments constitute an important starting point for the investigations of this thesis.

---

4 Leeflang H.P., Markgraf J.F.W., Detection of Corrosion on Aircraft Components by Neutron Radiography. Proceedings of the Fourth World Conference on Neutron Radiography, May 1992, San Francisco (in press).

CHAPTER 3

SYSTEM DESCRIPTION

3.1 Theory of the Attenuation of a Neutron Beam

The physics involved in the process of visualizing hydrogen in steel components by neutron-beams are simplified to where they are relevant for the modeling of the system. The probability of occurrence of a nuclear reaction between the incident neutron and the atoms of the object is expressed in terms of the concept of cross-sections. For these observations, the total cross-section of an element is used. The total cross-section, σ_t, is mainly a function of the element (Atomic Number), the isotope (Mass Number) and the energy of the incident neutron. The neutrons used here are in the thermal, respectively. cold energy range, i.e. the energies are smaller than 0.025 eV. The total cross-section for an element was found by experiments. Many of these cross-sections have been compiled at BNL (Brookhaven National Laboratory) in a series off handbooks of neutron cross-sections, commonly known as " Barn-books " (Named after the unit for neutron cross-sections. 1 barn = 10^{-24} cm^2).

A beam of neutrons passing through a material interacts with the atoms in the material:
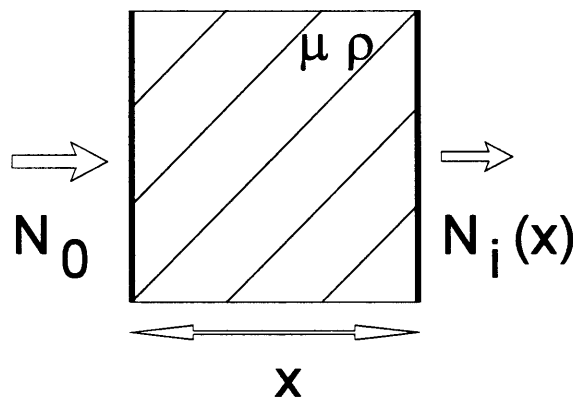
Figure 1. Neutron beam passing through uniform material

$$N_i(x) = N_0 \, e^{-\mu x} \qquad\qquad\qquad (3.1)$$

N_0: Source neutron flux [n/cm^2s]; $N_i(x)$: Neutron flux after passing through x [n/cm^2s]

μ: Linear attenuation coefficient [cm^{-1}]; x : thickness of object [cm]

The linear attenuation coefficient can be expressed as:

$$\mu = n \, Z \, \sigma_t \qquad\qquad\qquad (3.2)$$

n : Number of atoms per unit volume [$\#$ / cm^3]; Z : Atomic number; σ_t : Total cross-section [cm^2]

More often, the mass attenuation coefficient is given, as n is rarely known and has to be calculated:

$$\mu / \rho = n \, Z \, \sigma_t / \rho = (n_o \, \rho / A) (Z / \rho) \sigma_t = n_o (Z / A) \sigma_t \qquad\qquad (3.3)$$

ρ: density [g / cm^3]; n_o : Avogadro's number [$mole^{-1}$]   A : Mass number

Introduction of the mass attenuation coefficient in Eqn. (3.1):

$$N_i(x) = N_0 \, e^{-\mu \, x \, \rho} \qquad\qquad (3.4)$$

This form makes accounting for various material properties in the x-direction easier.

Assuming we have an object with two different material properties in the x-direction:
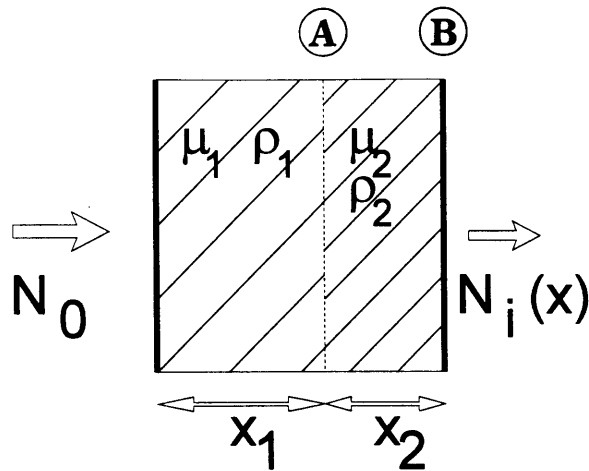
Figure 2. Neutron beam passing through an object with two regions with differing properties.

At position A: $N_i(x_1) = N_0 \, e^{-\mu_1 \, \rho_1 \, x_1}$ (3.5)

At position B: $N_i(x) = N_i(x_1 + x_2) = N_i(x_1) \, e^{-\mu_2 \, \rho_2 \, x_2}$ (3.6)

Insert (3.5) into (3.6):

$$N_i(x) = (\, N_0 \, e^{-\mu_1 \, \rho_1 \, x_1} \,) \, e^{-\mu_2 \, \rho_2 \, x_2} = N_0 \, e^{-(\mu_1 \, \rho_1 \, x_1 \, + \, \mu_2 \, \rho_2 \, x_2)}$$ (3.7)

With this form, varying material properties along the path of the neutron beam can be treated.

This effect is what is used to try to detect hydrogen in steel components. Looking at the graph .n appendix C, it can be seen that the mass attenuation coefficient for thermal neutrons of H is several orders of magnitude higher than the value for Fe (or Al). Assuming that the change of the density of steel due to the inclusion of hydrogen is negligible, the following situation presents itself if part of a steel object contains hydrogen:
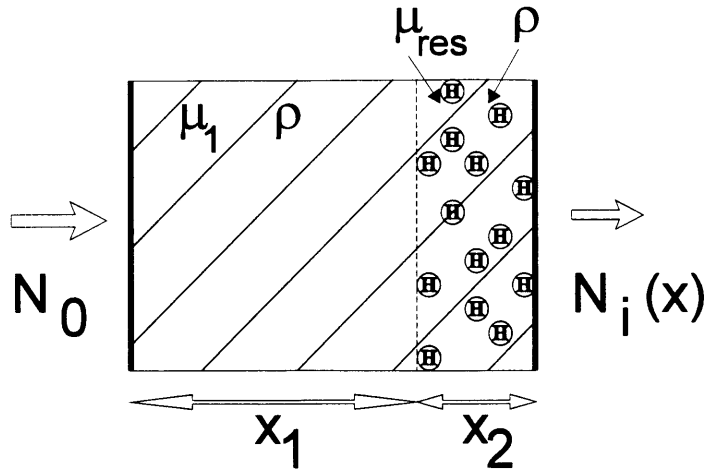
Figure 3. Neutron beam passing through an object containing hydrogen.

Region 1: Pure steel, contains no hydrogen. Density ρ.

Region 2: Steel with small amount of hydrogen. Density ρ.

Inserting given values into eqn. (3.7) gives:

$$N_i(x) = N_0 \, e^{-(\mu_1 \, \rho \, x_1 + \mu_2 \, \rho \, x_2)} = N_0 \, e^{-\rho \, (\mu_1 \, x_1 + \mu_2 \, x_2)} \qquad (3.8)$$

The mass attenuation coefficient for region 1 is simply the coefficient for the pure metal. The attenuation coefficient for region 2 is made up out of two parts. For future reference, μ_2 for cases of hydrogen in steel will be called μ_{res}.

Assuming that a fraction of the volume of the steel has been replaced by hydrogen, one can write:

$$\mu_2 = \mu_{res} = \mu_1 \, (1 - f) + \mu_H \, f \qquad (3.10)$$

f : fraction of hydrogen; μ_H : Mass attenuation coefficient of hydrogen [cm^2 / $_g$]

As hydrogen is only present in small amounts, f would be a small numerical value. For this reason, the expression of p for ppm of hydrogen is introduced.

$$p = 10^6 \, f \qquad\qquad\qquad p : \text{fraction of H in ppm}$$

Substituting this into eqn. (3.10):

$$\mu_{res} = \mu_1 \, (1 - p/\,10^6) + \mu_H \, (p\,/\,10^6) \qquad\qquad (\,3.11\,)$$

Eqn. (3.11) into (3.8):

$$N_i(x) = N_0 \, e^{-p} \, [\, \mu_1 \, x_1 + \{\mu_1 \, (1 - p\,/\,10^6) + \mu_H \, (p\,/\,10^6)\} \, x_2 \,] \qquad\qquad (\,3.12\,)$$

3.2 General description of the System

The proposed system for the detection of hydrogen in steel consists of the following sub-systems:

    a.) Neutron source with collimating device.

    b.) Object

    c.) Neutron detection unit

    d.) Optical system

    e.) Data acquisition, evaluation and visualization system.
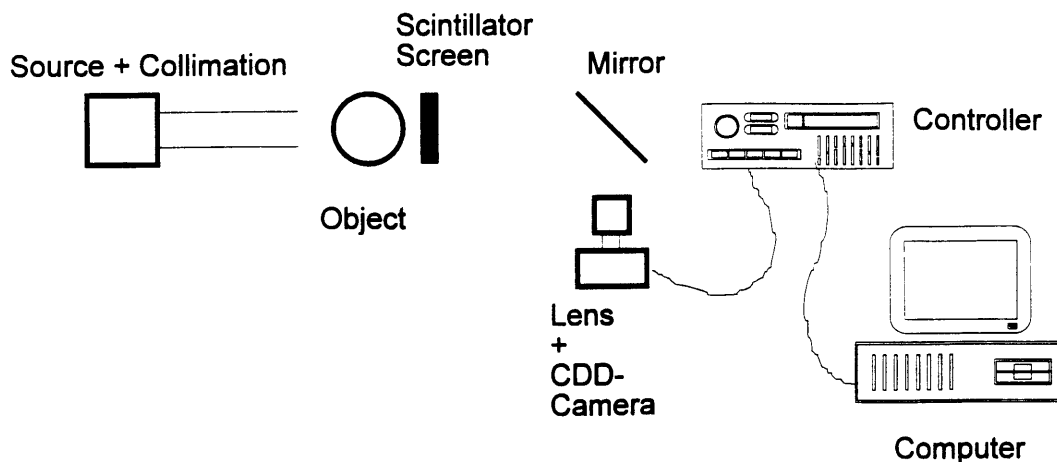
Figure 4. Schematic of neutron radiography system

The neutrons come from the source, pass through the collimating device and hit the object. The object can be moved about with the handling device to enable two-,or if necessary, three-dimensional scans. The remaining neutron flux behind the object hits the detection unit where each incident neutron is transformed into a certain number of photons. The photons are gathered by a lens onto the front surface of a Charge-Coupled-Device (CCD) chip. This produces an electrical signal proportional to the number of incident photons (and to the number of neutrons). The analog electrical signal is converted by an A/D-board and made available in a digitized form as an image on the computer monitor in various gray-shades (or color). The pictures can be manipulated, enhanced and analyzed on the computer using imaging software. If necessary, a tomographic reconstruction can be made.

3.3 Detailed Review of System Components

3.3.1 Neutron Source

There are specific demands on the neutron flux supplied by the source:

31

1.) A certain minimum "strength" (Intensity).

2.) Constant flux with small variations ($\delta\Phi / \delta t$ small, although this becomes less important with longer integration (exposure) times).

3.) Constant level over a sufficiently large time to acquire data.

The most obvious choice for this source is a nuclear research reactor. The negative points are that the whole test equipment and the object to be tested has to be transported to the reactor. Furthermore, the time schedule for the experiments has to be coordinated by reactor operations with other scientific groups using the reactor. The neutron flux in the beam port may be "contaminated" by γ-radiation, which imposes certain additional demands on shielding of the camera.

Non-reactor sources can be Cyclotrons with the appropriate targets, e.g. a Be (p,n)-reaction. The same problems as for the reactor above can apply (immovable, coordination of experiments). On the other hand, there are some quite compact Linear Accelerators, which can be used combined with a Be (p,n)-target. The problem with these system often is the available neutron flux. The smaller and more compact a unit gets, the less powerful it tends to be. Similar to a reactor source, the neutron beam can be contaminated with γ-radiation, necessitating additional shielding or leading to optical disturbances in the detection system.

A further possibility is the use of a pulsed source. The neutronic power densities of these normally are quite high. To be able to utilize this kind of source, a timing device between the source and the detection/optical system has to synchronize the pulses with the camera shutter.

The principle demands on a source for this system for non-destructive testing are:

- Transportable. The source has to be moved to the site of the component testing, if possible by one or two people.

- Powerful. For steel components with an average wall thickness a certain minimum flux is needed. The numbers will be determined in a later chapter.

- Non-nuclear. This is mainly a " political " issue. In the precise sense of the word, any device that produces neutrons at any time is based on nuclear reactions and therefore "nuclear". The meaning of the term "non-nuclear" is that it can not be a reactor or radioactive elements which need special handling, shielding and institutional control at all times.

- Reasonable power demands. For on site testing, the power demands have to be met by normal, industrial standard power supply circuits. If absolutely necessary, a separate, small generating group could be imagined.

- Easy to handle. The source has to be moved around on the site, in some cases even around the circumference of a pipe.

This list is not complete, but it already shows a few of the many, sometimes seemingly contradictory demands set upon the neutron source. It will by no means be simple to meet all of these demands, some compromises are inevitable. A weighting of the demands and comparison to the possibilities will have to take place for any possible source. Work on looking for and evaluating sources is ongoing. For the experiments described in this paper, a reactor or stationary linear accelerator [5] can be used, as the main purpose is to evaluate the basic possibilities of the system under laboratory conditions.

3.3.2 Object Handling

Object handling is a concern for a system that is set up in a laboratory environment. A transportable system that is used in power or chemical plants and on other large objects will have to be moved around the (stationary) object.

Object handling, meaning the movement of the object during a neutron radiography experiment, has to be done remotely. Many systems are available with two- and three-

---

5 Strictly speaking, an accelerator is a RF quadrupole. The term " Linear Accelerator " has found widespread use, even though it might not be correct in an absolute sense.

dimensional, remotely controlled tables. The tooling industry uses such devices, five or six independent axis can be controlled from one input device. Often, these are interfaced to a computer so that defined, pre-recorded programs of movements can be run. Simple handling devices for these experiments are available for use with small computes, e.g. the " nuDrive 3-axis system " which interfaces on to a Macintosh Computer and can run a preprogrammed sequence of movements.

3.3.3 Neutron Detection Device

For the detection of the neutrons after they have passed through the object, a Scintillator Screen is utilized. It absorbs the neutrons and emits a certain constant average number of photons for each incident neutron. The scintillator screen that is going to be used for these experiments is a ^{6}LiF-ZnS type, supplied by Nuclear Enterprises , Part -# NE 426. The wave length of the emitted light is in the blue-green range. Although this is not the optimum wavelength for detection by a CCD, a quantum efficiency ε_q of about 0.3 can be expected [6]. The reason for choosing this detector was commercial availability, although import into the USA took approximately two months as ^{6}Li is a controlled substance. The detection efficiency ε_d for this screen is 0.15 for thermal neutrons that incident at an angle of 90° to the screen. An advantage of this screen is a very small detection efficiency for γ-radiation, as some of the sources mentioned in 3.3.1 have noticeable amounts of " γ-contamination " along the neutron beam.

3.3.4 Optical Lens

The optical lens is mounted to the front of the CCD-camera. The function of the lens is to gather the light emitted from the scintillator screen onto the front surface of the CCD-chip. The characteristics of the lens strongly influence the detection capabilities of the

---

^{6}ZnS uses either an Ag actuator or a Cu activator. The Cu activator produces a light which is closer to the green-range and hence is somewhat better in conjunction with Charge-Coupled-Devices.

system. A large amount of light is lost due to the minification of the larger scintillator screen (object size) on to the CCD-chip (image size).

The characteristic values for a lens are:

- Focal length (f [mm]). This is the distance from the lens to the point at which incoming parallel rays focus. Some camera lenses have continuously variable focal length within certain boundaries.

- F-number (Aperture; F [-]). This is the ratio of the focal length to the lens diameter. A lens with a large diameter has a better light-gathering power and a smaller f-number. The F-number can often be adjusted on camera lenses to account for different light conditions.

The lens equation can be used to calculate the image distance if the object distance and the focal length are known.

$$^1/_p + ^1/_q = ^1/_f \hspace{4cm} (3.13)$$

p: Distance object to lens, q: Image distance, f: Focal length of the lens

The minification, m, is defined as the ratio of the object height to the image height:

$$m = H_o / H_i \hspace{4cm} (3.14)$$

H_o: Object height [mm], H_i: Image Height [mm].

This can also be expressed by the ratio of p to q.

Using these ratios and the lens equation, various information can be found based on given data. For example, if the focal length and the desired minification are given, the image distance and object distance can be calculated:

$$q = f(1+m)/_m \hspace{1.5cm} (3.15)\text{and} \hspace{1.5cm} p = mq \hspace{1.5cm} (3.16)$$

Image defects: The ability of a lens to form a perfect optical image is limited by certain defects. These are called aberrations. A simple, non-color corrected lens will have color aberrations, caused by different wavelengths of light being refracted at slightly different angles. There are other defects, like astigmatism, coma and spherical aberration that cause an image to be blurred. A sign of the quality of a lens is how small the effects of these defects are, closely controlled manufacturing, adjustment and the appropriate choice of lens material can keep these defects at a minimum.

Apart from the effects mentioned above, there are certain optical effects that limit the amount of light that can be captured by a lens system. This is given by the factor L, which expresses the fraction of light captured from a screen (Lambertian radiator) into a lens and is valid for small angles in the following form:

$$L = 1 / \{2F(m + 1)\}^2 \qquad\qquad (3.17)$$

Example: Object height H_o = 100 mm. CCD height 1150 x 22.5 μm = 25.9 mm. F-number of the lens F = 0.95.

$$m = H_o / H_i = 100 / 25.9 = 3.86$$

$$L = 1 / \{2F(m + 1)\}^2 = 1 / \{2 \times 0.95(3.86 + 1)\}^2 = 1.17 \times 10^{-2}$$

This shows, that only about 1.2 % of the light from the scintillator screen gets captured by the lens. Changes in m and/or the F-number of the lens towards higher values make this number smaller proportionally to the inverse square. Just using a lens with an F-number of 1.3 reduces L to 0.63 %, about half of the above value. The reasoning to use a larger CCD-chip also becomes obvious, as m is inside the squared brackets in the denominator too.

Furthermore, the lens is not perfectly transparent to the light passing through it. A certain amount of light gets lost due to reflection and refraction processes. A typical value for the transmission efficiency ε_l of lenses is 0.85.

Various lenses supplied by many name brand manufacturers where surveyed for this system. Four major manufacturers with interesting products for our purposes where:

- Jos. Schneider Optische Werke Kreuznach Gmbh & Co. KG in Germany
- Rodenstock Precision Optics, Inc. in Rockford, Ill. (US Distributor)
- Canon USA, Inc. in Englewood Cliffs, NJ
- Fujinon USA, Inc.

In an effort to limit the size of the test equipment, a so called "Wide Angle Lens" was searched for. These are characterized by focal lengths smaller than 50 mm. With such a lens it is possible to image a given object size onto a predetermined CCD at a smaller object distance. The disadvantage of these lenses are higher distortions, especially in the edge areas with smaller focal length.

The following lenses were compared:

Table 1. Comparison of Lenses

Lens Name	Focal Length	Max. Aperture	Price (1993)
Schneider XENON	17 mm	0.95	$ 865.-
Schneider XENON	25 mm	0.95	$ 738.-
Schneider XENON	42 mm	0.95	$ 1100.- (approx.)
Canon PH6x8 Zoom	8 ~ 48 mm	1.0 (at ? focal length)	$ 800.- (approx.)
Rodenst. TV-Heligon	42 mm	0.75	
Rodenst. TV-Heligon	50 mm	0.75	
Fujinon CF25L	25 mm	0.85	$ 350.-

After comparing the technical data sheets, calculating some possible layouts and taking into account the cost/features ratio, the Fujinon CF25L was acquired with a C-Mount. This should be sufficient for the first set of experiments and constitutes a great improvement over the TAMRON 28 ~ 70 mm zoom lens with f-number 3.5 used in Ref. [3] (see footnote p. 9).

3.3.5 CCD-Camera Systems

The CCD-Camera System is made up out of several components:

1. The CCD-Chip in the Camera Head.

2. The Camera Head with the Shutter, Cooling and Power Supply for the CCD-Chip, Preamplifier Circuitry, Lens and Camera Casing (with Mounting Frame).

3. The Camera Controller. This controls the Shutter, camera cooling, data acquisition, and transfer to the computer. It contains the A/D Converter(s) and the Power Supply for the Camera Head.

4. The Computer Interface Card. This acquires the data from the Controller A/D Converter and makes it accessible to the computer data bus.

5. The Computer System. The data from the interface card can be stored on a hard disk, displayed on the monitor, enhanced and analyzed. Hardcopies of images can be made on a connected printer or data transferred over a network.

Components 1.) and 5.) can be specified by the user in quite a large range of different makes and types for one given system manufacturer. The other parts are mostly predetermined by the manufacturer, although some choices for the A/D Converters do exist.

The choice of the CCD-chip and A/D converter directly influences the quality of the image. Some important characteristic values for the CCD-chips are:

- Number of horizontal and vertical pixels.
- Size of an individual pixel.

- Readout Noise.

- Dark Charge (Dark Current, Dark Noise).

- Dynamic Range (measured in bits of parallel data processing).

- Grade, specified by the number of defective pixels in the array.

The number of horizontal and vertical pixels and the pixel size directly influence the size of the CCD-chip. This then goes into eqn. (3.14) and influences the light-capture fraction L in eqn. (3.17). A larger chip will thus be beneficial to the factor L, giving a better overall efficiency of the scintillator-camera system. The number of pixels also influences the spatial resolution. A small number of pixels in either dimension will give a bad, very coarse resolution of the object. This is especially important for the detection of hydrogen in steel, as changes in the concentration can take place over small distances. Readout Noise influences the optical resolution of the CCD-chip, the capability to resolve small differences in light intensity. If the readout noise is high, subtle variances in the light intensity will get "drowned" by the noise. This is a very important area for the proposed system, as the basic principle relies on the detection of small variances in neutron flux, which give proportionally different brightness at the scintillator screen. A more detailed discussion of this subject will take place in chapter 3.5.

Dark Charge, often also called Dark Noise (or -Current), is relevant for the minimum flux that can be detected. This relates to the source flux, the object geometry and the object properties. The dark current is the amount of current the CCD-chip passes on to the preamplifier and the controller even when there is absolutely no light incident on the CCD. A high dark current will "cover up" a very low intensity light source, disabling the detection. Dark current on CCD-chips is proportional to the temperature and usually reduces by half with every decrease in temperature by 5 - 6°C. This is the reason why CCD-cameras for scientific low-light experiments are mostly cooled. The influence of this value on the neutron radiography system will be described in chapter 3.5.

39

Dynamic Range is measured in bits on a CCD-camera system. This expresses how many bits are available at the A/D Converter to describe the status of an analog value, in this case the light intensity (measured as a charge) at a pixel. A small number of bits enables less values to be assigned to a given state, e.g. 1 bit gives $2^1 = 2$ values ("on" or "off"). With 8 bits, $2^8 = 256$ shades of grey can be described. A large dynamic range is desirable, similar to the considerations for readout noise. Here, the influence is on the ability to display small variances in the light intensity.

The quality of CCD-chips are specified by grades, grade 1 being the highest quality. This classification is done by testing the device after the manufacturing process. Every grade has a specific limit on the number of faulty points, clusters and columns. The grade has a direct influence on the price of the chip. As the object can be moved in relation to the surface of the CCD in these experiments, a lower grade chip can be chosen without negative effects.

The choice of Computer System influences the depth of possible data analysis and the speed at which this can be done. As a full readout of one image can easily represent several megabytes of information, the demand for a fast computer with large storage capacity and plenty of memory becomes obvious. Furthermore, the display subsystem (monitor and display adapter) should be able to show the full information received from the camera. For a CCD-Chip with 1000 x 1000 pixels, the monitor would have to be able to display at least the same number of picture points. The same applies to the dynamic range, where the small variances in light intensity have to be equally well represented on the monitor for analysis.

3.3.6 Enclosure and Mounting for Scintillator and Camera

In an ideal case, the CCD-camera should only "see" the light emitted by the scintillator screen. All backlight and diffuse light from the surrounding room has therefore to be avoided. This is done by enclosing the scintillator screen, the lens and the CCD-chip in a

light-tight box. Furthermore, to keep the γ-radiation of the neutron beam away from the sensitive camera, a mirror is used to place the camera at an angle (e.g. 90°) to the axis of the beam.

The box has to be made out of a material that is not neutron activated, so that it can be moved or settings changed without necessitating additional shielding or radiation protection. For this reason, aluminum was chosen. The box is constructed of a welded aluminum frame for stability with aluminum plates fixed to it by plastic screws. The plates are removable for initial setup and adjustment of the mirror. The size of the box is approximately 90 cm x 30 cm x 30 cm. Details of the construction are included in appendix D

3.4 Basic Modeling Of System

For the computer simulation of the system in chapter 5, it is necessary to model the individual components as a set of equations. These equations can the be connected together to give the response of the system to a given set of input parameters. The influence of variations on the results can be studied.

Most of the components can be modeled very simply by giving efficiencies for the processes involved.

Source: The source is represented by a unidirectional neutron flux incident on the object. In most cases this is not the flux of the actual source (e.g. reactor) itself, as losses are involved in the thermalization, guidance in the beam-tubes and collimation. The source flux is represented by the symbol N_0 (see also eqn. 3.1, p.12) and expressed in $n / cm^2 s$.

Object: The object is described by the attenuation of the neutron flux, described by equation 3.12:

$$N_i(x) = N_0 \, e^{-\rho \, [\, \mu_1 \, x_1 + \{ \mu_1 \, (1 - p / 10^6) + \mu_H \, (p / 10^6) \} \, x_2 \,]} \qquad\qquad (\, 3.12 \,)$$

This equation is valid for a plate geometry. For a pipe, the lengths x_1 and x_2 have to be redefined.
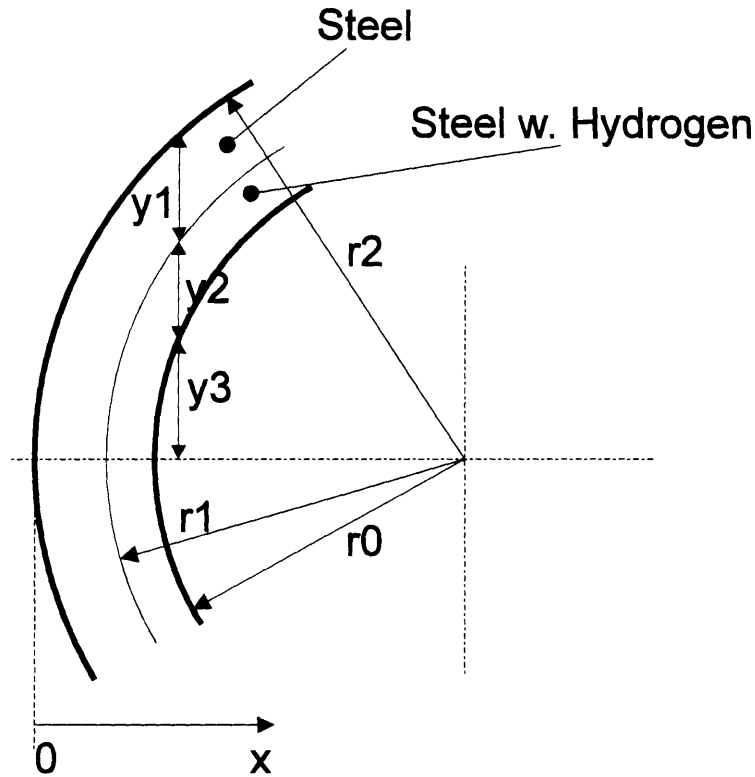
Figure 5. Pipe geometry for neutron beam attenuation.

For this modeling, hydrogen embrittlement of the inside of the pipe is represented by a low uniform re-distribution of hydrogen over a certain depth of the inside of the pipe. Given: Inside radius r0, radius of uniform hydrogen loading r1 and outside radius r2. The values y1, y2 and y3 have to be determined.

$$y \text{ tot} = y1 + y2 + y3 \tag{3.18}$$

Applying trigonometry, the results for y1, y2 and y3 can be found:

$$y3 = \sqrt{\{ r0^2 - (r2 - x)^2 \}} \tag{3.19}$$

$$y2 = \sqrt{\{ r1^2 - (r2 - x)^2 \}} - y3 \tag{3.20}$$

$$y1 = \sqrt{\{2\,r2\,x - x^2\}} - y2 - y3$$
$$= \sqrt{\{2\,r2\,x - x^2\}} - \sqrt{\{r1^2 - (r2 - x)^2\}} \qquad (3.21)$$

These values for the lengths can then be inserted into equation 3.12. As the neutron beam will also have to traverse parts of the fluid inside the pipe, the length y3 had to be introduced.

$$N_i(x) = N_0 \exp\left[-\{\mu_{Fe}\,2\,y1\,\rho_{Fe} + \mu_{res}\,2\,y2\,\rho_{Fe} + \mu_{fl}\,2\,y3\,\rho_{fl}\}\right] \qquad (3.22)$$

μ_{Fe}: Att. coef. of Iron; μ_{fl}: Att. coef of fluid in pipe; ρ_{Fe}: density of Iron; ρ_{fl}: density of fluid.

Scintillator Screen: $N_i(x)$ is the number of neutrons that strike the front surface of the scintillate screen. The scintillator screen detects:

$$N_d = N_i(x)\,\varepsilon_d \qquad (3.23)$$

N_d: Neutrons detected by scintillator $[\,n\,/\,cm^2s\,]$; ε_d: detector efficiency.

The transformation of incident neutrons into photons takes place with a constant transformation factor, given for the type of screen and neutron energy:

N_γ : Transformation Factor $[\,e\,/\,n\,]$.

Lens: The lens can be described with the light-capture fraction L of equation 3.17:

$$L = 1\,/\,\{2F(m+1)\}^2 \qquad (3.17)$$

Furthermore, the lens has a certain efficiency, ε_l.

CCD-Camera: The first number of interest is how many photons are incident on the front surface of the CCD-Chip. This is proportional to the neutron flux incident on the front side of the scintillator screen.

$$P \propto N_i(x)$$

$$P = N_i(x)\, L\, \varepsilon_l\, m^2 = N_i(x)\, L\, \varepsilon_l\, \varepsilon_d\, N_\gamma\, m^2 \qquad\qquad (3.24)$$

P: Photon flux incident on front of CCD [$e / cm^2 s$]

The factor m^2 comes from the decrease in area due to minification.

The second number of interest is how many electrons (= current) are available at the output of the CCD-Chip. This is the signal that is then used to generate an image.

$$N_e = P\, \varepsilon_q = N_i(x)\, L\, \varepsilon_l\, \varepsilon_d\, \varepsilon_q\, N_\gamma\, m^2 \qquad\qquad (3.25)$$

N_e: Signal at output of CCD-Chip [$e / cm^2 s$]; ε_q: Quantum efficiency of CCD-chip.

For most uses, the strength of this signal for one pixel of the CCD-Chip is of interest. To calculate this number, N_e has to be multiplied by the ratios of the image area to the CCD area and the CCD area to the total number of pixels.

$$N_e\ [\ e / pixel\ s\ ] = N_i(x)\, L\, \varepsilon_l\, \varepsilon_d\, \varepsilon_q\, N_\gamma\, m^2\ (\ A_i / \#p\ ) \qquad\qquad (3.26)$$

A_i: Image area, measured on scintillator screen [cm^2]; $\#p$: Total number of pixels on CCD-Chip.

Camera Head, Controller, Computer: These parts of the system are not included in the modeling anymore, thus N_e in [$e / pixel\ s$] is the final result. The effects of amplification, conversion from an analog into a digital signal and modification into grey-shades for the display on the monitor are difficult to model. The relationship between the

output signal of the CCD-Chip and the grey-shade on the monitor will have to be found by calibration on the actual system.

3.5 Influence of Noise on System Performance

a.) First approach:

The noise of the CCD-camera system is made up of three components:

- Statistical noise of the signal ("Shot noise")

- Readout noise of the CCD-chip

- Dark noise of the CCD-chip.

The total noise of the system can be written as:

$$\sigma(t) = \sqrt{\{ (P + B) t \varepsilon_q + D t + N_r^2 \}} \qquad (3.27)$$

σ: Total noise of system [e / $_{pixel\ s}$]; P: Photo-electron flux incident on CCD [e / $_{pixels}$]; B: Background photo-electron flux on CCD ("Background light") [e/$_{pixel\ s}$]; D: Dark noise [e / $_{pixel\ s}$]; N_r: Readout noise [e^{RMS} / $_{pixel}$]; t: Integration time [s].

For further calculations, B will be assumed to be zero, there is no background light on the CCD, it is enclosed in a light tight box. In this case, the term (P + B) t ε_q can be replaced by N_e t (see equation 3.25). Equation 3.27 can then be simplified to:

$$\sigma(t) = \sqrt{\{ N_e t + D t + N_r^2 \}} \qquad (3.28)$$

In electronic systems, the absolute noise level is seldom given. The use of the " Signal to Noise Ratio " (SNR) is much more common, as a dimensionless comparison, independent of the signal strength can be made. In the CCD-camera system, the signal is

45

given by N_e. The SNR is dependent of the integration time t required to acquire the image.

The time dependent SNR can then be written as:

$$SNR(t) = N_e(t) / \sigma(t) \qquad (3.29)$$

Inserting 3.28 into 3.29:

$$SNR(t) = N_e\, t / \sqrt{\{\, N_e\, t + D\, t + N_r^2 \,\}} \qquad (3.30)$$

Two regions of the time dependent SNR can be distinguished:

- For very short exposure times, the read noise N_r becomes the dominant source, the other terms can be omitted with a good approximation. In this case, equation 3.30 reduces to:

$$SNR(t) = (N_e / N_r)\, t \qquad (3.31)$$

This is known as the " Read noise dominated area ".

- For longer exposure times, the read noise is negligible. Equation 3.30 reduces to:

$$SNR(t) = (N_e / \sqrt{\{\, N_e + D \,\}})\, \sqrt{t} \qquad (3.32)$$

This is then called the " Shot noise dominated area ".

The dependance of the various components on exposure time can be summed up:

Dark noise $\sim \sqrt{t}$

Statistical noise $\sim \sqrt{t}$

Read noise = constant

Signal $\sim t$

The SNR can be displayed for a certain system in a graph as a function of t.

46
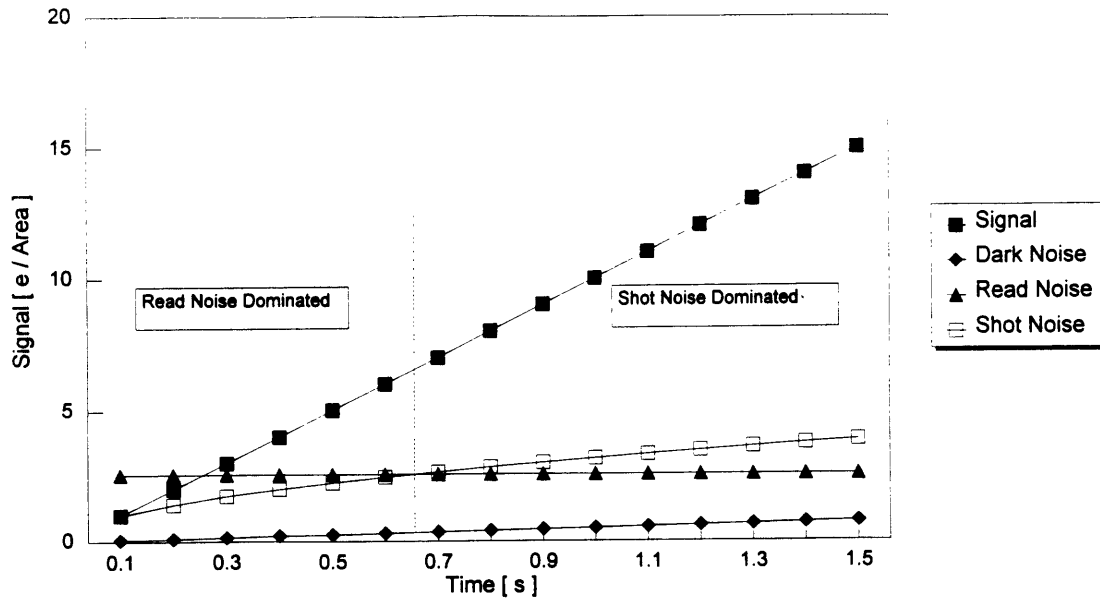
Figure 6. Example of a SNR-Diagram.

b.) Second approach:

The noise of a system can also be approached by first looking at the purely statistical

noise and including the system specific parameters later.

Generally, the statistical noise of a signal is equal to the square root of the signal. For the

" signal flux " N_d of the scintillator screen, the statistical noise is $\sqrt{N_d}$. The statistical

noise of the electrons produced at the CCD is also the square root of this signal. We want

to relate this noise to the detected neutron flux at the scintillator screen. For this, we have

to introduce the number N_c, the number of photons produced per detected neutron.

$$N_c = L\ N_\gamma\ \varepsilon_l\ \varepsilon_q \qquad\qquad (3.33)$$

The component of the noise added by the CCD-chip, expressed as detected neutrons, is

proportional to $1 / N_c$. To calculate the absolute value, we have to multiply with N_d. The

components then are added up in quadrature:

47

$$\sigma_n{}^2 = N_d + N_d \left(1 / N_c \right)$$

Noise: $\qquad \sigma_n = \sqrt{\{ N_d + (N_d / N_c) \}}$ $\qquad\qquad\qquad$ (3.34)

σ_n: Noise expressed in terms of the number of neutrons [n / cm^2 s]

By multiplying equation 3.34 with N_c, we get the statistical noise in terms of electrons. The system specific noises, i.e. readout noise and dark noise, are added to this statistical noise in quadrature:

$$\sigma_e{}^2 = N_c{}^2 \left[N_d + (N_d / N_c) \right] + D^2 + N_r{}^2$$

Noise: $\qquad \sigma_e = \sqrt{\{ N_c{}^2 N_d \left[1 + (1 / N_c) \right] + D^2 + N_r{}^2 \}}$ $\qquad\qquad$ (3.35)

σ_e: Noise expressed in terms of the number of electrons at the CCD [e / cm^2 s].

By applying the area reduction factor (A_i / $_{\#p+}$), this can then be transformed into [e/$_{pixel}$ $_s$] There is no time dependence on this way of expressing the noise, as integration time is not taken into account in equation (3.35). This can be done by multiplying the appropriate terms in the equation by the integration time. (Signal and dark noise)

The noise influences system performance in two ways:

1. In the read noise dominated region, it sets the minimum source flux needed to give a signal that is above the read noise with all other system parameters given.

2. In the shot noise dominated region, the minimum resolution for variances in the signal is determined. The variance in the signal that can be detected (Difference in steel without hydrogen to steel with hydrogen => Hydrogen loading) has to be larger than the shot noise.

CHAPTER 4

MODELING AND COMPUTER SIMULATION

4.1 Basic Model

The basic model used for the simulation of the neutron radiography system is made up of the components as described in chapter 3.4. The fundamental equations to describe the system are 3.22 and 3.26. These can be used to evaluate the response of the system to various parameter changes. Calculations of the Signal-to-Noise ratio will also be based on these equations, as they supply the input data for the signal.

A method had to be found to be able to change parameters quickly and make results visible numerically as well as graphically. Calculation by hand (with a calculator) is possible, but would be time consuming and error-prone. As the same type of calculations have to be repeated several times, the spreadsheet program " Lotus 1-2-3, Release 4 " (for Windows)was chosen. Some calculations were also done with " MathCAD 3.1 " (for Windows), as this has the ability to solve equations for an implicit variable. Most of the results will be presented in diagrams of signal at the CCD-chip output vs. distance x, measured from the outer diameter of the steel pipe.

Basic assumptions for the spreadsheet model: This model of the system has been kept as simple as possible so that the reaction to changes can be made visible. The assumptions are:

- The " Source Flux " is the flux incident on the object.
- There are no scattered neutrons incident on the detector screen.
- The material properties density and mass attenuation coefficient are uniform over the whole object.
- Hydrogen distribution is uniform in the object to a certain depth.

49

- The scintillator screen has a uniform detection and conversion efficiency over the whole area.

- Optical distortions in at the edge of the image area are not taken into account.

- The mirror has an optical efficiency of 1.

- The CCD-chip has no defects.

- The mass attenuation coefficient for the object is the coefficient for iron. The effects of alloying elements cancel out on an average.

The effects of some of these simplifications will be discussed in chapter 6.

4.2 Parameter Variations and Case Studies

In the following chapter 4.2, the basic input values for the spreadsheet are varied around a basic case defined in chapter 4.2.1. Two variations are chosen, the first at a lower, the second at a higher setting. These changes serve two purposes:

a. The model and the resulting spreadsheet can be checked for correctness. The influence of the variations on the input parameters on the results has to agree with the physical and optical characteristics of the system.

b. The resulting figures are a simple tool to compare the magnitude of the change in the resulting signal. This can be used to compare the efficiency (measured by the increase of the signal level) of a modification in the components of the whole system.

4.2.1 Base Case

For a first look at the model, a base case is defined. Variations of the settings can then be compared to this to find the influences.

Source flux: $N_0 = 5 \times 10^6$ [n / cm^2 s], thermal neutrons.

Object geometry: Steel pipe, outside diameter 20 cm ($r_2 = 10$ cm), inside diameter 18cm ($r_0 = 9$ cm), $\rho_{Fe} = 7.88$ g / cm^3, image area 10 x 10 cm^2, contains water, $\rho_w = 1$ g / cm^3.

| Hydrogen Loading: | Uniform loading of inside diameter to a depth of 0.05 cm (r1 = 9.05cm) with 200 ppm. |

Hydrogen Loading: Uniform loading of inside diameter to a depth of 0.05 cm (r1 = 9.05cm) with 200 ppm.

Scintillator screen: Detection efficiency ε_d = 0.15, conversion factor N_γ=1.7x10^5 $^e/_n$

Lens: Focal length f = 25 mm, aperture F = 1, lens efficiency ε_l = 0.85.

CCD-chip: 1024 x 1024 pixels, pixel size 15mm, quantum efficiency ε_q=0.3, CCD-area 1.536 x 1.536 cm^2.

Attenuation Coefficients: μ_{Fe} = 0.15 cm^2/$_g$, μ_H = 22.0 cm^2/$_g$,, μ_w = 15 cm^2/$_g$.

Using the equations in chapter 3.4, the values for m, L and μ_{res} can be calculated:

$$m = 6.51 \qquad L = 0.00443 \qquad \mu_{res} = 0.15437 \text{ cm}^2/_g$$

All this data is used as input for the spreadsheet. The unit of distance x is always in cm.
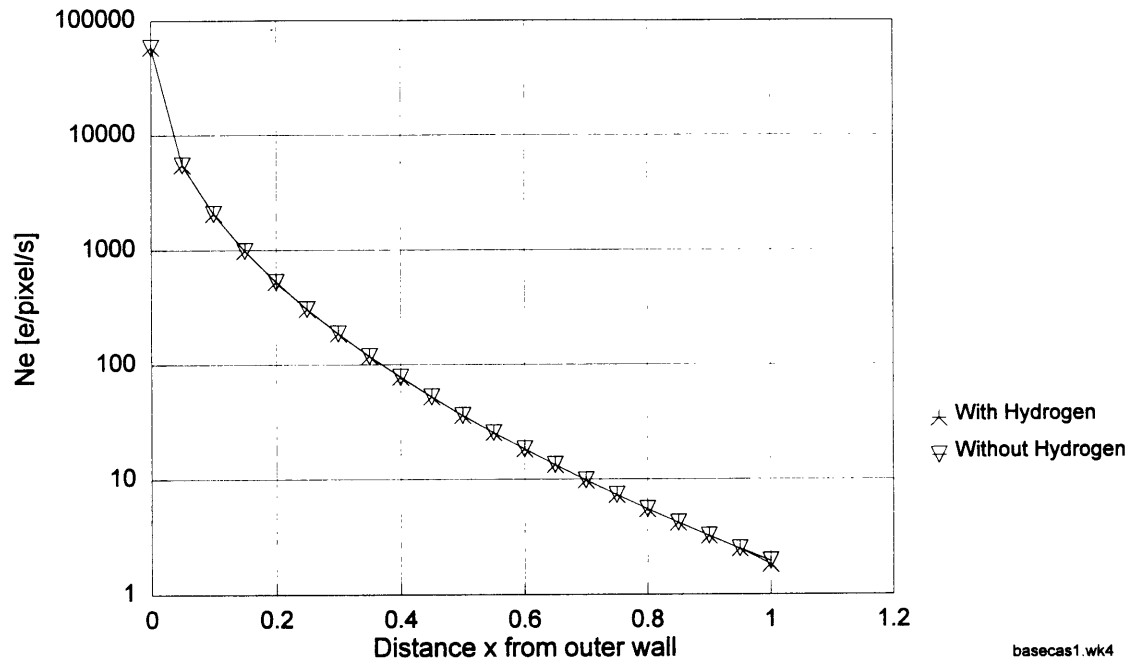
Figure 7. Base case. Signal at CCD-output vs. distance from pipe outside diameter.

51
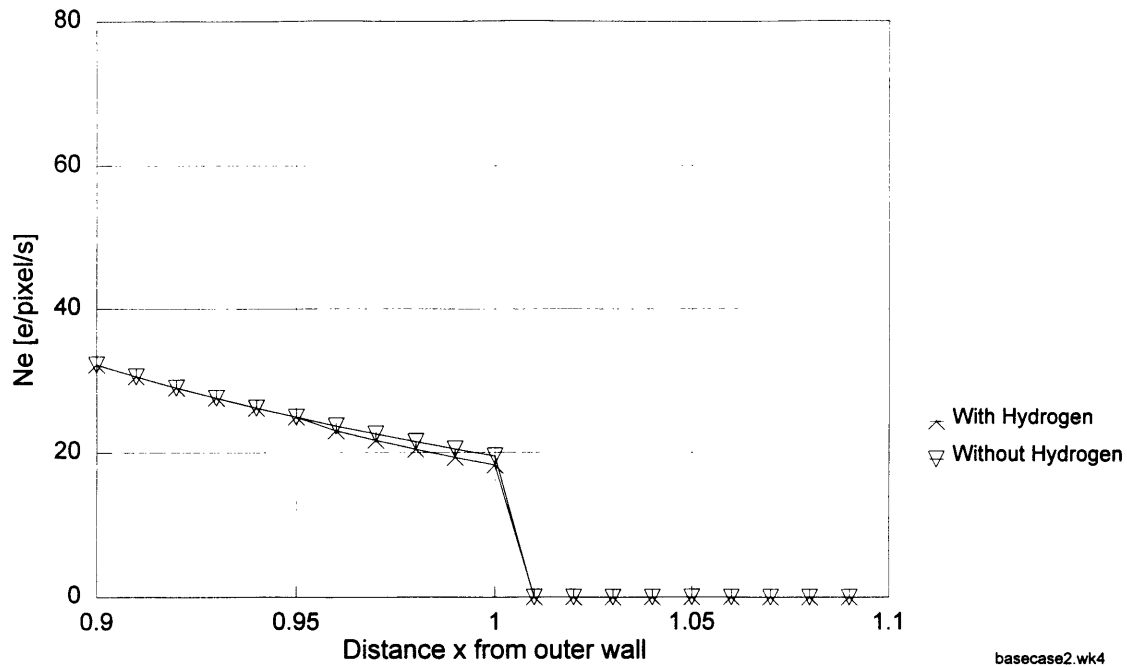
Figure 8. Base case. Signal at CCD-output. Enlargement of region around pipe inside diameter.

The strong attenuation of the neutron flux (expressed as the signal at the CCD-output)

by the steel of the pipe wall can be clearly seen. The signal decreases as a negative

exponential with x. The effect of the hydrogen in the inside wall is better visible in figure

8 by further attenuating the flux when compared to the curve without hydrogen. The large

drop at x = 1 cm is a result of the very strong attenuation by the liquid (Water) in the

pipe. The signal strength at x > 1 cm is approximately zero for any practical use. This can

serve as a very good method to detect the exact position of the inside wall of the pipe. In

the next illustrations, the region adjacent to the inside diameter of the pipe will be

displayed, as it gives the numbers of greatest interest for the evaluation of the system

performance.

The difference in the signal with and without hydrogen (ΔN_e) is not visible in the scale

chosen for figure 7. Compared to the absolute signal in the outer regions of the pipe wall

it is very small. The largest differential signal ΔN_e is achieved at the position of the

inside wall, as the highest value for the length y2 (attenuation length of steel with

hydrogen) is reached here. With decreasing x, ΔN_e gets continuously smaller, until the position corresponding to r1 (maximum radius of the uniform hydrogen loading) is reached, where it is zero. The detection of this difference is the fundamental task of this proposed system for NDT. It is a characteristic of the imaging system, how small a signal ΔN_e can be detected and sets a criteria for the suitability to the task of detecting hydrogen. The limitations for the detection of ΔN_e will be discussed in chapter 6.1.2. At this point it can be said that a good CCD-camera system with a correct setup is capable of detecting very small differences in the final signal, which correspond to the order of magnitude of ΔN_e in these examples. In general though, a higher value for the absolute signal and a larger differential signal are sought for.

4.2.2 Variation of Source Flux

The source flux is varied for a value lower and a value higher than the base case.
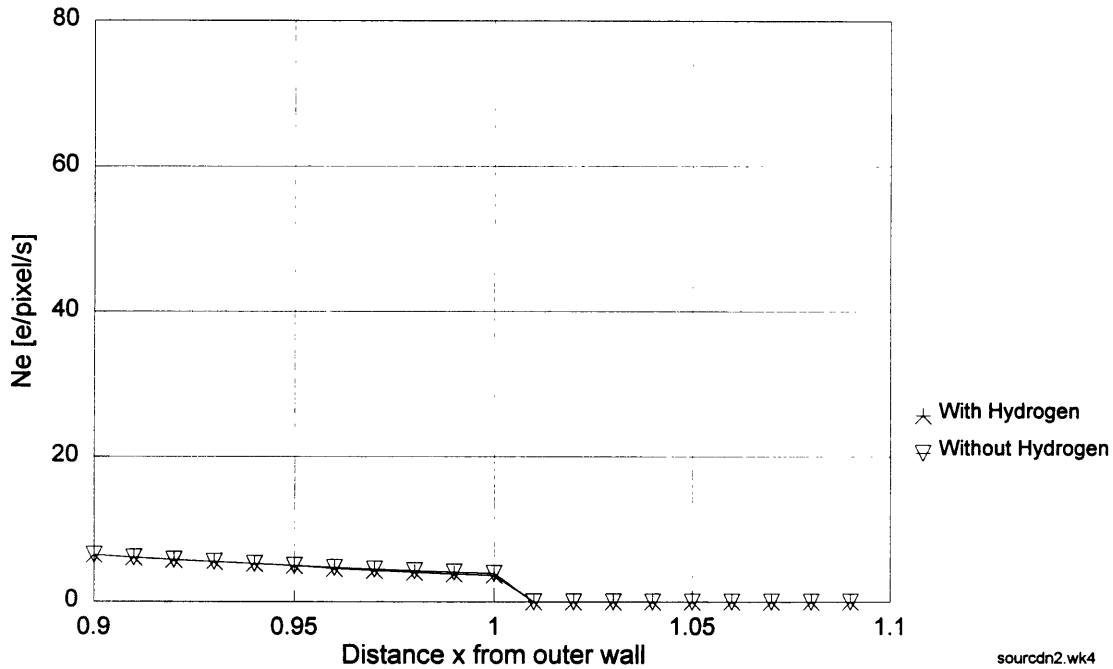
Figure 9. Source flux reduced to $N_0 = 1 \times 10^6 \, n/cm^2 \, s$
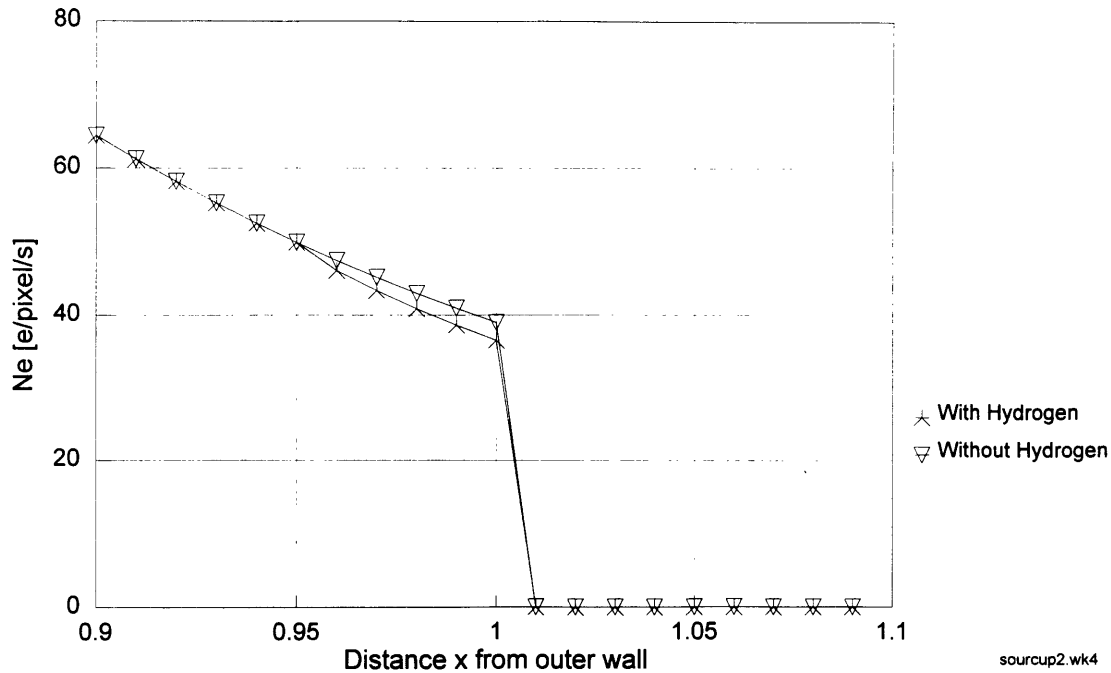
Figure 10. Source flux increased to $N_0 = 1 \times 10^7 \, n / cm^2 s$

It can be seen here that it is of importance to get the maximum possible flux incident on the object. A higher flux not only increases the absolute level of the signal, but also increases the differential signal ΔN_e considerably.

4.2.3 Variation of Object Size

The object is represented by the image area on the scintillator screen. A smaller object can be placed closer to the lens and CCD-camera, a larger object would have to be placed farther away. Using an adjustable zoom-lens would enable objects of varying sizes to be kept at the same distance.
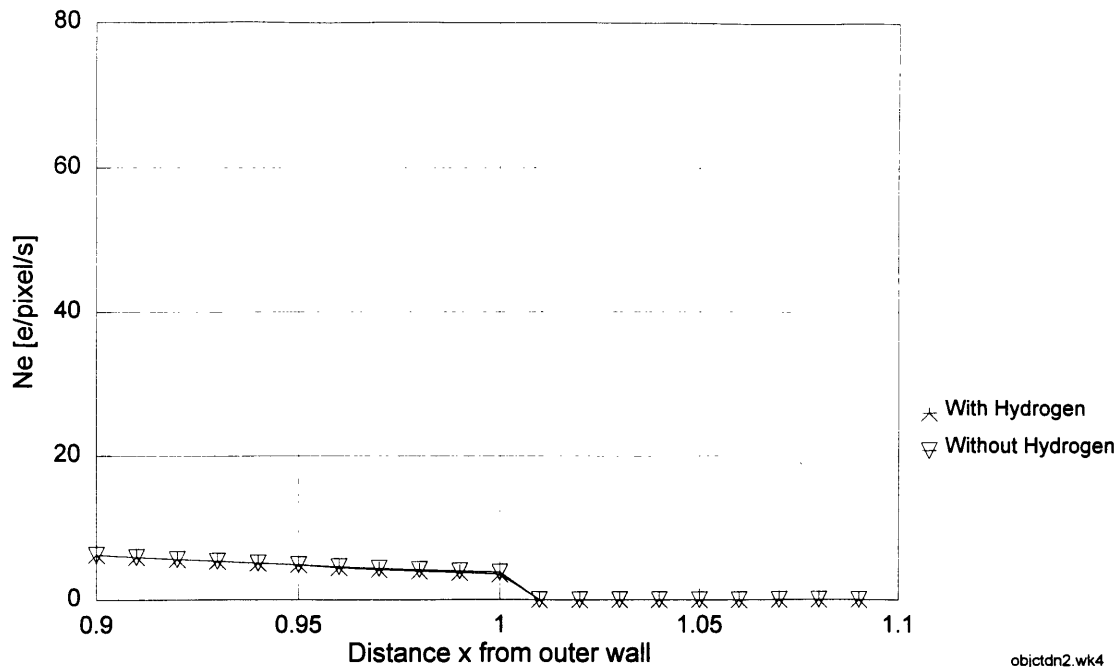
Figure 11. Object area reduced to 5 cm x 5 cm.
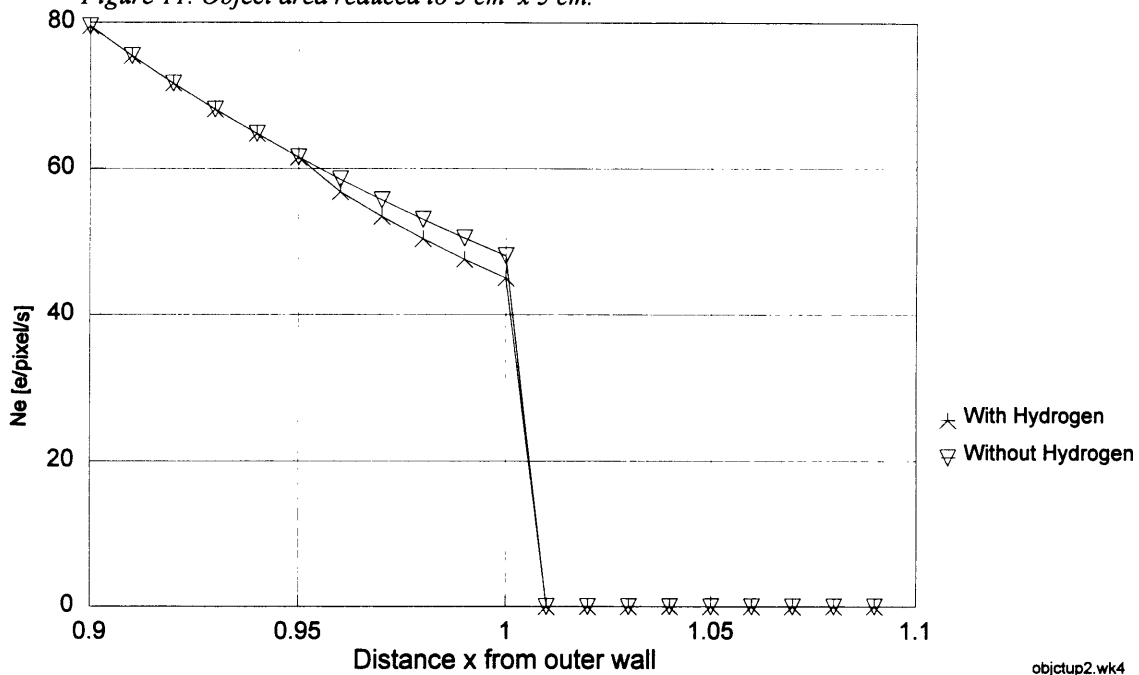
Figure 12. Object size increased to 15 cm x 15 cm.

The effect of a change in the object size on the final signal is two-fold:

1. Minification is changed. The numerical value is higher for larger object sizes.

2. The ratio of the object area to the number of pixels on the CCD is changed. This increases for larger object size.

The first effect is less noticeable, especially for large m. The reason for this can be seen if equation 3.17 for L is inserted in equation 3.26 .

$$N_e = [(\varepsilon_q \, \varepsilon_l \, \varepsilon_d \, N_i \, N_\gamma \, m^2) / (4 \, f^2 \, \{m + 1\}^2)] \, (A_i / \#p) \qquad (4.1)$$

For large numbers of m, the addition of 1 in the denominator can be neglected and m^2 cancels out. This then leaves the approximation:

$$N_e \sim (1 / 4f^2) \, (\varepsilon_q \, \varepsilon_l \, \varepsilon_d \, N_i \, N_\gamma) \, (A_i / \#p) \qquad (4.2)$$

The ratio of the object area to the number of pixels on the CCD-chip is the only remaining influence.

This agrees with what is to be expected from a physical sense as a bigger object produces a larger lighted area on the scintillator screen. The absolute number of photons (integrated over the whole lighted area) is therefore higher.

4.2.4 Variation of Hydrogen Content in Object

The assumed uniform distribution of hydrogen in the object is changed to a lower value of 100 ppm and a higher loading of 400 ppm. In a later phase, the effect of a non-uniform distribution of hydrogen will be discussed. The non-uniform distribution can be thought of as one of two cases:

- Distribution according to a non-linear function, e.g. parabolic, exponential, etc.
- Pseudo-arbitrary, according to the micro structure of the metal. Hydrogen concentrations can be found at grain boundaries and defects within the crystallographic structure.
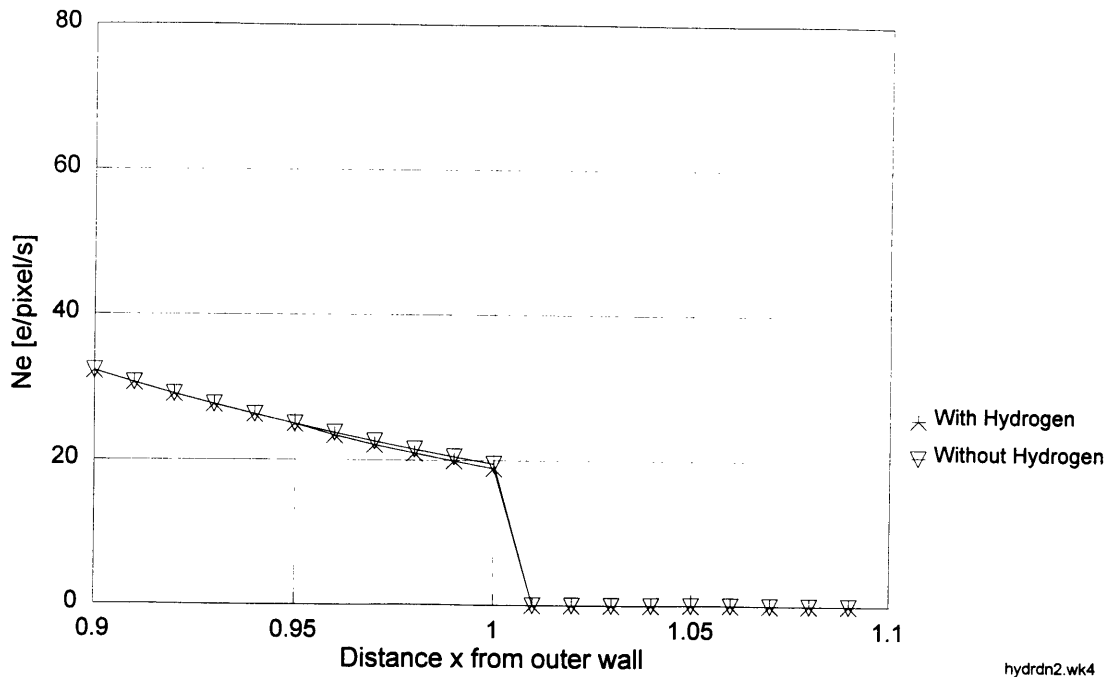
Figure 13. Uniform hydrogen distribution decreased to 100 ppm.
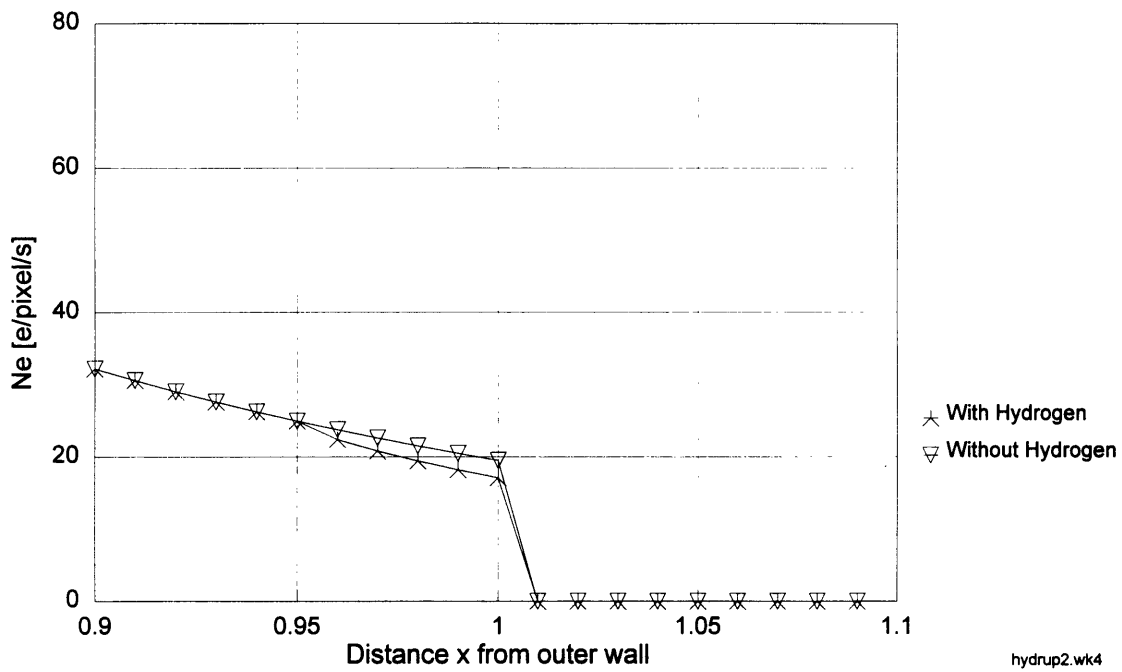
Figure 14. Uniform hydrogen distribution increased to 400 ppm.

These changes only affect N_e between r0 and r1 by decreasing or increasing the difference between the line without and the line with hydrogen. The factor p (Hydrogen loading) is in the exponent of equation 3.26 and varies μ_{res}. The effect on μ_{res} is small, the numerical values are given below:

Hydrogen loading:	100 ppm	200 ppm (base case)	400 ppm
μ_{res}:	0.15219	0.15437	0.15874

This agrees with the physics involved, as for a case without hydrogen there obviously would be no difference between the two lines. Hydrogen content in the steel matrix basically describes the ratio of the total nuclear interactions with neutrons between the hydrogen and the metal atoms. A higher hydrogen content, combined with a significantly larger cross-section, results in a stronger attenuation of the neutron beam than by the base metal.

4.2.5 Variation of Parameters of the Scintillator Screen

a.) **Variation of the detection efficiency** ε_d: Detection efficiency is a value given by the technical specifications of the screen. It depends on a variety of factors, e.g. the angle of incident neutrons, the construction of the screen, the materials used, etc. Except for the incident angle of the neutrons, none of the changes can be done by the end-user on a specific application. Detection efficiency increases when the screen is set at an angle smaller than 90° to the direction of the neutrons.
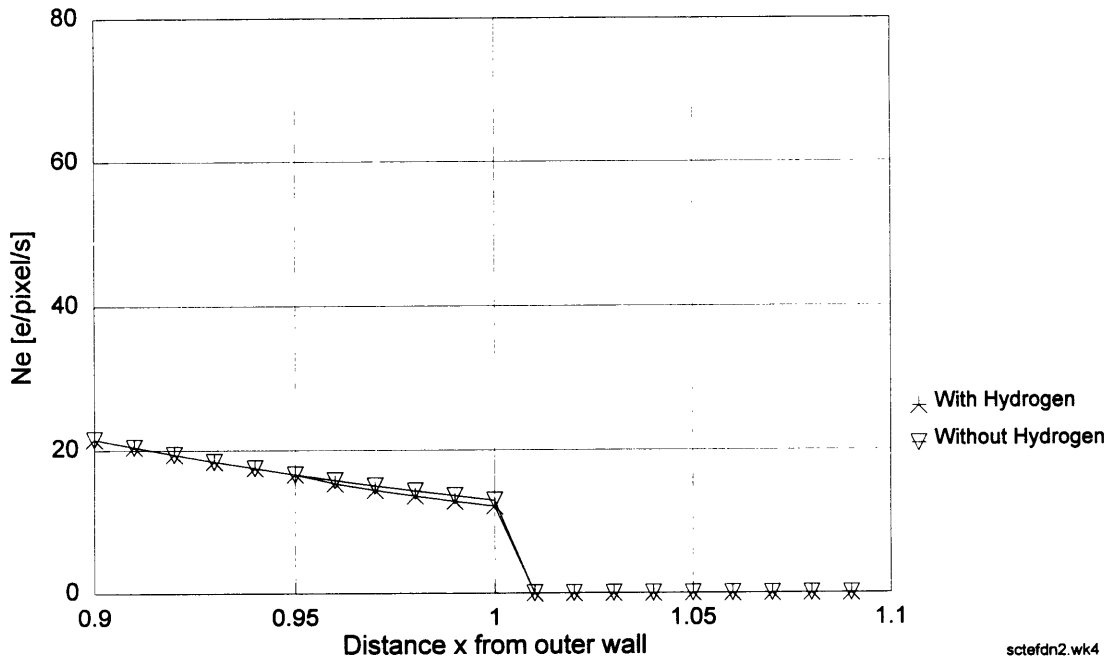
Figure 15. Decrease of scintillator screen detection efficiency ε_d to 0.1.

58
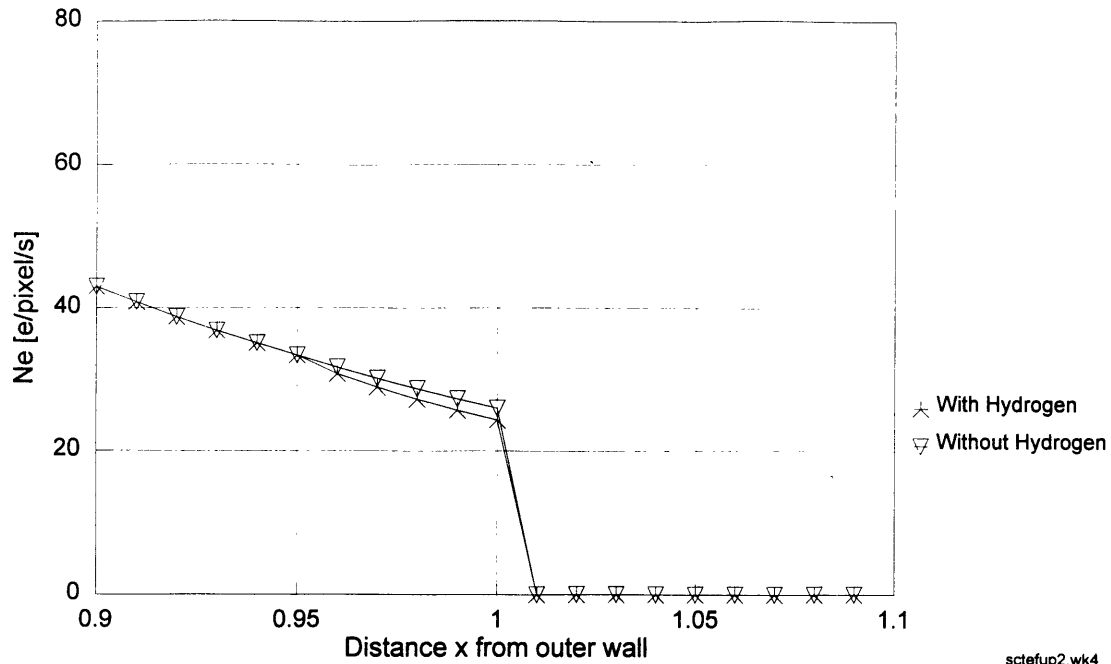
Figure 16. Increase of scintillator screen detection efficiency ε_d to 0.2.

Detection efficiency influences how many of the neutrons incident on the scintillator screen are available for transformation into photons. A higher efficiency combined with a constant transformation factor N_γ, will obviously result in a larger number of photons.

b.) Variation of the conversion factor N_γ: This also is a technical characteristic of the screen. One factor that influences this number is the neutron energy.
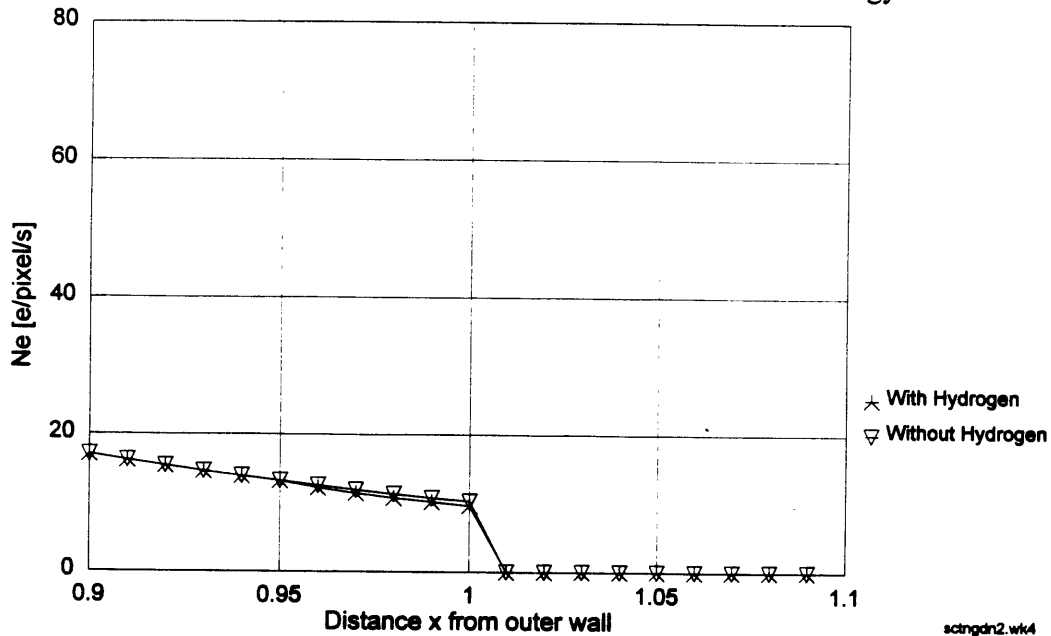
Figure 17. Low scintillator screen conversion factor $N_\gamma = 9 \times 10^4 \, e/_n.$
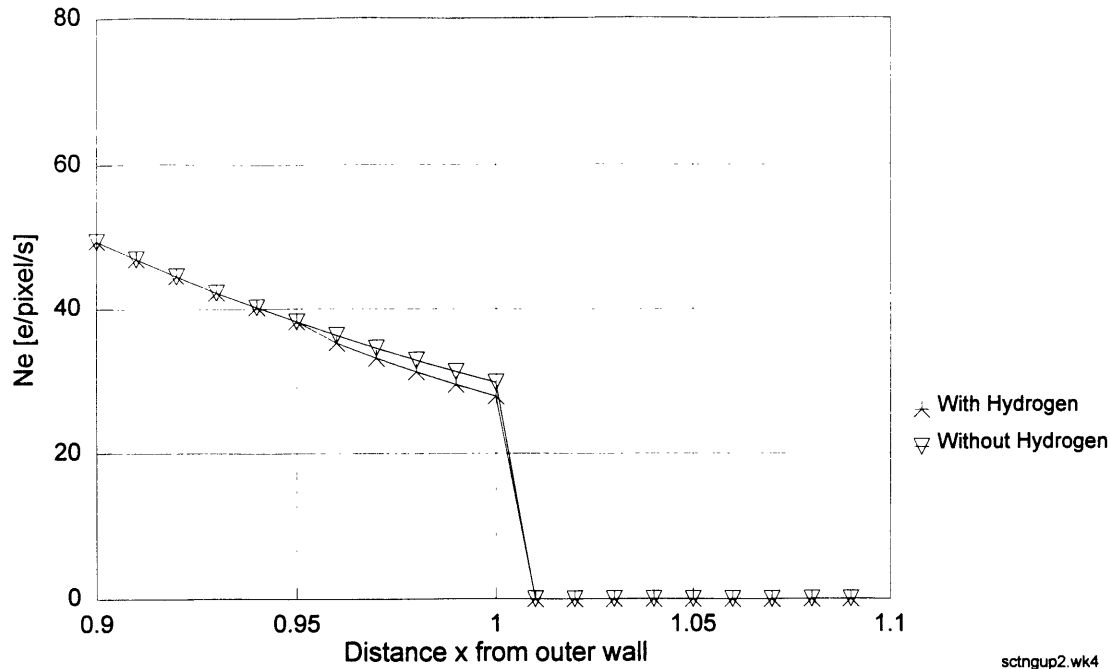
Figure 18. High scintillator screen conversion factor $N_\gamma = 2.6 \times 10^3 \; e/_n$.

The importance of this transformation factor is shown clearly by the figures above. A higher N_γ results in a larger amount of photons being produced which not only influences the absolute signal but also the differential signal.

4.2.6 Variation of Lens Characteristics

a.) Variation of the largest aperture (minimum F-number) of the lens: For a fixed focal length lens, this number is given by the lens geometry and construction. A zoom lens will have a variable aperture, the F-number is different for each focal length. The lowest F-number (largest aperture) normally coincides with the shortest focal length on zoom lenses (F-number = focal length / diameter).
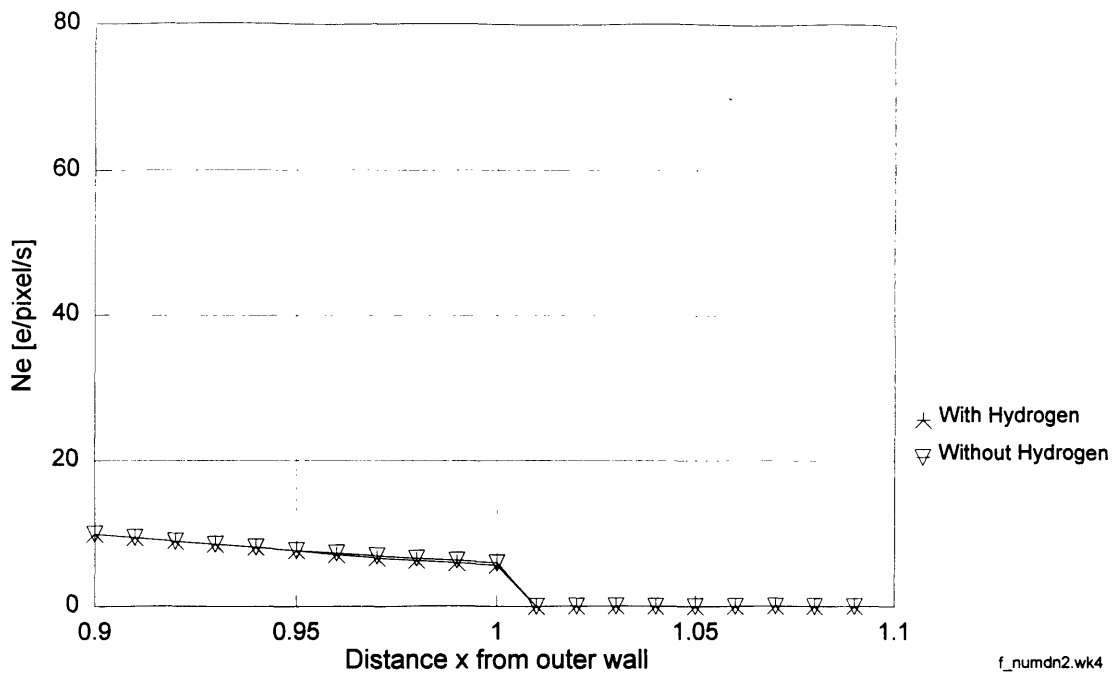
Figure 19. Decrease in the light-gathering capability of the lens (higher F-number). F = 1.8
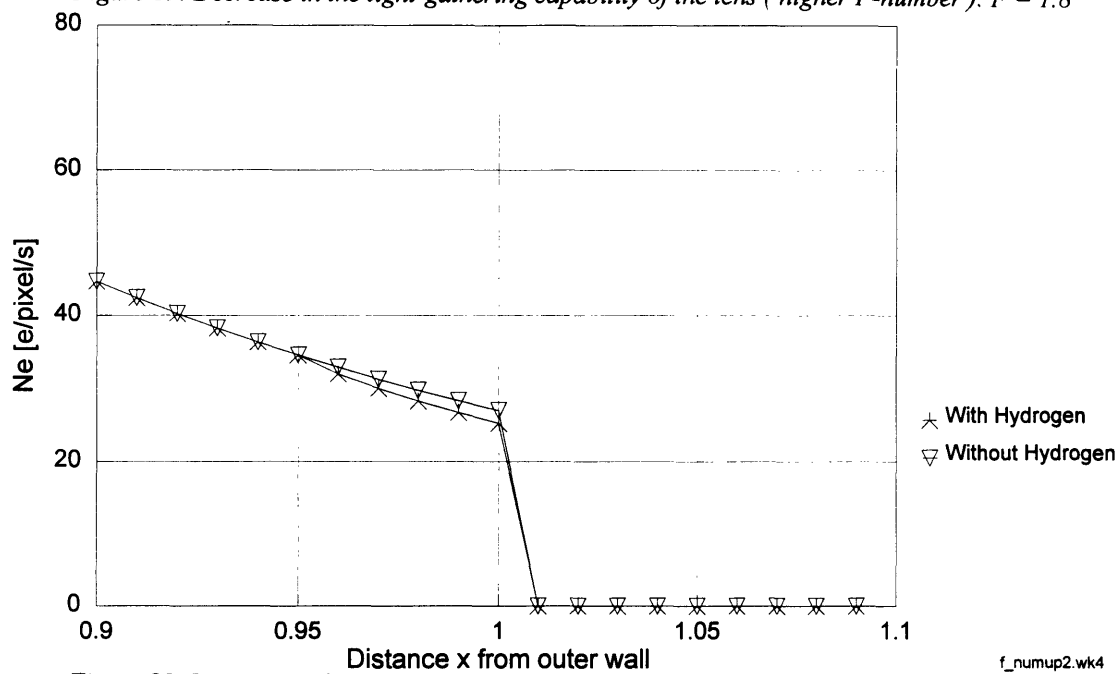
Figure 20. Increase in the light-gathering capability of the lens (lower F-number). F = 0.85.

The F-number is squared in the denominator of the factor L, therefore the signal at the CCD-output reacts proportionally to the inverse of the square of the change. This can be explained by the optical characteristics, as an increase in the F-number signifies a decrease in the diameter of the opening in the lens through which light passes. The area of this opening is relevant, this is proportional to the square of the diameter.

b.) Variation of the lens efficiency: This number is mainly influenced by the quality of the lens, although thin layers of dust or dirt on the outside surfaces of the lens where the light enters can also have a noticeable effect.
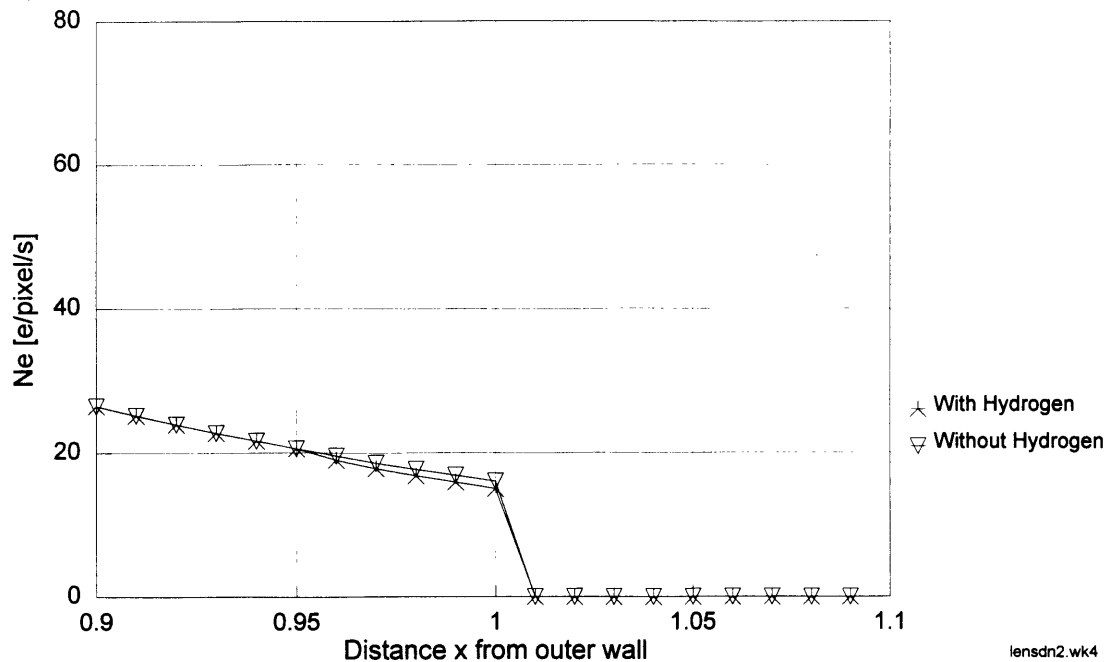
Figure 21. Decrease in lens efficiency, $\varepsilon_l = 0.7$.
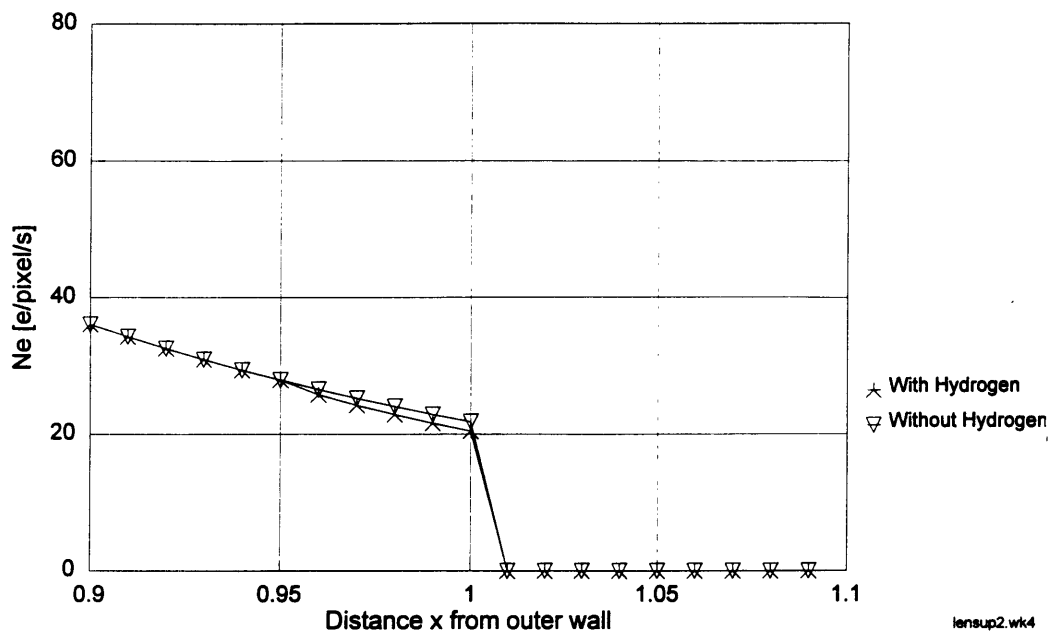
Figure 22. Increase in lens efficiency, $\varepsilon_l = 0.95$.

The efficiency factor ε_l influences the amount of photons that are lost through scattering on transmitting the lens.

4.2.7 Variation of the Characteristics of the CCD-Chip

a.) Variation of the number of pixels on the CCD-chip: CCD-chips are supplied by various manufacturers in a multitude of forms. In a CCD-camera system by one given manufacturer, there normally is a choice of CCD-chips, differing in sizes, qualities and chip-manufacturers. The most commonly used CCD-chips are of square or rectangular (close to square) geometry. Some manufacturers produce their chips with the number of pixels in both dimensions corresponding to potentials of 2, e.g. 512 x 512, 1024 x 1024 or 2048 x 2048 pixels.
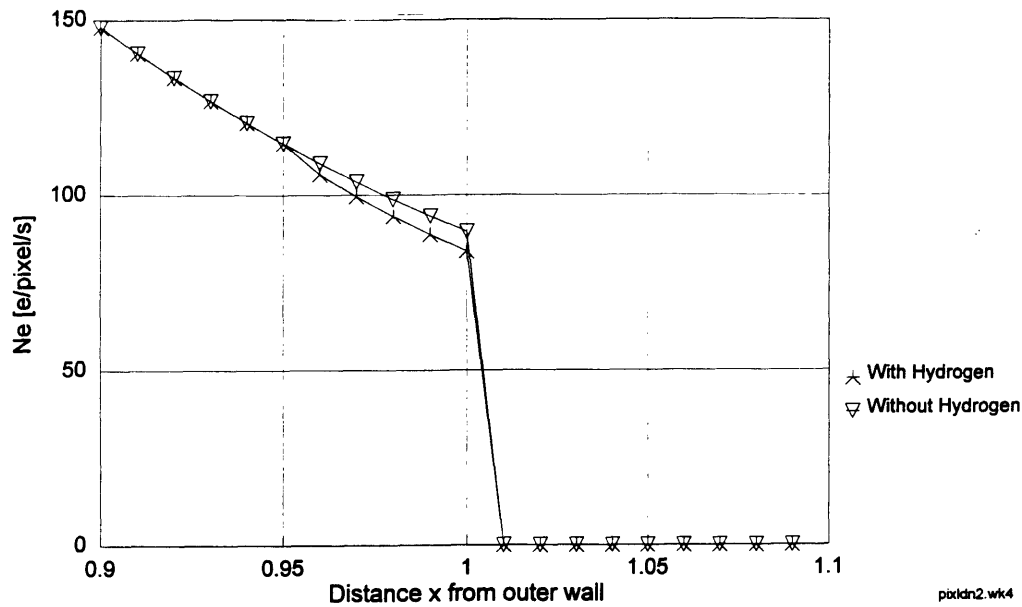
Figure 23. Reduction in CCD-chip size to 512 x 512 pixels. Pixel size 15 μm.

100

80

Ne [e/pixel/s]

60

40

20

0

0.9　　　　0.95　　　　1　　　　1.05　　　　1.1

Distance x from outer wall

⚹ With Hydrogen
▽ Without Hydrogen

pixlup2.wk4
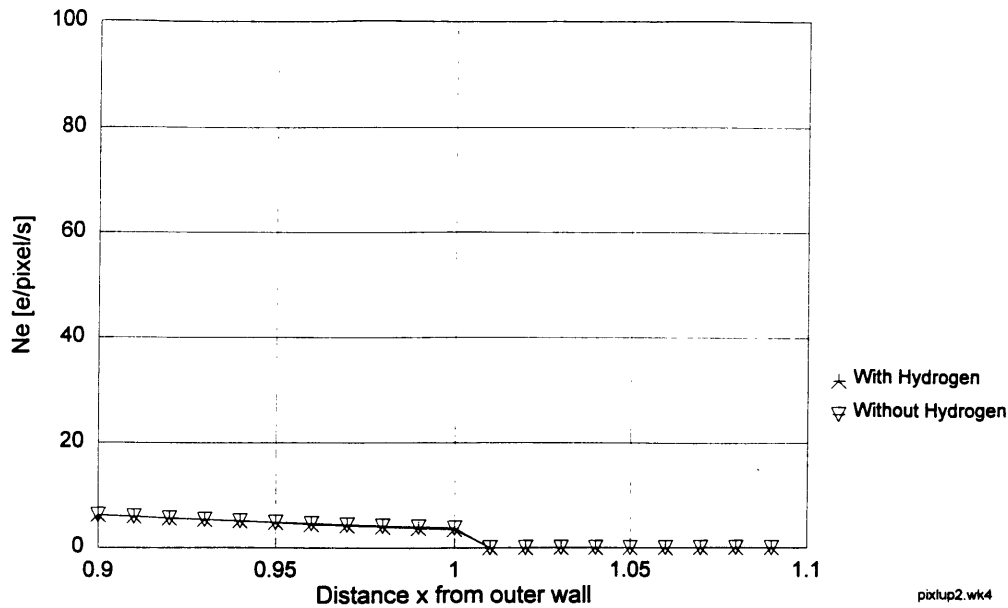
Figure 24. Increase in CCD-chip size to 2048 x 2048 pixels. Pixel size 15 μm.

The effect on the output signal of the CCD-chip is quite marked. Similar to an increase in object size, a reduction of the number of pixels gives a larger number for m. For large numbers of m, approximation 4.2 can be utilized. The dominating effect thus is the influence on the ratio of object area to total number of pixels. One can also explain this in a more descriptive manner, by saying that the available light from the scintillator screen has to be concentrated onto a smaller total number of pixels, therefore giving a higher light intensity per pixel.

b.) Variation of the pixel size: The sizes of a single pixel is mostly given by the manufacturer of the chip. Pixel sizes can vary between 6 μm up to 30 μm and are dependent on the manufacturing process.
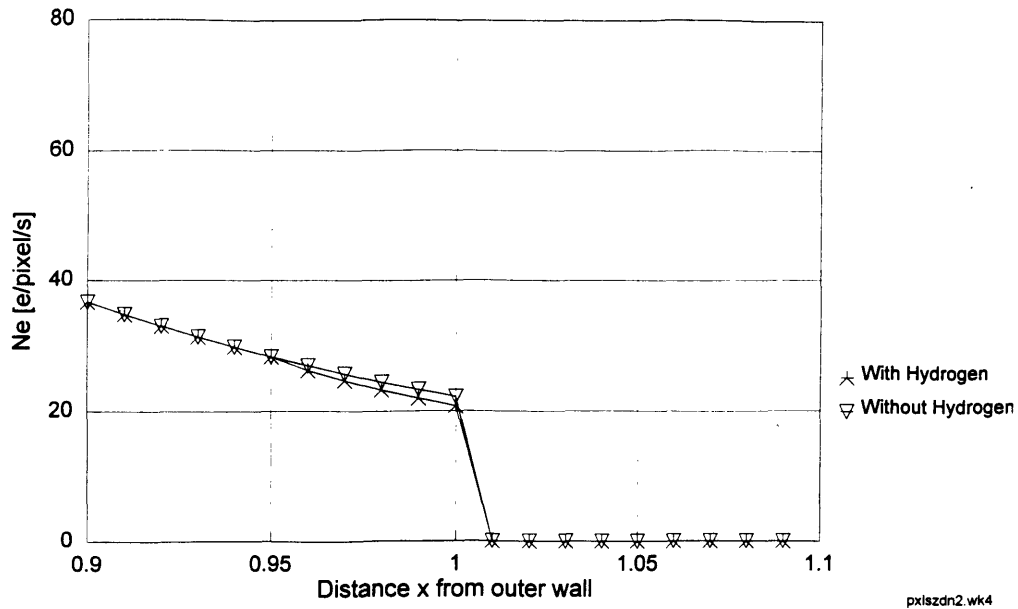
Figure 25. Reduction of pixel-size to 8 μm.
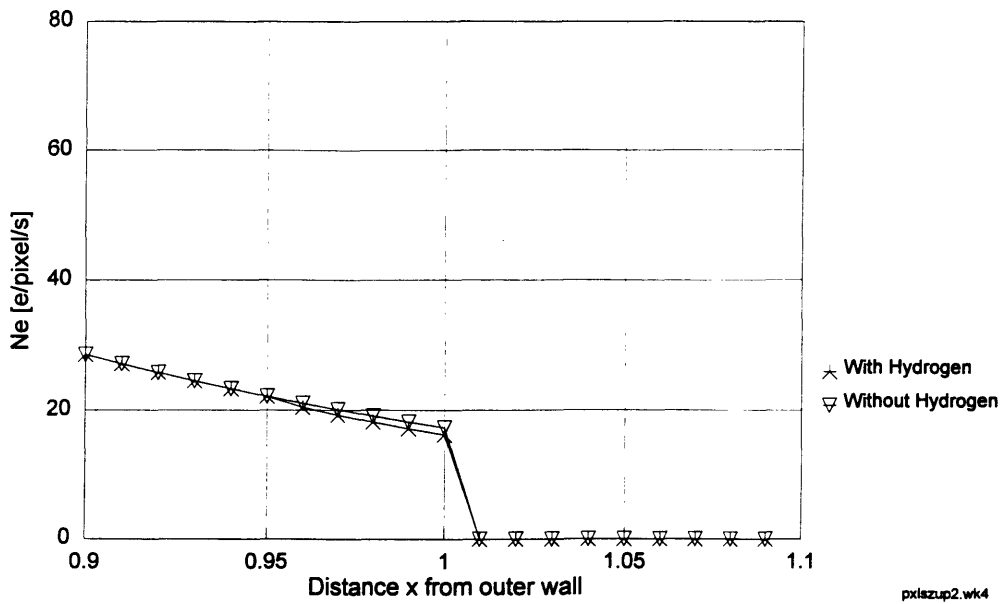
Figure 26. Increase of pixel-size to 22 μm.

The signal at the CCD-output changes very little. This is the effect of a change in the numerical value of m, showing that m is still small enough in these two cases that approximation 4.2 gives somewhat different results than the correct equation 4.1. The ratio (A_i / $\#_p$) does not change. Furthermore, the size of the CCD-chip changes, as the number of pixels in one dimension are kept constant. Therefore, the available light from

65

the scintillator screen has to be spread out over a larger total CCD area. The change in area of one pixel is directly proportional to the total area change, hence the larger pixel does not gather more light.

c.) Variation in the quantum efficiency of the CCD-chip: This number is most easily changed by varying the wavelength of the light from the scintillator. The CCD-chips in use today tend to have a higher quantum efficiency in the red-ranges.
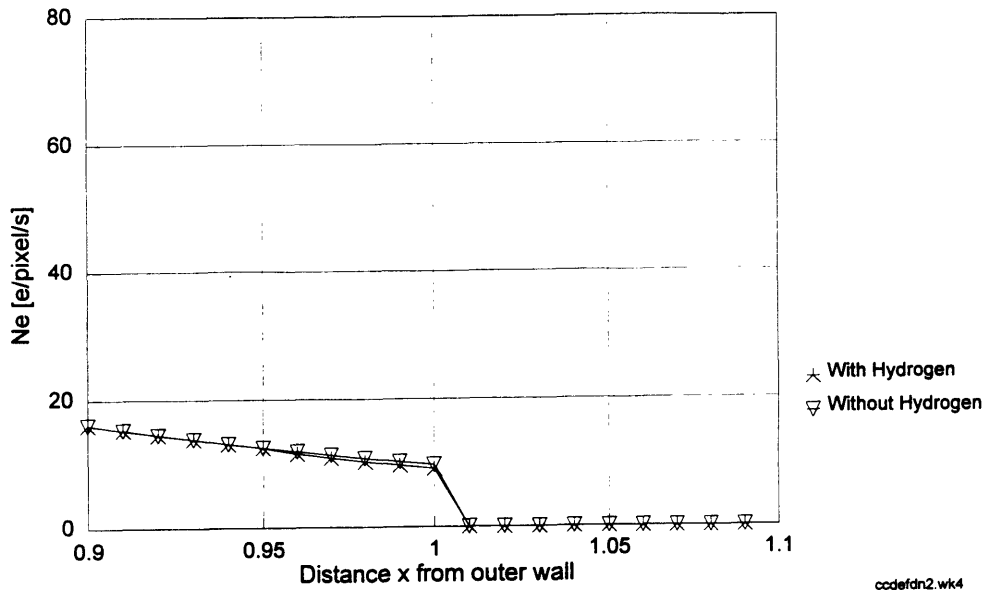
Figure 27. Reduction in quantum efficiency of the CCD-chip. $\varepsilon_q = 0.15$.
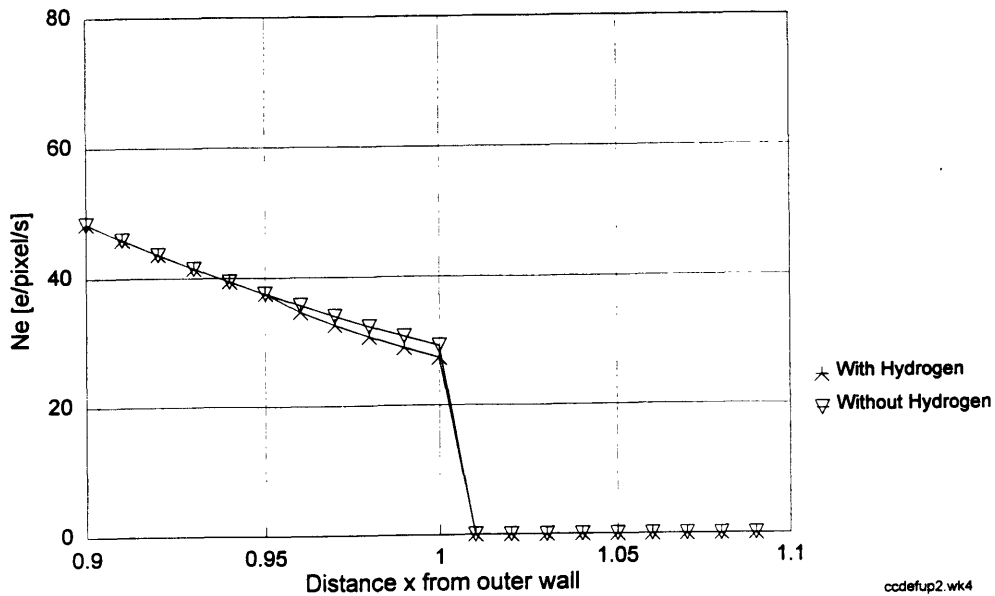
Figure 28. Increase in quantum efficiency of the CCD-chip. $\varepsilon_q = 0.45$.

66

4.2.8 Summary of the Variation of Parameters

The results of the changes in the input parameters of the spreadsheet agree with the physical-optical characteristics of the system. It can therefore be concluded, that the applied modeling process is correct in the basic form.

The properties of this system for NDT can be subdivided into two categories:

1. Parameters which can be changed by the operators of the system.

2. Parameters which are given by physical or operational characteristics and can not be changed by the operators.

In order to make the system more capable for the task of hydrogen detection, the most effective parameters out of the first group are of interest. Efficiency in this sense is defined by the ease of changing the parameter compared to the magnitude of the change in the resulting signal. Technical limitations have to be taken into account for the possible magnitude of a change. One example is given here: It is simple to enlarge the object image size by a factor of two, possible to increase the source flux by a factor of two but practically (and financially) impossible to do the same with the lens efficiency.

Each variation has been evaluated separately, with the other parameters kept constant at the base case level. In a real system, this is not necessarily the way modifications will be done. To increase the signal level at the CCD, it is quite well possible to modify two components slightly and get the same effect as would be achievable if either of them was changed to a greater extent. This can have advantages on the technical as well as economic side. The model is a useful tool to evaluate such modifications.

4.3 Modeling of Real Components

In this chapter the true numbers of real, commercially available components are used as input for the model. This will give a first indication of the output signal that can be expected at the CCD-chip and allow comparisons to noise levels. Some of the numbers that have been used in the preceding chapters are quite representative of real components,

some small corrections might have to be applied. On the other hand, some numbers can not be given definitely until the real component has been tested specifically for the unknown characteristic. In this case, reasonable assumptions will have to be taken.

4.3.1 Evaluation of Different CCD-Camera Systems

There are at least 15 to 20 manufacturers offering some kind of CCD-camera equipment that might qualify for the proposed NDT-system. In a first step, these had to be narrowed down to four or five systems that could then be evaluated in more detail. Certain minimum demands were set up for a first sorting, this helped to reduce the number. Some basic demands are:

- Cooled camera

- Choice of several CCD-chips

- Minimum number of pixels on chip ~ 500 x 500 pixels

- Variable shutter speed

- Controller integral part of system

- Interface to common computer system (PC, Mac, UNIX-workstation)

- Fast image readout

- Available (with reasonable delivery times)

- Known manufacturer with good standing in industry and after sales service

The initial group was represented by manufactures such as Sony, Hamamatsu, Spectra Source, Princeton Instruments, Tektronix, Santa Barbara Instrument Group, Photometrics, Dalsa, etc.

After the initial sorting of systems based on product catalogs using above criteria, four relevant manufacturers were found with the following systems:

Table 2. Relevant CCD-camera systems manufacturers for closer evaluation.

Manufacturer	Systems :			
Hamamatsu	CD 4880			
SpectraSource	HPC - 1	HPC - 2	MCD 1000	MCD 1200
Princeton Instr.	ST 130	ST 138		
Photometrics	ATC 200	PXL - 1300		

For a second, closer evaluation of these systems, the manufacturers were contacted and additional technical and pricing information demanded. All this information was closely compared and some numbers inserted into the spreadsheet program to compare results. In this category, the results were close together and did not give definitive indications for one system. In the end, three systems were taken into the final judgment (Prices:1993):

1. Hamamatsu with the C 4880 system. Includes cooled camera, controller and interface card, no software; readout modes: 10 bit 10 MHz, 12/14 bit 300 KHz; Grade 3 CCD-chip by TI (TC 215), 1024 x1024 pixels, 12 μm; Price: $ 36,150 (+) for PC-base.

2. Princeton Instruments with the ST 138 Controller based system. Includes cooled camera, controller, interface card, all necessary signal cabling and software; readout modes: 12 bit 1MHz, 16 bit 500 KHz; Grade 3 CCD-chip by EEV, 1142 x 1252 pixels, 22 μm; Price: $34,350 for PC-base.

3. Photometrics with the PXL - 1300 system. Includes cooled camera, controller, interface card and software; readout modes: 12 bit up to 1.5 MHz; Grade 3 CCD-chip by Kodak (KAF - 1300L), 1280 x 1280 pixels, 16 mm; Price: $ 39,380 for PC-base + $ 1'800 for first day installation in Eastern USA.

In this phase, the Princeton Instruments representative agreed to supply us with a loan system for about one week. This would give an excellent opportunity to test the capabilities and user interface and gain further knowledge about such systems. Some of the tests are described in chapter 6.

After a final comparison of price to feature ratios, delivery times and the interest of the manufacturer in actually selling and supporting his product, the Princeton Instruments System was chosen. Delivery should take place end of December 93 / beginning of January 94.

4.3.2 Modeling of the Princeton Instruments System

The components giving the input parameters for this calculation are listed below:

Source:	$N_0 = 5 \times 10^6 \; n / cm^2 \; s$	Thermal neutrons
Object:	Steel pipe, $\rho_{Fe} = 7.88 \; g / cm^3$ $\mu_{Fe} = 0.15 \; cm^2/ g$	$r0 = 9$ cm, $r2 = 10$ cm Image size 9.12 x 10 cm^2
Hydrogen loading:	200 ppm, uniform distribution	$r1 = 9.05$ cm
Scintillator Screen:	$\varepsilon_d = 0.15$	$N_\gamma = 1.7 \times 10^5 \; e / n$
Lens: [7]	$\varepsilon_l = 0.85$	$F = 0.85$
CCD-chip	$\varepsilon_q = 0.3$	1142 x 1252 pixels, 22 μm, image area: 2.51x2.754cm^2
Other parameters:		
Atten. coefficients:	$\mu_H = 22 \; cm^2 / g$	$\mu_w = 15 \; cm^2 / g$
Density:		$\rho_w = 1 \; g / cm^3$
Calculated factors:	$m = 3.63$	$L = 0.01614$
	$\mu_{res} = 0.1544$	

[7]This is the data for the Fujinon CF25L lens with a C-mount. Most likely an other lens will be used on the definitive system which has a Nikon-mount. It can be assumed, that a lens with very similar characteristics would be chosen.

The Princeton Instruments system allows the camera signal to be read out in standard or in MPP mode [8]. Although MPP-mode reduces the dynamic range, this should not lead to problems in the proposed application.

The readout noise for this camera is 4 to 6 e RMS / pixel at 50 KHz and 8 to 11 e RMS / pixel at 200 KHz. Readout noise is proportional to the third root of the frequency, so the expected readout noise at 500 KHz is 11 to 15 e RMS / pixel.

The dark noise is about 6 e/pixel s at - 45°C in standard mode and approximately 0.03 e/pixel s in MPP mode.

The next two figures show the signal at the output of the CCD-chip in relation to the distance of the outside pipe wall. The second figure is an enlargement of the inner pipe wall region.
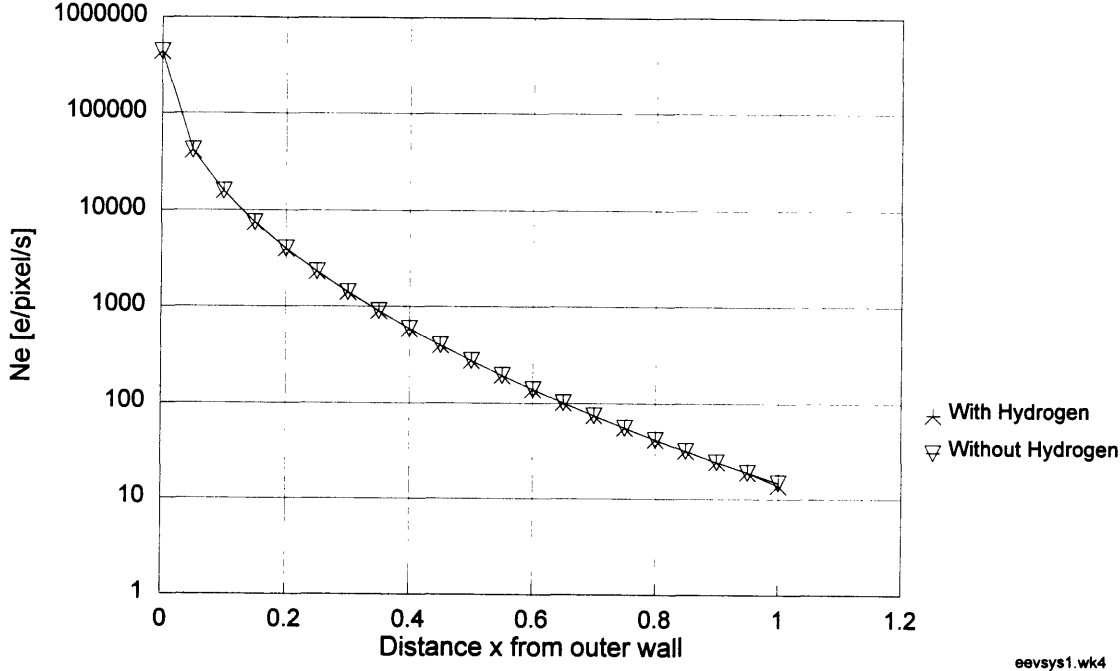
Figure 29. CCD-output signal N_e of PI camera system vs. distance from outside pipe wall.

---

[8]MPP stands for Multi-Pinned-Phase. It reduces the dark current generated during integration by a factor of 20. In many cases, MPP technology provides performance equivalent to cyrogenic cooling.
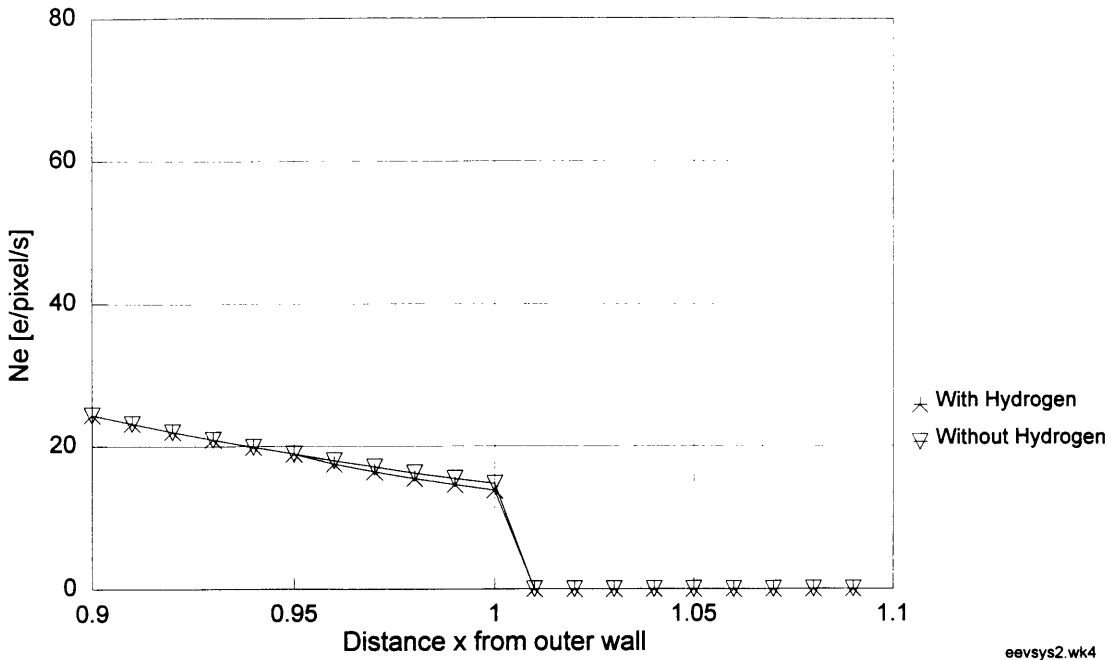
Figure 30. CCD-output signal N_e of PI camera system. Enlargement of region adjacent to inside pipe wall.

All these graphs display the signal expressed in units per second. During a neutron radiography experiment, the object will be in a constant source flux N_0. The exposure time has to be set up in the camera control software, the controller unit then regulates the opening time of the shutter on the camera head. The exposure time can basically be chosen in the software, any value between 0.001 s and hundreds of seconds can be chosen. In a real experiment, the minimum exposure time is given by the noise levels of the system. The signal has to be larger than the total noise. Depending on the signal strength and the noise characteristics of the system, the minimum exposure time has to be adjusted accordingly. All the following Figures are done for the flux corresponding to the position at the inside wall, i.e. distance x = 1 cm.
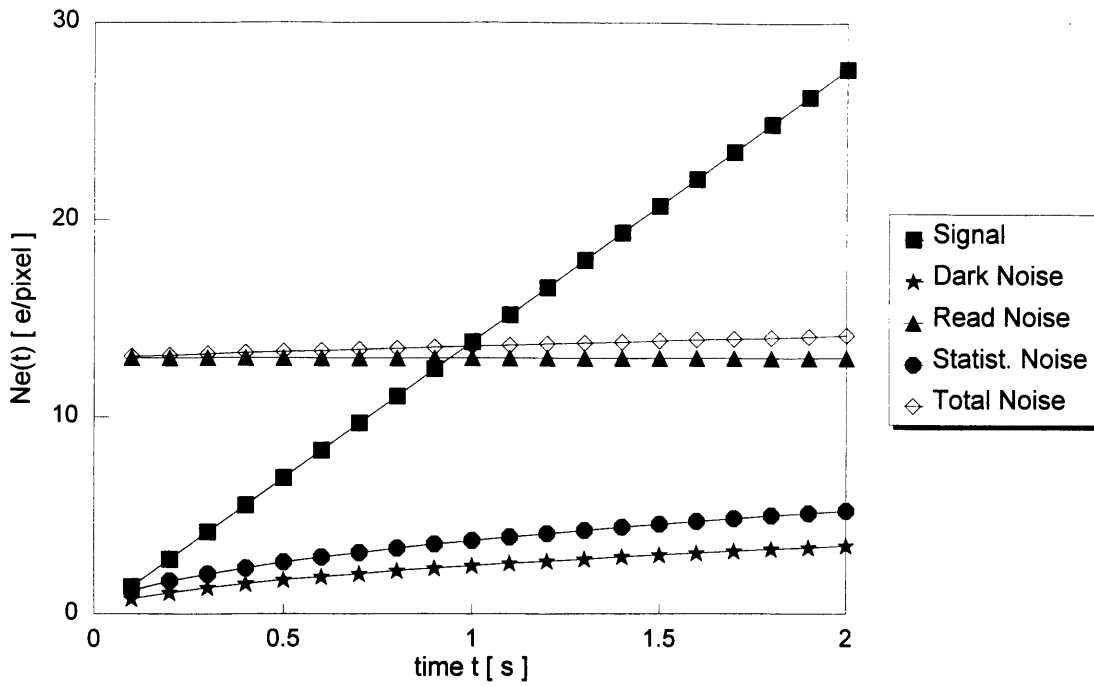
eevnsbs1.wk4

Figure 31. Output signal at CCD and noise levels vs. exposure time. Standard readout mode. (PI

system)

In this mode, the minimum exposure time for the signal to be higher than the system

noise is at one second. Read noise is constant over all times as it is given in electrons

RMS per pixel, which makes it independent of exposure time.
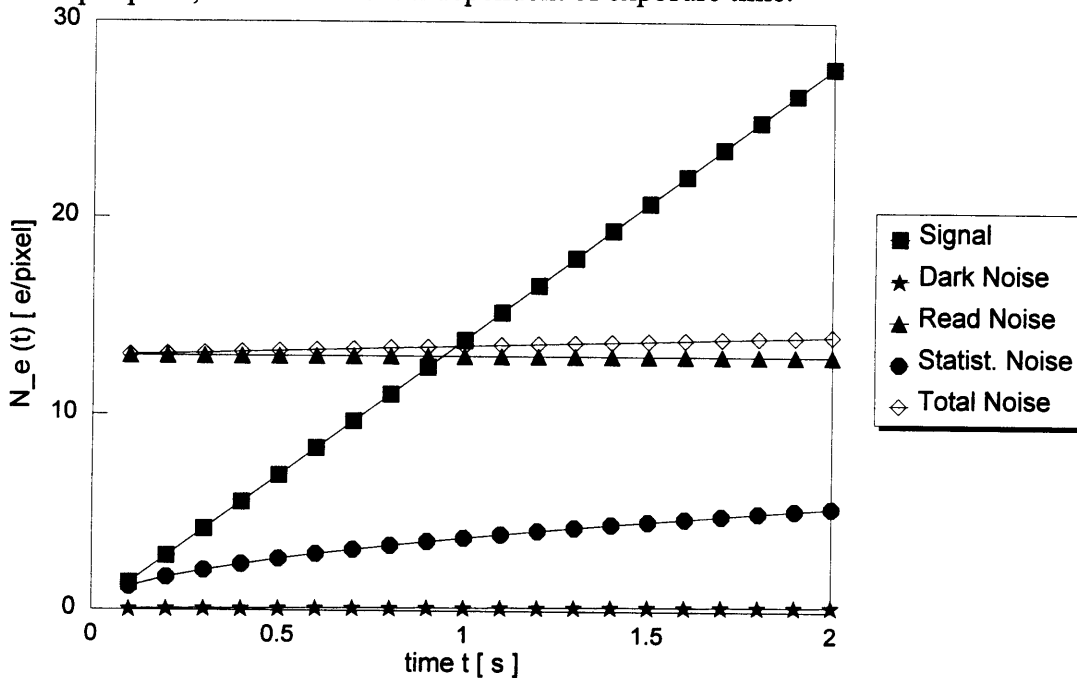
Figure 32. Output signal at CCD and noise levels vs. exposure time. MPP mode. (PI system)

Even though the dark noise is considerably lower under MPP-mode, the requirement for the minimum exposure time does not change much. In this mode, dark noise is basically negligible in comparison to readout and statistical noise.

The signal-to-noise ratio (SNR) can be calculated as a function of exposure time utilizing equation 3.30. This will give the same information concerning the minimum exposure time, the criteria being the time where the SNR is greater than one. The relationships between dark noise, readout noise and the signal can also be made visible.
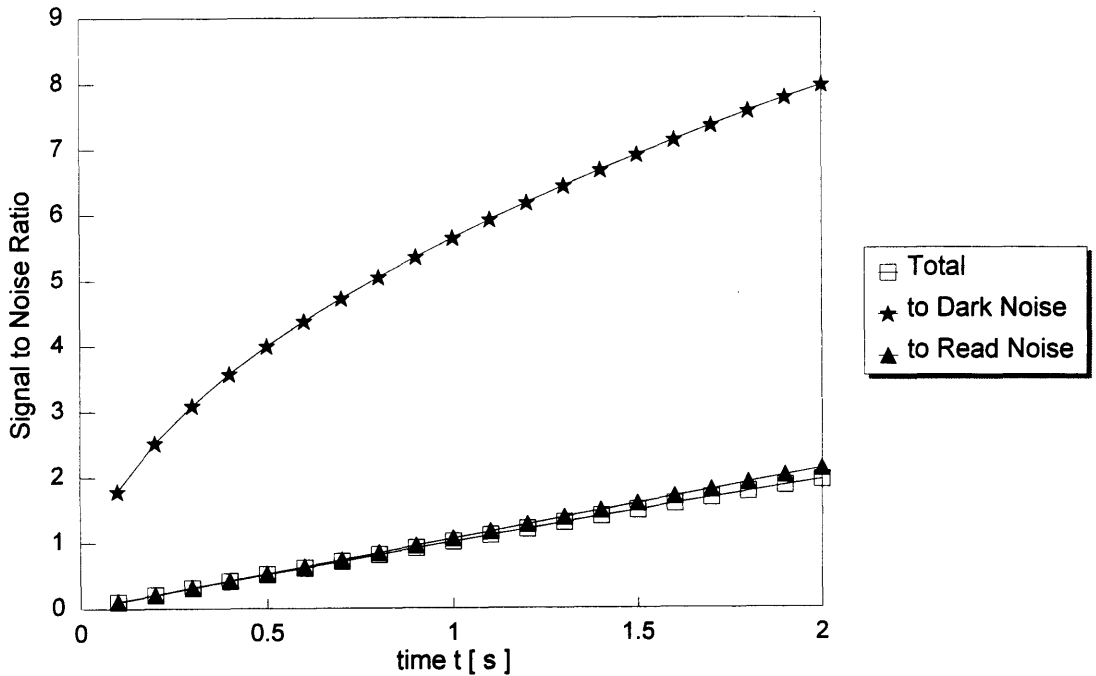
eevsnr1.wk4

Figure 33. Signal-to-noise ratio for PI system operating under standard mode.
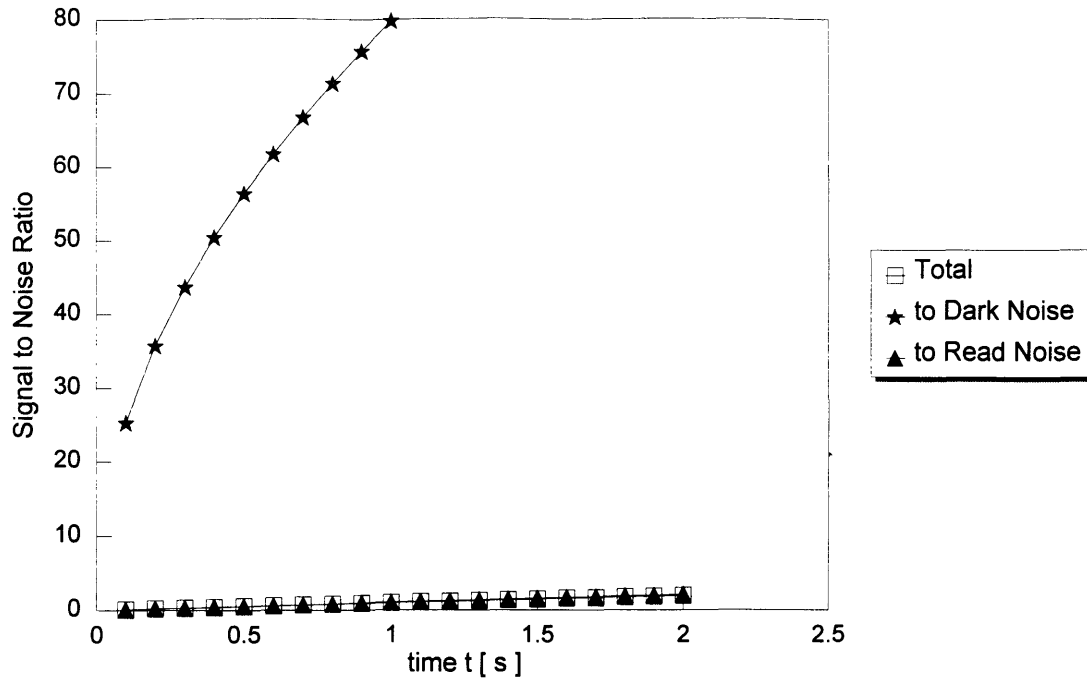
eevsnr2.wk4

Figure 34. Signal-to-noise ratio for PI system running under MPP-mode.

The large influence of MPP-mode on the Signal-to-Darknoise ratio is clearly visible in

Figure 37. The same is of course valid here as for Figure 35, the system noise is

dominated by readout and statistical noise, so the large ratio for the dark noise in MPP-

mode does not have a noticeable influence on the total SNR.

4.3.3 Modeling of Various Pipe Dimensions

So far, one fixed geometry has been assumed for the object. This does not represent

reality very well, as many different pipes will have to be examined. Assuming constant

material properties, i.e. the same density for steel, the same attenuation coefficients etc.,

the influence of changing the pipe diameters has to be studied. Different diameters

change the wall thickness and the distances the neutron beam is being attenuated (y1, y2,

y3). As these numbers are in the exponential part of equation 3.26, a considerable

influence on the detected flux at the scintillator screen can be expected. In the following

figure, the signal at the output of the CCD-chip is displayed for the PI camera system for

the distance x corresponding to the inside wall. The hydrogen loading is 200 ppm, all other parameters are as given in chapter 4.2.1.
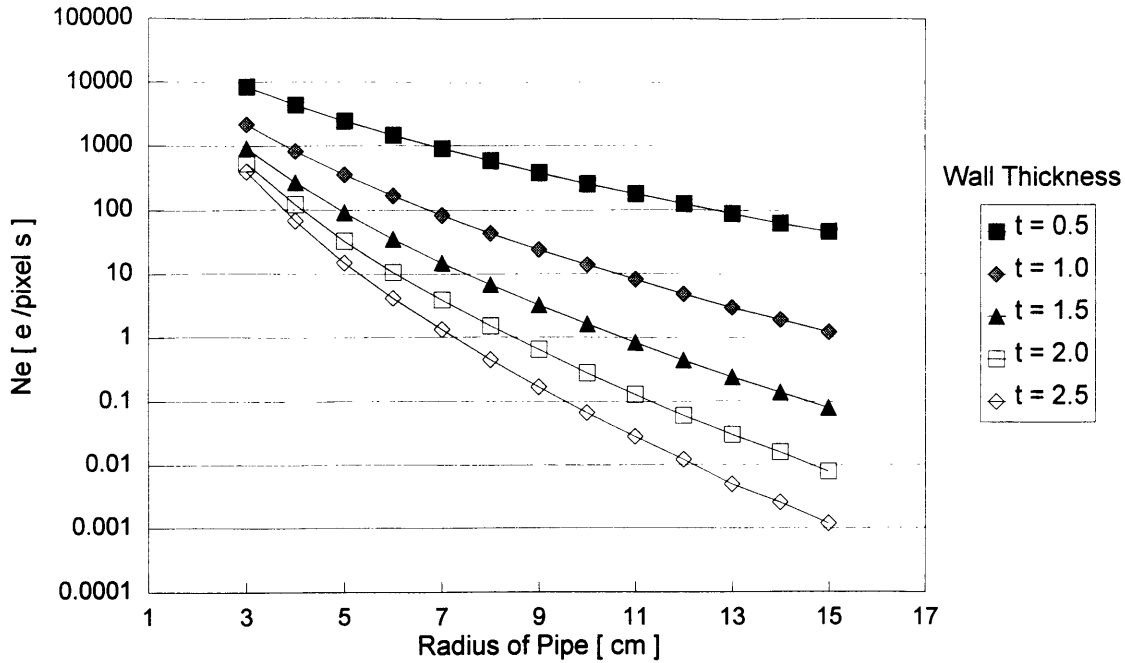
Figure 35. Output signal at CCD-chip for various outside pipe diameters and wall thicknesses.

It can be seen, that with larger pipes and greater wall thicknesses the absolute signal decreases rapidly. The size of the differential signal ΔN_e changes proportional to the inside radius of the pipe, as y2 grows with larger r0. Although this would be a positive effect for the detection of hydrogen in larger pipes, the low absolute signal level will be difficult to discover in the noise of the system.

4.4 Error Sensitivity

The numbers given so far have been absolute, without any margins for error. In a real experiment, certain errors are unavoidable. These errors have a number of sources, e.g. measurement errors, rounding errors in calculations, readout errors, etc. Some values are more susceptible to these errors than others, four likely error sources for this experiment have been picked out. These are:

- Source flux

- Lengths (Diameter, radius)

- Material density

- Mass attenuation coefficient

In the following, the effects of a small error in any single one of these values on the resulting signal at the CCD-chip will be shown. This is done by varying the value of each parameter by the error and studying the effect on the result. For each value an error of $\pm$ 1 % was assumed. The effect on the result is given in % change from the initial result with all parameters at their error-free values.

Source flux:

Table 3. Effects of 1 % error in source flux on signal at CCD-chip.

Source flux N_0	- 1 %	+ 1 %
Change in result	- 1 %	+ 1 %

N_0 is a linear multiplicator in equation 3.26 so a 1 % error has the same outcome in % on the result.

Radius:

Table 4. Effects of 1 % error in radius on signal at CCD-chip.

r0 (Inside Rad.)	- 1 %	- 1 %	+ 1 %	+ 1 %
r2 (Outside Rad.)	- 1 %	+ 1 %	- 1 %	+ 1 %
Change in result	+ 11 %	- 61 %	+ 181 %	- 10 %

The largest consequence for the result (N_e = + 181 %) is brought about by the case in which the inside radius r0 is 1 % larger and the outside radius r2 is 1 % smaller than measured. The wall thickness is reduced from 1 cm to 0.81 cm (- 19 %) with considerable effects on the values of y1, y2 and y3. In all these cases, the ingression of hydrogen into the inside wall was left at a constant 0.05 cm, i.e. r1 is either 8.96 cm or 9.14 cm.

77

Density:

Table 5. Effects of a 1 % error in density on signal at CCD-chip.

Density of steel	- 1 %	+ 1 %
Change in result	+ 11 %	- 10 %

The density is in the negative exponent in equation 3.26, so the effects on the result are inverse and noticeable.

Mass attenuation coefficient:

Table 6. Effect of a 1 % change in attenuation coefficient on the signal at the CCD-chip.

μ_{Fe}	- 1 %	- 1 %	+ 1 %	+ 1 %
μ_H	- 1 %	+ 1 %	- 1 %	+ 1 %
Change on result	+ 11 %	+ 11 %	- 10 %	- 10 %

The effects of the changes in the attenuation coefficient of hydrogen are negligible in this example. The consequences of the errors in μ_{Fe} are comparable with those of ρ_{Fe}.

Summary:

Opposing errors in the measurement of the radius have the largest effect on the numerical value of the signal at the CCD-output. Although the outside diameter of a pipe can be measured quite precisely with vernier calipers or similar tools, this might not be the main cause for the error. It can be imagined that a pipe used for the transport of liquids is not produced with tight tolerances and variations in the outside diameter and the wall thickness occur in axial as well as a radial directions. Manufacturers of pipes usualy control wall thickness, therefore a change in the outside radius will normally coincide with a change on the inside radius (" - - " or " + + " cases in table 4).

These errors signify deviations from the expected values as given by the calculations of the model. In a real NDT-system, the absolute level of the signal may be different to the calculated numbers, as some uncertainties about the characteristics of the components remain. Therefore, these errors are less important than they may seem, as long as they do

not reduce the signal to an undetectable level. If this happens, an excellent indicator is given that some input value of the model is noticeably different from the real value. An analysis of this difference can then lead to the discovery of a fault in the system.

CHAPTER 5

EXPERIMENTS

5.1 Preliminary Experiments

5.1.1 X-Ray Experiments with SBIG CCD-Camera

In the Spring of 1993 it was anticipated that maybe some neutron radiography

experiments could be run using the Santa Barbara Instrument Group Star Tracker 4

(SBIG ST4) camera. This is a small, thermoelectrically cooled camera system developed

mainly for astro-photography. It is also possible to use it as an imaging system together

with a personal computer. The system includes the camera, a separate controller, interface

and power cables and imaging software. The interface to a personal computer is done via

a RS-232 serial port. The price for the complete system is $ 890.-

Table 7. Technical specifications for SBIG ST4 camera.

Active area of CCD	2.5 x.2.5 mm^2
Number of pixels	192 x 165
Pixel size	13.75 x 16 μm
Exposure time range	50 ms to 300 s
Readout noise	150 e RMS / pixel
Dark noise	371 e / pixel s (at T = 21° C, lower when cooled)
Signal processing dynamic range	8 bit

The CCD-chip used is a Texas Instruments TC210, the specifications for readout noise

and dark noise have been taken from the TI Area Array Image Sensor Products Data

Manual. Comparing the technical specifications of this camera to those of the Princeton

Instruments system it is easy to see where the difference in price comes from.

Additionally, the controller on the PI system is considerably more sophisticated and much faster at a larger dynamic range.

Setup:

A test rig was set up using an X-ray tube as source and an X-ray phosphor screen. All the components were placed along the axis of a piece of 6 inch plastic drainage pipe. The phosphor screen was supplied by MCI Optronix Inc. of Cedar Knolls, NJ and is a "PFG" ZnCdS:Ag type. The emission efficiency is 19 % with a green emission color (peak at 530 nm).

The image size on the phosphor screen was set at 2.5" x 2.5". The lens used is the FUJINON CF25L described earlier with a focal length of 25 mm and a maximum aperture of 0.85. The image to CCD distance was calculated at 39".

A considerable problem was encountered in trying to match the lens to the camera, as the lens has a C-mount and the camera only has a tube that can be slid into the eyepiece mount of a telescope. After completely unsuccessful attempts to locate an adapter it was decided to machine the necessary part by ourselves.

The whole system was set up with the pipe standing vertically, the X-ray tube at the top and the camera at the bottom. Openings in the tube allowed the manipulation of the object and the camera lens. Shielding was provided by sheet lead wrapped around the outside of the plastic pipe.

The X-ray tube is a Kevex Type 5010 SW with the following specifications:

Table 8. Technical specifications for Kevex K 5010 SW X-ray tube.

Max. Volt:	50 kV
Max. Current:	1 mA
Max. Power:	50 Watts
Target Material:	Tungsten

Test runs:

The X-ray tube was run at slightly below 40 kV and 180 μA throughout the experiment as a fault in the power amplifiers caused a cut out at voltages higher than ~ 40 kV.

After the initial focusing and aperture setup, some tests were run with various objects to evaluate the general imaging procedure and get a first impression of picture quality. Large objects gave acceptable overall picture quality although a lack of detailing was noticed. In order to test the resolution, a lead calibration plate with varying distances of line pairs was used. The calibration plate starts at the largest spacing of 0.6 line-pairs (LP) per mm and goes up to 10 ^{LP} / $_{mm}$.

The results were unacceptable. The most coarse line spacing could just be sufficiently resolved by the camera. The next two finer spacing already were difficult to distinguish as lines of bright and dark.
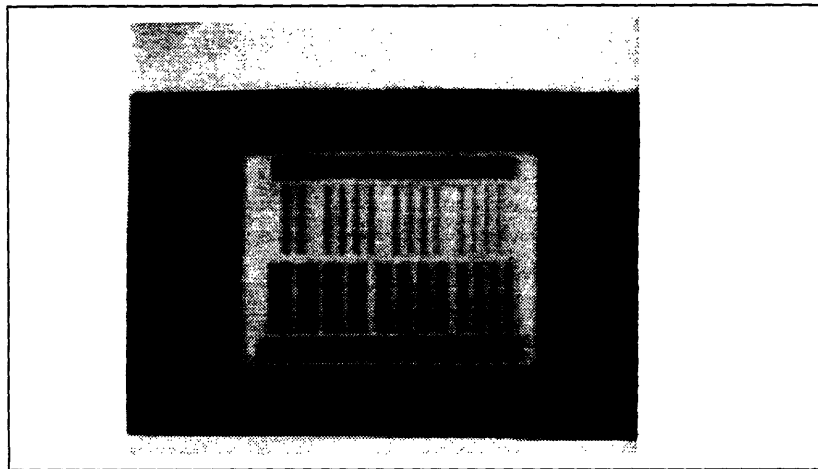
Figure 36. Printout of screen image of X-ray calibration plate. Most coarse line spacing at bottom left corner of plate (0.6 LP / mm). Negative image is displayed.

Contrast has been enhanced over the original picture and high resolution output was chosen.

82
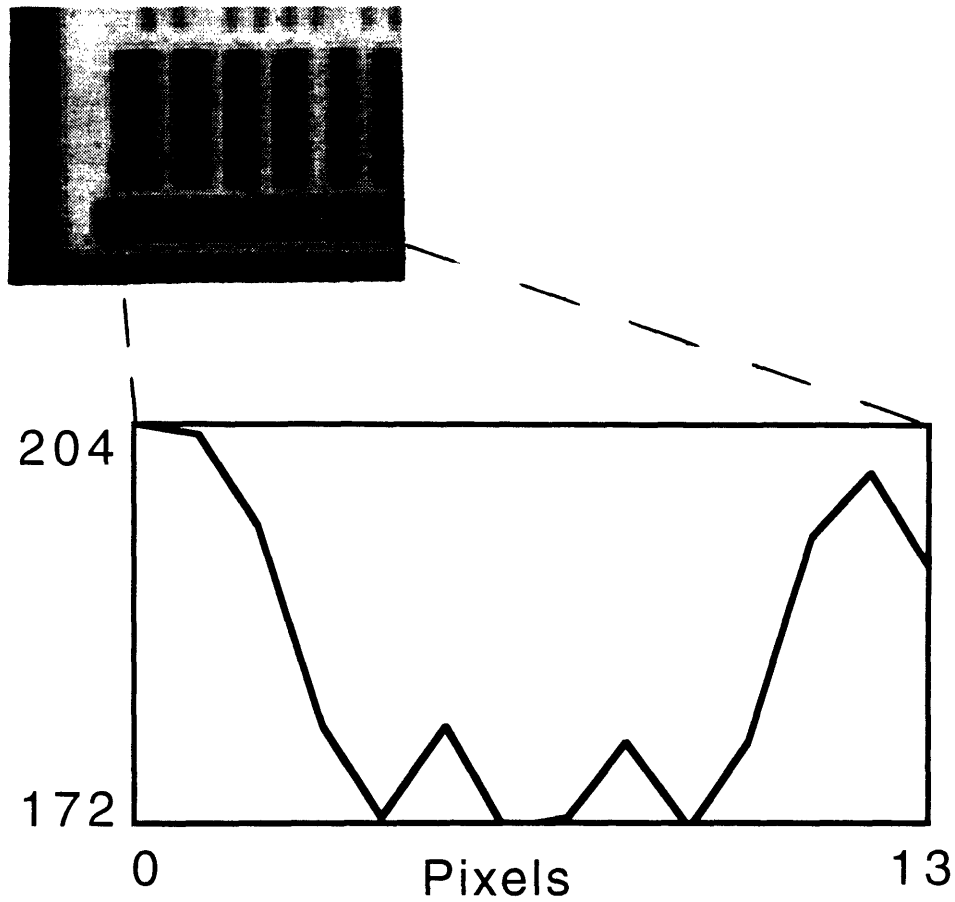
Figure 37. Printout of enlargement of figure 39. A profile plot of the intensity is below the image.

The profile plot shows that the linepair is basically being detected by one pixel and the intensity averaged out with the neighbouring pixels (low peaks). From this it is quite clear that no better resolution can be reached, as one pixel is the minimum value. The resolution of the linepairs could be enhanced by placing the calibration plate closer to the camera, but this reduces image size and has limits in the minimum focusing distance of the lens.

In conclusion it can be said that this camera system is unsatisfactory for any further experiments with X-rays or neutron radiography. The CCD-size is too small (in absolute area and number of pixels) and the noise levels to high. Therefore, these experiments were halted at this point.

5.1.2 Tests with Loaned PI Trial System

As mentioned in chapter 4, the sales manager of Princeton Instruments (Lewis I. Rubin, Ph.D., Lexington, MA, (617) 861-0360) agreed to loan us a trail system for 1 ½ weeks in the Fall of 1993. This would allow us to test the system for the suitability as an imaging system for neutron radiography. Also, it would give us the possibility to compare technical specifications and descriptions to "real-live" data, which would be useful to further evaluate all CCD-camera products that were in the closer choice.

The system supplied to us was complete by including the whole camera system as well as a PC-based computer system and monitor. The CCD-chip in the camera head was not the EEV-chip as described in chapter 4, but a smaller chip with 584 x 377 pixels. Furthermore, the controller was a ST-130 with a single slower A/D board with 12 bit @ 500 Khz. The noise levels are comparable to those of the EEV 1142 x 1252 CCD-chip. The pixel size is slightly smaller, approximately 18 μm.

Setup:

The system was set up for purely optical experiments on a table in Laboratory NW13-213. Three groups of runs were planned:

1. General imaging. Capturing an image, variable exposure times, shutter control, image display and manipulation, image analysis with supplied software.

2. Noise levels. Readout noise and dark noise, levels as a function of exposure time.

3. Resolution. Optical resolution of X-ray calibration plate.

Initial setup problems were encountered with a part not directly related to the camera system: The computer monitor did not work and had to be removed for repair. A provisional solution was found by using a different, lower resolution monitor from the Laboratory. Although this worked initially, starting up the whole system the next morning produced no picture on the provisional replacement monitor. A failure in the Video Display Card of the computer was suspected and a certain apprehension to connect

a third monitor developed. A few days later the PI sales manager returned with the original monitor where the failure had been traced to a bent pin in the video signal connector. The second monitor eventually started working on an other computer system again, the fault was not found. All this reduced the available time for the experiments considerably.

Test runs:

The tests out of group 1 went smoothly and showed the excellent possibilities for image capturing, evaluation, manipulation and analysis. The software runs under "Windows 3.1" and has the familiar user interfaces. Various statistical tools are available for image analysis. Furthermore, single pictures can be combined in different ways to allow the subtraction of dark or background noise or superimpose variations. A limitation was found in image storage for further use outside of the actual imaging software. The software can only save images in it's own proprietary form which can not be accessed by any other image enhancement/manipulation software. This is especially important as the supplied routine for producing hardcopies (printout) is unnecessarily complicated and produces very mixed results (Printout via screen capture, whole screen placed in "Windows Clipboard", has to be transferred to "Windows Paint", unneeded parts of image have to be deleted (frames, operating system information, menus), printout from "Windows Paint" but brightness and contrast difficult to regulate).

The experiments of group 2 were performed to get some information about the noise levels of the system. This was done by exposing the CCD-chip with various shutter speeds to a black box (no light source). For each exposure time, the image was recorded and analyzed. The image brightness and contrast can be manipulated in such a manner, that even though the picture should be uniformly black, various grey shades could be distinguished. A statistical analysis of the whole image area by the software then gives the minimum intensity and position, the average intensity of all pixels and the maximum intensity and position (pixel - x, pixel - y). The intensity is expressed as a numerical

value for the grey shade, with $I_{min} = 0$ = absolute black (no signal) and $I_{max} = 2^{16} =$ 65'535 ("bright white"). The intensities can then be plotted against the exposure time.
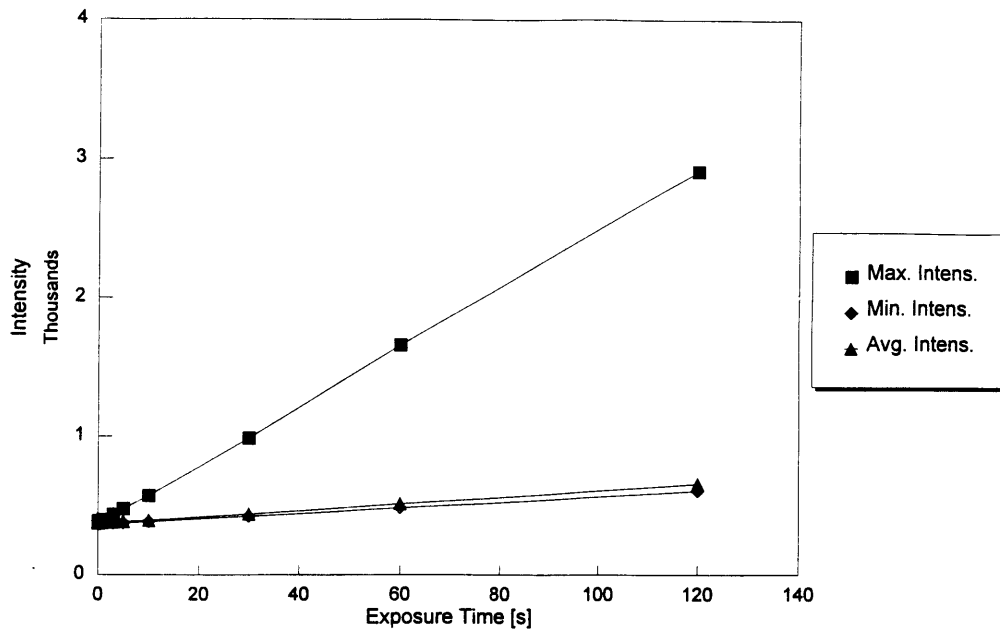
Figure 38. Princeton Instruments Trial System Noise Test. Intensity of dark frames vs. exposure

time.

The slope of the average intensity is comparable to the slope in figure 33 or 34. The average intensity of the dark frames must contain the dark noise and the readout noise. The readout noise is constant over time and corresponds to the minimum intensity value at time 0 (Practical exposure time: 0.005 s). In this case, the read noise corresponds to an intensity level of 373. One can try to correlate this intensity to a signal in $^e/_{pixel}$ by assuming that the maximum intensity corresponds to the full well capacity of a pixel. The full well capacity is 200,000 electrons. This would give a readout noise of 1'140 $^e/_{pixel}$, which is several orders of magnitude away from the real value (10 - 15 $^e/_{pixel}$). The assumption must therefore be incorrect. The real relationship would have to be found through calibration experiments (Calibration for zero offset). The noise measured by this test represents the total system noise, including noise from the camera pre-amplifier, controller and A/D converter. As such, the levels are low enough to expect a large SNR in

practical imaging. Furthermore, the " Image Subtract " feature in the software enables the average " Dark Frame " to be subtracted from the actual image.

The experiments of group 3 were conducted with the X-ray calibration plate. A light source was placed behind the calibration plate and the lens focused on the linepairs. Several runs were needed to find the optimal combination of lens aperture, contrast, brightness and intensity range. The problem with this setup is that the image properties for display on the monitor can be set up in such a way that the picture is displayed incorrectly, giving seemingly bad resolution. In the short time available, it was possible to resolve the field with 1.2 $^{LP}/_{mm}$ at an object distance of 40". This does not represent the best value, as the optimum setup had not been established. All the same, this represents a considerable improvement over the SBIG ST4 system. With the 1142 x 1252 CCD-chip and optimum setup better values can be expected.

5.2 Components Prepared for Experiments

Some components of the system have been prepared and are available for the construction of a stationary system.

1. Scintillator screen. A Nuclear Enterprises NE 426 ^{6}LiF-ZnS-Cu activated (for enhanced green output) type scintillator screen is available. It has to be affixed to the inside of the front surface of the aluminum casing.

2. Aluminum box. This supports the scintillator on one end and the camera normal to the axis source-object at the other end. The mirror is placed on a movable plate towards the back end of the casing. As mentioned before, this box is constructed of a sturdy aluminum frame with plates fixed by plastic screws. Only the top plate and the unmarked side-wall should be removed . The bottom and one side-wall are marked as " Do not remove ". This is done to guarantee the alignment of the plates and give better initial light sealing. Additional sealing can be done with black masking tape. The opening and support for the camera have not been implemented so far, as the

correct measurements will have to be taken from the real components. The cutout for the lens has to be large enough to allow adjustment (by hand) of focusing and aperture. The opening can then be re-sealed with two aluminum half-plates. Construction details and additional information is given in appendix D.

3. The order for the camera system was placed with Princeton Instruments at the beginning of November 1993. Delivery time is 45 to 60 days, so the system can be expected to arrive in January 1994. Initial tests can be run similar to those described in chapter 5.1 to check the system functions and to familiarize the operators. The system has been ordered with a Macintosh interface and the imaging software " IP Lab " by Signal Analytics Corporation, Vienna, VA. ({703}281-3277), which offers a considerably more sophisticated set of imaging options than the basic software as supplied with the loan system.

4. Computer system. An Apple Computer Macintosh Quadra 650 with a 500 MB hard disc drive, 1MB display RAM and 16" Color Monitor was recently acquired. Together with the "IP Lab" software, this will give excellent possibilities to acquire, manipulate and analyze the data from the computer system. The system speed should be sufficient to allow reasonably short acquisition and processing times. Faster speed in this area could have been reached by choosing a PC-compatible Intel 80486DX2-66 processor based local bus system. A Pentium processor or RISC processor based workstation would offer even higher speeds, but hardware compatibility and software availability problems could be encountered.

5. Mirrors. Several sizes of mirrors are available. These are all front surface mirrors so that care has to be taken during handling and installment. The following sizes are ready: 2 pieces 85 x 101 mm, 1 piece 127 x 178 mm and 1 piece 254 x 313 mm. These can be bonded to the angle-adjustable mirror back plate in the aluminum box.

CHAPTER 6

ANALYSIS AND DISCUSSION OF RESULTS

6.1 Analysis of Computer Modeling

6.1.1 Base Case and Variation of Parameters

The basic modeling of the system is a good tool to evaluate the system performance and responses. It leads to an understanding of the processes and functions involved in neutron radiography and imaging. By introducing numerical values for the system parameters, an order of magnitude can be supplied for the final signal. This is a first indicator if the proposed setup will be usable in a real application by giving a detectable signal at the CCD-chip.

The variations of the system parameters give indications of their influences. Additionally, they serve as a feedback for the correctness of the model and the spreadsheet. The basic equations implicitly already give all the effects of parameter variations. The figures make the comparisons easier and show the order of magnitude of the changes in the resulting signal. They give indicators of how to change the signal strength and the " efficiency " of a variation. This can be used in a purely technical sense to estimate the effectiveness of a system modification. On the other hand, cost to benefit comparisons can be done to indicate areas giving better value or higher efficiency for a certain cost.

In a real system the results will surely be somewhat different from the absolute numerical numbers calculated with this modeling. This is due to simplifications and assumptions set up for the basic model as well as imperfections and uncertainties in the behavior of real components. The basic reaction of the system to changes will stay the same, even adjusting for above factors. In a case where this can not be observed, an indicator is given

for a deeper evaluation. This way, a fault in the system or a revision and refinement of the model may be discovered.

6.1.2 Minimum Signal

A fundamental question for the function of the whole system is the size of the difference in the signal at the CCD-chip, ΔN_e. This has to be large enough so that it can be detected and displayed on the monitor as a difference in the grey-levels. In the figures for the model, it can be seen that the two lines representing the case with and without hydrogen are sometimes quite close together. In figure 33, which represents the Princeton Instruments system, ΔN_e at the inside wall is about $1\ ^e/_{pixel\ s}$. The criteria for the detectability is that the variation in the grey level of the image caused by hydrogen in the object has to be larger than the irregularities in the grey level due to noise. Statistical noise and readout noise are the two criteria for this evaluation. The relationship can be formulated in the following way:

$$\Delta N_e\ (t) > \sqrt{\{\ N_{e(H)}\,t + N_r^2\ \}} \qquad\qquad (6.1)$$

$N_{e(H)}$: Signal at output of CCD-chip corresponding to case with hydrogen.

ΔN_e (t) is the difference of the signal N_e (t) without hydrogen minus the signal $N_{e(H)}$ (t) with hydrogen. This can be developed for the exposure time t and gives the minimum exposure time needed for the differential signal ΔN_e (t) to be detectable.
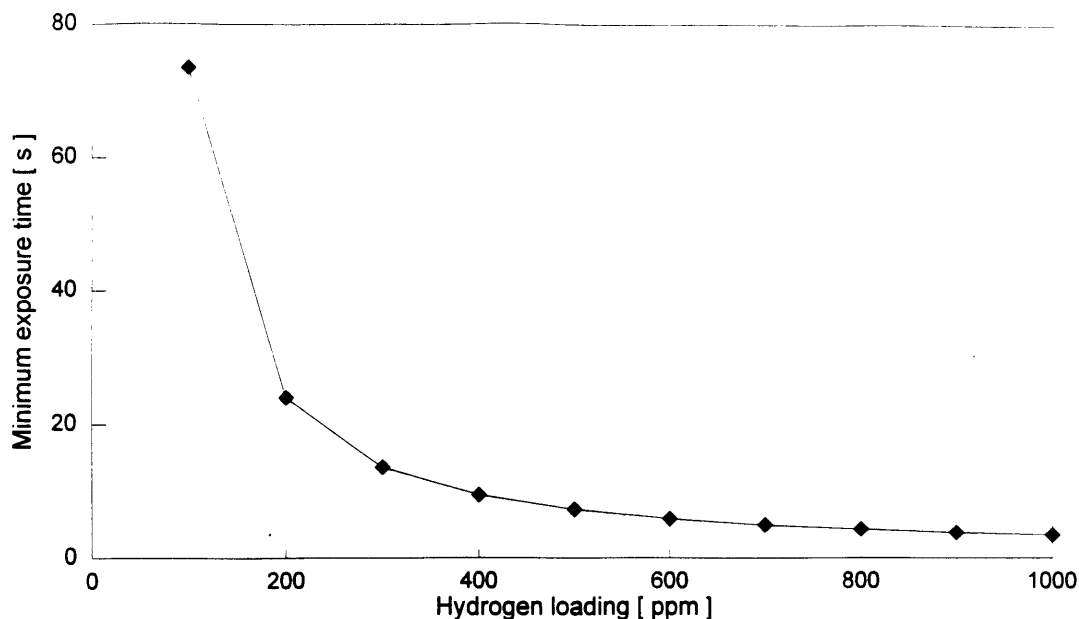
Figure 39. Minimum exposure time t vs. hydrogen loading. Data for PI-system, distance x = 1 cm,

i.e. at inside wall of pipe.

This calculation can be done for various positions in the pipe wall containing hydrogen. However, with an assumption of a uniform distribution of hydrogen in the pipe wall to a certain depth, ΔN_e (t) will go to zero at the position x = r2 - r1. Obviously, this would result in an infinite exposure time necessary to detect this difference. In a practical sense, this would mean that, given the above assumptions, hydrogen can only be detected up to a certain depth into the pipe wall. At a certain point, the amount of hydrogen in ppm will be too small for detection.

Furthermore, as mentioned above, the real numerical value of N_e will seldom be known. In spite of this, a number of interest is the minimum detectable amount of hydrogen. This can be expressed as a difference in the mass attenuation coefficient, $\Delta\mu$. This can be called " Contrast Resolution " and will be discussed in chapter 6.2.3.

6.1.3 Model of the Princeton Instruments System

This model is a variation of the base case adjusted to the anticipated characteristics of the Princeton Instruments ST-138 system with the EEV 1142 x 1252 chip. As mentioned

91

above, it gives an impression of the signal to be expected, although the absolute numerical value will be different for the real system. The figures comparing the general noise levels and the SNR (Figure 31 to 34) give order of magnitude for the initial exposure times so that the signal can be detected. The influence of MPP-mode dark noise reduction on the overall noise is shown, it can be seen that this operating mode can be turned off without a large negative influence on the SNR if the full dynamic range is needed. Furthermore, comparing with the figures on the influence of the chip size in the base case (Figures 23 and 24), the signal could be enhanced by artificially reducing the size of the EEV chip. This can be done by creating a sub-array of the chip which then is sampled in one frame readout.

The influence of pixel size is shown in figures 25 and 26. Judging by these graphs, a reduction in pixel size would seem appropriate to increase the strength of the signal at the output of the CCD-chip. Under this viewpoint, it might seem inappropriate to chose a CCD-chip like the EEV which has relatively large pixels (22 μm x 22 μm). Figures 28 and 29 are somewhat misleading in that the size of the CCD changes with the pixel size (CCD-size = # of pixels x pixel-size). On the other hand, if the CCD-size is kept constant, larger pixels have the effect of increasing the signal per pixel. This can be explained by imagining that the available light on the CCD is distributed over less pixels, respectively one larger pixel can gather more light.

6.2 Relationship between the Model and Real Experiments

6.2.1 Influence of the Assumptions

In the preceding subchapter it was mentioned that the absolute numerical value can be expected to differ between the one calculated for the model and the number for the practical experiment. The importance of this is secondary for two reasons:

1. The result of the practical experiments is not displayed as " Electrons at CCD per pixel per second " but as an image of different grey-levels on a monitor.

92

2. The numerical value has not to be known as the image characteristics (Difference in grey-shade and spatial distribution) are the relevant factors.

Therefore, as long as all the errors introduced by the assumptions do not add up in the same direction and reduce the signal at the CCD to an extent where detection might be impossible, these errors can be treated in a qualitative manner.

- Source flux: This is assumed to be incident on the object. In a real setup, the name "source flux" will be used for the flux of the reactor or at the neutron producing target. This value has therefore to be adjusted for the effects of collimation and the recalculated value introduced into the equations.

- Uniform material properties: This assumption is not to far removed from reality as uniform material properties are present on a macroscopic scale in reality. An exception is a case where the density changes due to planned differences in the material characteristics. This would have to be incorporated into the basic model by making more regions accounting for variable properties. The influence of a small change in density has been shown in chapter 4.5.

- Faults in scintillator screen and CCD-chip: It is to be expected that these are represented in the final image by sharply defined areas with considerably different image qualities. A faulty pixel for example would result in a small square of blackness on the image. As the object can be moved in relation to the imaging system, these errors can be compensated.

- Mirror efficiency: The optical efficiency was assumed to be 1 in equation 3.26. A real mirror will add some distortion and loss of light. The latter can be included in the model by a mirror efficiency factor, ε_m. Distortion will be minimal as most mirrors used for scientific applications have very small tolerances for parallelism and planarity.

- Mass attenuation coefficient of basic iron used for steel: This factor can be more precisely calculated when the exact constituents and alloying elements of the steel

93

are known. Some typical alloying elements have higher attenuation coefficients than Fe, others have lower ones. On an average, it can be expected that the effects will cancel out.

6.2.2 Influence of the Hydrogen Distribution.

The distribution of hydrogen in the steel wall of the pipe will not be uniform to a certain defined depth as used for the assumptions. There is a superposition of various mechanisms influencing the distribution on a macroscopic and a microscopic scale. Appendix A.4 and A.5 give examples of mechanisms influencing macroscopic distribution. For example, permeation of hydrogen depends on solubility, which is a function proportional to the square root of the pressure. Therefore, a parabolic distribution might be expected inside the pipe wall. This would influence the depth to which hydrogen can be detected considerably, as the " Cut off "point for the signal to be larger than the noise would be moved in location closer to the inside of the pipe wall. Appendix A.5 and A.6 supply some mechanisms for the microscopic distribution of hydrogen. Higher concentrations can be expected at faults in the crystallographic structure, grain boundaries and crack surfaces. If these local concentrations are large enough to be detected, they can give additional information about faults in the structure of the component.

6.2.3 Resolution Limits

Spatial Resolution: Spatial resolution is the smallest distance two points on the object plane can have to be still displayed as two individual picture points in the image. This can be limited by a number of factors:

- Resolution of scintillator screen. This depends on the size of the " Scintillator cells " given by the spacing and fineness of the scintillator wires.

- Optical quality of the mirror and lens. A poor quality mirror or lens can cause a distorted, "unfocused" picture in the image plane.

94

- Pixel size of the CCD-chip. The resolution of the proposed imaging system will most likely be limited by this factor, as the object is reduced in size onto this image plane. With a "perfect" mirror and lens, the minimum resolution is given by pixel size and minification m.

$$D_{min} = m\, L_{pixel} \qquad\qquad (6.2)$$

D_{min} : Minimum distance of two points in object plane [μm]; L_{pixel} : Pixel size [μm]. This is for two points that are parallel to the direction in which L_{pixel} is measured. The worst case is given by two points which are parallel to the diagonal of the square pixel. For this, D_{min} is given by:

$$D_{min} = m\, \sqrt{2}\, L_{pixel} \qquad\qquad (6.3)$$

With the numerical values for the EEV CCD of the PI system, this gives a worst case resolution of 113 μm.

Contrast resolution: A second resolution of interest is the difference in the attenuation coefficient $\Delta\mu$ which has been mentioned in sub-chapter 6.1.2. This can be written as a fractional difference $d\mu / \mu$ which then can be expressed as a percentage of the original value of μ which can be detected.

A method to find this contrast resolution is shown in [9]. It is shown, that the fractional difference in attenuation $d\mu/\mu$ can only be detected if the variation in the number of

---

[9] McFarland E.W., Lanza R.C., and Poulos G.W. Multi-Dimensional Neutron-Computed Tomography Using Cooled Charge-Coupled Devices. IEEE Transactions on Nuclear Science. April 1991, Vol. 38, Number 2

neutrons exiting from an absorbing medium caused by the difference $d\mu$ is larger than the detector statistical error.

$$\sqrt{N} < (\, ^{d\mu}/_{\mu}) \, \Delta x \, \mu \, N_d \qquad (6.4)$$

N: "Detector statistical error", Δx: Length of a cubic voxel ΔV in which $^{d\mu}/_{\mu}$ is detected. In the case of the neutron radiography system described here, the " Detector statistical error " is the noise of the neutrons detected at the scintillator screen.

$$\sqrt{N_d + N_d / N_c} < (\, ^{d\mu}/_{\mu}) \, \Delta x \, \mu \, N_d \qquad (6.5)$$

This relation can then be developed for $^{d\mu}/_{\mu}$, giving the following expression:

$$(\, ^{d\mu}/_{\mu}) > \sqrt{ \{ (N_c + 1) / (N_c \, \Delta x^2 \, \mu^2 \, \rho^2 N_d) \} } \qquad (6.6)$$

N_c is given by equation 3.33; N_d is given by equation 3.23 and N_i in this expression is described for a pipe in equation 3.22. These expressions can be inserted into relation 6.6, together with the numerical values for the system components the minimum fractional difference in the mass attenuation coefficient can be found. For the length Δx it is recommended to use a number close to the spatial resolution calculated above.

96
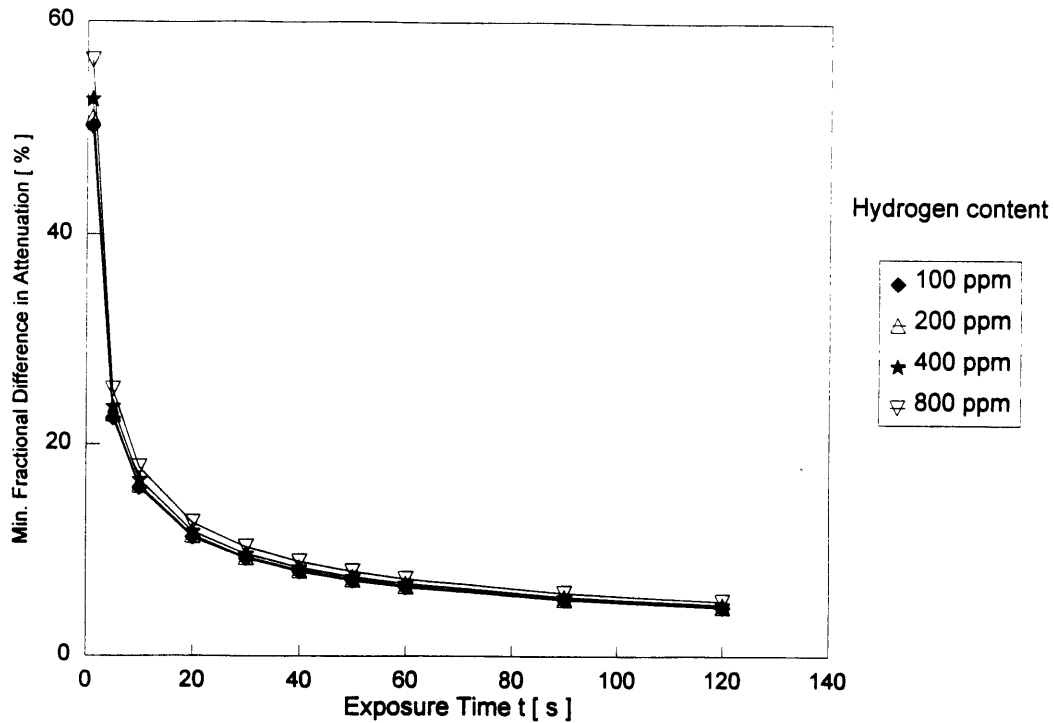
Figure 40. Minimum contrast resolution vs. exposure time t. Data for PI-system, distance x = 1cm, i.e. at inside pipe wall.

6.2.4 Scattering

No scattering has been assumed for the modeling of the system. In general, this is not true as a certain number of neutrons of the beam will be scattered in the object. On the scintillator, two kinds of neutrons could then be considered:

1. Unscattered, unabsorbed primary beam neutrons

2. Multiply scattered neutrons.

The effect of scattering on the imaging process has been described in [10]. Contrast resolution $(d\mu/\mu)$ is reduced by scattering and is described in the following equation:

$$({}^{d\mu}/_\mu)_{scatter} = ({}^{d\mu}/_\mu)_{no\ scatter} \times g_s \qquad\qquad (6.7)$$

---

[10] See reference to footnote 8, page 95.

g_S : Square root of the ratio of the total # of neutrons incident on the detector to the # of primary neutrons incident on the detector.

g_S is a function of the material and the thickness of the material. Some examples are listed in table 15.

Table 9. Factor g_S for various materials and thicknesses T. Table copied from reference [8]

Material	T = 2 cm	T = 10 cm	T = 20 cm
Iron	1.9	168.6	1.5×10^7
Aluminum	1.0	1.2	2.3
Water	18	1.9×10^7	1.0×10^{22}
Silicon	1.0	1.5	10.9

In the pipe geometry used for the modeling, the thickness of steel the neutron beam has to travel through is in the order of 10 cm (2 y1 + 2 y2 = 8.72 cm). A approximate interpolation from table 15 gives a factor g_S of around 125, which is a considerable reduction in contrast resolution. This might make the function of the whole system questionable, as very long exposure times would be needed to reach the minimum value for ($d\mu$ / μ)$_{scatter}$. On the other hand, the numbers above represent a worst case scenario. Some methods are available to reduce scattering, such as scattering grids or increasing the distance object to detector.

CHAPTER 7

CONCLUSIONS AND RECOMMENDATIONS

7.1 Conclusions

Steel is one of the most commonly used construction materials. Steel consists of iron with less than 2 % carbon, certain other elements can be added for alloying purposes. The manufacturing process and the type and amount of alloying elements added to the steel determine the properties and characteristics of the final product.

Unprotected steel is susceptible to environmental attack. Corrosion by air and moisture ("Rusting") is the best known form. The resistance of steel to corrosion can be enhanced by adding certain alloying elements, chromium and nickel are the most effective.

An other form of degradation of steel by the environment is hydrogen embrittlement. The mechanical properties of steel are changed by embrittlement, the ability to cope with vibrations and deformations is reduced. Changes in the geometry of the component that were foreseen for the original design can lead to a failure in a brittle region. An example of such a component is an assemblage of steel pipes transporting a fluid at high pressure and/or temperature. Failure of one section of the pipe can lead to catastrophic results.

A survey of the information available from materials science shows the mechanisms involved in the adsorption, dissolution and diffusion of hydrogen in steel. The crystallographic structure, environment and the alloying elements have a strong influence on the amount of hydrogen to be expected in a steel part. Concentrations of hydrogen or hydrogen-compounds in certain locations in the structure of the base metal lead to embrittlement by inhibiting the movement of dislocations. It is to be concluded that if the

basic chemical-physical processes can not definitely be excluded, a certain amount of hydrogen has to be expected in the steel.

Hydrogen embrittlement is not as easily detectable as surface corrosion. Therefore, methods are sought to reveal the amount of hydrogen enclosed within the walls of a part. One proposed method is non-destructive testing by neutron radiography. Due to the much larger nuclear cross-section of hydrogen compared to steel for thermal and sub-thermal neutrons, relatively small amounts of hydrogen might be detected within a structure. Based on earlier experiments, a system for non-destructive testing of steel pipes is proposed. The system is based on a thermal (or cold) neutron source, a scintillator screen and a cooled CCD-camera imaging system. Before a real system is set up for experiments, the suitability to the task is evaluated theoretically. For this purpose, the system and components are modeled, resulting in a set of equations. These equations are used in a computer to imitate the responses to various input parameters. The initial results are positive, the output signal at the CCD-chip in the camera head is large enough for further amplification and manipulation. The responses to parameter variations are as expected and give a first validation of the model.

In a second step, a more refined look is taken at the system. Parameters representing real components are introduced and the effects of statistical, readout and dark noise on the final output signal are studied. The influence of simplifications and errors on the result are discussed. This second step shows some limitations, small amounts of hydrogen will be very difficult, for practical purposes even impossible to detect. The pipe geometry also influences the usefulness of the system considerably. Large pipes with thick walls attenuate the primary neutron beam down to a level where single electrons have to be detected and evaluated. Even though the noise background on modern CCD-cameras is extremely low, tracking an absolute signal consisting of single electrons is close to

100

impossible. Outside of these limiting regions, the system fulfills the basic function of detecting hydrogen.

In a final step, the spatial and contrast resolution are assessed. Additionally, scattering effects are introduced. Multiple scattering reduces the contrast resolution for the basic model by a factor of approximately 125. Although this is a worst case scenario and improvements can be introduced, this may set serious limitations and render the system unusable for some applications.

The model of the neutron radiography system and the evaluation so far has shown that it is basically possible to detect hydrogen in the wall of a steel pipe. The fundamental remaining question is: " How much hydrogen causes dangerous embrittlement of the pipe and leads to a failure? ". This is a very important question, as the answer sets the limits for the affected component as well as for the testing system. It is very difficult to give a definitive answer, as a multitude of factors influence the outcome. Furthermore, it has been concluded earlier that a certain small amount of hydrogen can be anticipated in all steel components, without necessarily endangering them. Some of the factors that have to be taken into consideration are:

- The type of steel, the microstructure and the alloying elements
- The stresses and strains on the component, their distribution over time (e.g. vibrations)
- The pressure, temperature, type and consistence of the transported fluid
- Other factors of the operating environment
- The processes involved in the initial construction (e.g. welding, hardening, annealing)
- The operating and maintenance routine.

Under these circumstances, with all the involved variables, it will never be possible to give one specific answer. The information from practical experiments and operating experience will have to be combined with knowledge of materials science to give ranges

for limiting hydrogen contents. Each case has to be analyzed carefully and the above factors included with the results.

The model utilized for the assessment of the a neutron radiography system represents a laboratory setup. The type of source is undefined, but assumed to be stationary (immovable). The object has to be moved in three dimensions for inspection. For usage in industrial facilities, the roles will have to be reversed. The object, i.e. a pipe, has to stay in position and the source and imaging system have to be moved around and along the pipe. Judging by the complexity and very limited space around pipes in a power plant or refinery, such movement may not be possible.

Taking into account these practical considerations and the limitations imposed by object size and contrast resolution on the imaging quality, the author feels that with the proposed technology, there could be a very limited use for such a system in non-destructive testing of fixed steel pipes in a power plant. Substantial improvements have to be implemented on a practical system to justify the costs involved with the development and production. Improvements can be made in two areas:

a. Detection/resolution quality of the imaging system with scattering effects

b. "Suitability" of the whole system to the practical environment.

The improvements in a.) can be implemented relatively easily by modifying components in the system. In chapter 4, several methods have been shown that increase the absolute signal level and the differential signal, e.g. an optimized object to CCD geometry, high quality lenses, a suitable scintillator screen and scattering grids. Although the costs of some of these improvements may seem high initially, they have a lasting and constant overall positive effect. An other region to improve on the initial system is the use of a cold neutron source. Cold neutrons give substantial changes in opposing directions in the attenuation coefficients of steel and hydrogen (e.g. μ_{Fe} from 0.15 to 0.075, μ_H from 22 to 44 cm^2 /$_g$). This would result in less attenuation of the principle neutrons in the steel

102

and a larger differential signal ΔN_e (See also chapter 7.2). Cold neutrons can for example be produced with the appropriate cooled targets by a linear accelerator. The initial costs for setting up such a target are rapidly offset by the large gains in imaging capability.

Improvements in b.) are considerably more difficult to reach. A critical factor is the ratio of power (flux) to size (physical volume) of the source. Accelerator based sources that produce a flux in the region of $10^7 \, n / cm^2 \, s$ are bulky and easily fill a small room (~ 100 m^3). A much more compact source would be naturally radioactive elements. A source that produces around $10^7 \, n / cm^2 \, s$ can have a volume of about 1 liter ($10^{-3} \, m^3$). The disadvantages are that it is a "nuclear" source that can not be turned of at will and that the neutrons are emitted isotropically with a relatively broad range of energies. Considerable development will have to take place in this region to produce a suitable source. This development work should be left to other research- or industrial laboratories, so the costs do not have to be carried by M.I.T. The disadvantage of this is that only a small amount of influence on the direction of the research can be taken directly.

Even if the demands imposed by b.) can not be met in the immediate future, a neutron radiography/tomography system still remains an excellent tool for NDT. Although the utilization of this method as a testing equipment for stationary pipes in a power plant does not look promising at the moment, this has to be seen in relation to the many other uses of neutron radiography. A system with good imaging qualities like the one described in the previous chapters has a multitude of applications in NDT, some examples have been given in chapter 2.1 and 2.2.

Other methods are available for the testing of materials for defects or, in this case hydrogen content. Most of the methods have the disadvantage that they are either destructive or at least require the dismantlement of a component (e.g. chemical extraction, SEM). For non-destructive testing, radiography methods have to be chosen.

An alternative to neutrons would be the use of X-rays. The disadvantages of these systems are that they rely on density changes and have a much smaller dynamic range. These disadvantages could surely be somewhat alleviated with further development and investments. On the other hand, it is to be assumed that the costs would be no smaller than to implement comparable changes on a neutron radiography system.

7.2 Recommendations

The model has shown that the proposed imaging assemblage based on a cooled CCD-camera can work. Limitations have been discovered and the influence on the effectiveness discussed. Some of the limitations can be reduced with the use of cold neutrons, as these give another substantial increase in the difference of the attenuation coefficients. (μ_{Fe} is reduced by a factor of 2 which results in e^2 (= 7.4) times less attenuation by the same amount of steel.)

Similar to any model, the real system can not be described entirely and represented 100 % accurately. Although care is taken not to change any of the basic characteristics and functions by the modeling process, some unknown effects might remain. Therefore, the model represents a good tool for a preliminary assessment and a quick variation of parameters.

Although it was concluded that the proposed present state of technology has serious limitations, an experimental facility must be set up and operated. The short, preliminary tests described in chapter 5 have shown how much invaluable experience and knowledge can be gained by practical experimenting. Furthermore, feedback from the experiments can be used to develop and refine the model, making it into a powerful supplementary tool for testing.

Various components that are already available for an experimental facility have been mentioned in earlier chapters, further parts will follow within the next few months. A linear accelerator is going to be delivered from AccSys Technology, Inc., Pleasanton, CA

({510}462-6949) and set up in a basement room of the M.I.T. Nuclear Reactor Laboratory buildings. Together with appropriate targets, this can be the source for a whole line of neutron radiography experiments.

For a continuation on the detection of hydrogen embrittlement in steel pipes, the following steps are proposed:

1. Test the CCD-camera system with optical experiments after delivery. Check the function of all components in all modes. Familiarize operators with system and software.

2. Build up a neutron radiography test facility. Allow enough space in the object area for various object geometries and types, implement remote object handling. Set up aluminum box with the scintillator screen, mirror and camera. Test the whole setup with optical experiments to check for correct function of object handling, mirror placement and camera alignment.

3. Run simple neutron radiography experiment with some specially prepared test objects, e.g. steel blocks with water channels or steel blocks through which hydrogen gas can be passed. Calibrate the system with these test objects. (Geometry of object is well defined and "hydrogen content" is known.)

4. Extend tests to simple pipe geometry without hydrogen. Does the experimental data correspond to the model results? If not, analyze the cause for the discrepancy and re-evaluate the model.

5. Repeat above test with the same pipe with the inside wall loaded with hydrogen. The type of steel used should initially be chosen to allow hydrogen ingression by pressurizing the inside of the pipe with a hydrogen gas.

6. Extend object geometries to other forms and components to find the limits of the system in the function as a non-destructive test facility.

Parallel to this line of tests, other neutron radiography or tomography experiments can be run. After some time, a large amount of knowledge and practical experience will have been acquired, which can be put to excellent use to further enhance the possibilities of neutron radiography.

APPENDIX A

METALURGICAL CONSIDERATIONS

A.1 Characteristics of Some Metallic Construction Materials

A.1.1 Aluminum

Due to its light weight in comparison to steel, aluminum has evolved into the prime construction material where weight is of importance, like the aerospace industry. Additionally, it is more resistant to surface corrosion in a normal outdoor environment than most iron-based materials. Surface treatments with corrosion inhibiting layers of paint can be omitted, further saving weight. The negative aspects of aluminum include higher costs for the basic material and tooling (e.g. specialized welding procedures) and lower strength than iron-based alloys. Furthermore, fatigue life is limited on most aluminum-alloys.

A.1.2 Titanium

A combination of high strength and good high temperature stability with low weight has made this material quite popular for highly stressed components in light weight structures. Titanium also displays a good resistance to corrosion. High price and specialized tooling have prevented widespread use and limited applications to areas where the positive characteristics are really needed, e.g. turbine blades on jet engines, main wing spar to fuselage connections on military aircraft, specialist light-weight bicycle frames. Pure titanium components are quite brittle, alloying elements e.g. vanadium, can somewhat alleviate this characteristic.

A.1.3 Iron and Steel

The most widespread metallic construction material in use. Pure Iron (Fe) by itself is rarely used as a construction material. It is highly ductile at room temperature and strongly magnetic, difficult to obtain and expensive. "Iron" as a material in the metallurgical sense has a content of less than 0.04 to 0.05 % carbon. Cast Iron has a carbon content in excess of 2 % and usually less than 4.5 % C. Steel, which is basically an alloy of iron and not over 2 % of carbon, is further subdivided into various classes of steels with a wide range of physical characteristics and mechanical properties. Precisely controlled amounts of alloying elements and carbon are responsible for these properties as well as closely controlled manufacturing processes.

a.) Atomic Structure

Like all other metals, iron is crystalline in structure. Crystalline bodies are thought of as composed of atoms placed at points in a space lattice. The smallest component of this lattice is a unit cell, characterized by a regularity in the structure.

Iron exists in one of two forms of a space lattice, where the unit cell is formed by cubes. The two lattice types are known as body-centered cubic (bcc) and face-centered cubic (fcc). The bcc form has an atom at each corner and one in the center of the cell. The fcc form again has an atom at each corner but also one in the center of each of the six faces. The lattice types are a function of temperature and carbon content. As an example, the changes in type of lattice for "Iron" (carbon < 0.04 %) are given:

Table 10. Lattice types as a function of temperature

Temperature [C]	Lattice Type	Name
Room Temp. (20)		
to	bcc	α-ferrite, magnetic
770		
to	bcc	α-ferrite, non-magn.
910		
to	fcc	γ-iron, non-magn.
1410		
to	bcc	δ-iron
1540 (melting pt.)		
above	no known changes	

The addition of carbon changes the temperatures and properties. These phase changes have been extensively studied and are described in the equilibrium phase stage diagram for Fe - Fe3C.
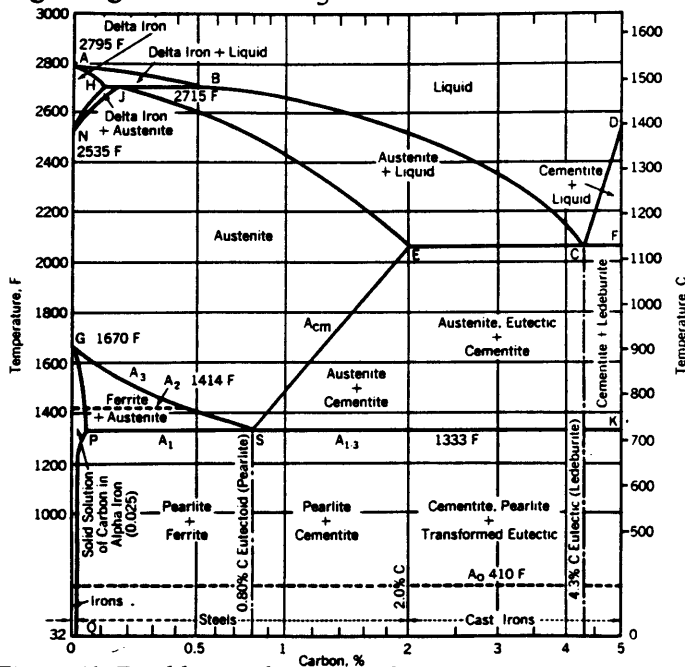
Figure 41. Equilibrium phase stage diagram for Iron and Carbon

b.) Effects of Alloying Elements

The primary alloying element for iron is carbon, which, together with other elements like manganese, silicon, sulfur and phosphorus, turns it into steel. Steel itself can then be alloyed with other elements to further influence the physical characteristics and mechanical properties. In the following, some effects of alloying elements are discussed.

Carbon: Even though carbon is not generally regarded as an "alloying" element for steel, because steel without carbon would not be steel, it is appropriate to mention it. The general influence of an increase in carbon content is a higher ultimate strength and hardness but lower ductility and thermal and electrical conductivity. Carbon content is usually restricted to 0.15 % in low-alloy steel for high-temperature applications, this ensures optimum ductility for welding and bending operations. An other consideration limiting carbon content is the susceptibility to intergranular stress corrosion cracking for chromium-alloyed steels. The upper limit here is 0.08 %, although 0.03 % carbon can be used in extremely low-carbon grades.

Chromium: This is one of the essential constituents of stainless steel. It raises the yield and ultimate strength as well as hardness and toughness at room temperature. At high temperatures, these effects are much less noticeable. A steady improvement in the resistance to atmospheric corrosion is seen when the chromium content of steel is increased above 12 %. Chemical properties are however effected by carbon content. Generally, the higher the Cr-content and the lower the C-content, the more an alloy will be able to resist corrosion. The upper limit for the addition of Cr is at 30 %. Above this content, the resulting steel is very brittle and has no practical value as construction material.

Nickel: The principal benefit obtained by the addition of Ni (over 1 %) is increased toughness. It dissolves in the iron matrix in all proportions and therefore raises the ultimate strength without impairing ductility.

The most important use of nickel is addition of more than 8 % in combination with chromium. Various combinations of these two elements produce alloys known as " 18/8-types " which cannot be obtained with equivalent amounts of any of the elements alone. These types of steel display enhanced resistance to corrosion at high temperatures as well as higher creep strength.

Molybdenum: This element increases the strength, resistance to wear, elastic limits and hardenability of steel. It also enhances the inherent corrosion resistance in stainless steels of the above mentioned " 18/8-types " by reducing chemical media.

Tungsten: Similar in behavior to Mo, although the molybdenum is more effective in increasing strength from a cost/benefit viewpoint. Tungsten is important for tools for high speed cutting.

Vanadium: It mainly increases strength, toughness and hardness in a steel by forming carbides which stabilize the structure especially at high temperatures. Va also intensifies the individual properties of other alloying elements.

Phosphorus: It is effective in increasing the machinability of free-cutting steels. This is caused by an embrittling effect by which phosphorus increases the grain size and causes segregation. When machining considerations are of lesser importance, this embrittling effect is less desirable. Also, the presence of phosphorus is objectionable to welding. It is therefore mainly used in proprietary low-alloy high-strength steels where increased yield strength and resistance to atmospheric corrosion are primary requirements.

Silicon: The effect of this element is felt in two phases of the life of steel. During production it deoxidizes and degassifies, in the finished component it increases ultimate strength without loss in ductility as well as resistance to corrosion. Addition of more than 2.5 % causes brittleness, more than 5 % makes the steel non-malleable. Silicon also decreases the electrical conductivity of steel and hysteresis losses. Therefore it is often used in electrical apparatus.

Manganese: This is an excellent deoxidizer and sulfur neutralizer and improves the ratio of yield strength to tensile strength at normal temperatures. It also prevents a certain form of brittleness, known as " Hot Shortness ". On the negative side, it increases the crack sensitivity of welds, especially with high-carbon steels.

A.2 Mechanical Properties of Steel

Steel is the basic material in use for pressure parts in nuclear steam supply systems. Various types of steel are used, each with different properties especially suited to specific tasks. These steels must have characteristics which make them suitable for manufacture as well as long service life under often harsh operating conditions. Guaranteed consistency of a type of steel with specified properties must be checked by testing methods in compliance with standards by the ASTM (American Society of Testing and Materials) and other authorities.

The principle method of testing for strength is the tensile test, where gradually applied unidirectional pull determines the maximum nominal load that a material can withstand before actually breaking. This test also records the relationship between stress and strain. Up to a certain point (A), a release of the stress will result in a return of the object to the original dimensions (Elastic deformation region). If the stress is continued over this point, permanent deformation of the object will occur up to the breaking point (Plastic deformation region). The true point of transition between these two regions is difficult to determine with accuracy and is thus called "yield strength" (YS).

TS

YS

Stress

A

O
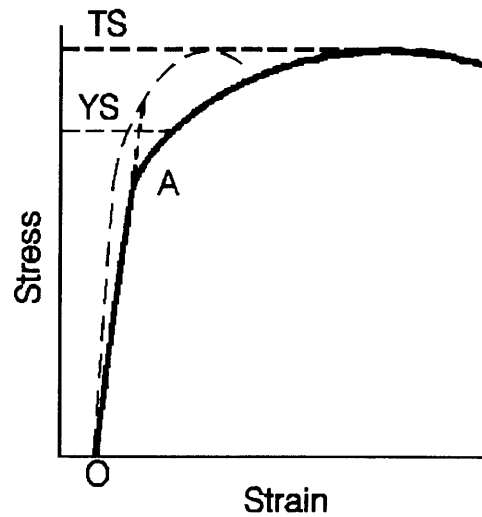
Strain

Figure 42. Generic Stress vs. Strain Diagram

Embrittlement of a material changes the stress to strain relationship:

    a.) Steepening of the line OA, i.e. less strain for the same amount of stress. (Or, vice versa, more stress for a given amount of strain.)

    b.) Steepening of the curve A to TS

    c.) Shortening of the curve A to TS.

These effects are demonstrated by the dotted line in Fig. 2. The area under the dotted curve is smaller, the possible deformation work has been reduced.

Embrittlement of a component can thus lead to a lack of ability to withstand stresses and/or strains imposed on it by the initial use in a system. If a certain elongation (strain) in the elastic region was foreseen in the original design, this same strain may lead to stresses that bring about plastic deformation or breaking in the brittle material.

Embrittlement of a material therefore sets serious limitations on the function foreseen by the original design, it may no longer be able to fulfill the basic functions.

A.3 Uses of Certain Types of Steel

A.3.1 Tube Steels

Seamless or electric-resistance welded tubes for uses in boilers and other heaters are often made out of hot-rolled low-carbon steels.

An other type of steel used for boiler tubes is medium-carbon steel with a maximum of 0.35 % C. This grade of steel permits higher stress levels than low-carbon steel in the 280 - 360 ° C saturation temperature region usually encountered.

Higher temperatures in pressure parts can occur in the superheater and reheater in fossil-fuel power plants. These tubes have to be made out of materials displaying superior high-temperature properties and resistance to oxidation. Carbon steel is suitable and economical up to about 450 - 500 °C, depending on pressure. Above this, alloy steels are required. Carbon-molybdenum steels are used in the intermediate temperature range, so called low and intermediate chromium-alloy steels are used in the higher temperature regions. Stainless steel is used in the hottest regions of modern high-temperature boilers (560 °C, 12 - 28 MPa).

These are operating regions which apply to fossil-fueled power plants in the boilers. The situation in a nuclear power plant is different in as much as there is no exposure to high temperature gases (combustion gases) and the highest temperatures in a light water reactor system are 320 - 350 °C. On the other hand, there is an additional environmental component for nuclear steam and water piping, in the form of radiation.

A.3.2 Nuclear Steam Supply Systems

In the primary loop of a pressurized water reactor, mainly stainless steel is used. The pressure vessel and thick pipes are generally made of low-alloy steel with stainless steel cladding or lining. A special case for pipes in the primary system is the fuel cladding,

where Zircalloy, alloys of zirconium is used. Zircalloy displays low neutron absorption with adequate strength and resistance to corrosion in the reactor coolant environment. For the steam generator tubes of a PWR, Inconel is employed in place of 18/8 stainless steels, as the latter showed some corrosion on the steam side. Commercial Inconel alloy 600 tubing has a high resistance to corrosion on both sides of the system and has a lower coefficient of thermal expansion, resulting in lower stresses in the steam generator tubing. Inconel 600 is also used for other parts in the nuclear system, e.g. for control rod drive housings on PWR vessel heads. Recently, some problems with cracking of this material in the region of the connection of the drive housing to the vessel head has been discovered and is under investigation.

Table 11. Composition of Inconel 600. Limiting chemical composition in % .

Nickel (+ Cobalt)	> 72	Carbon	< 0.15
Chromium	14 - 17	Copper	< 0.5
Iron	6 - 10	Silicon	< 0.5
Manganese	< 1	Sulfur	< 0.015

A.3.3 Primary Coolant Piping

The stainless steels most common in reactor systems are the AISI (American Iron and Steel Institute) 300 series. These are austenitic stainless steels that display similar qualities in strength, ductility and resistance to corrosion at high temperatures. The main types in use for the primary system piping are 304 and 316. 304L, 316L and 347 are used in smaller quantities, although a recent move towards the "L"-types has taken place, as these are more resistant to stress corrosion cracking in BWR. The letter "L" stands for low-carbon content.

Table 12. Composition of 300-Series Stainless Steels (in wt%)

Type	Fe	Cr	Ni	Mn	Mo	Si	C	S	P
304	Balance	18-20	8-10.5	-	2	1	0.08	0.03	0.045
304L	Balance	18-20	8-12	-	2	1	0.03	0.03	0.045
316	Balance	16-18	10-14	2-3	2	1	0.08	0.03	0.045
316L	Balance	16-18	10-14	2-3	2	1	0.03	0.03	0.045
347	Balance	17-19	9-13	-	2	1	0.08	0.03	0.045

A.3.4 Steam Piping

The steam piping system has to be correctly designed and erected to accommodate for thermal expansion and absorb vibrations. These operational characteristics also set certain criteria on the material. Joints are commonly welded, giving another aspect to the selection of the appropriate type of steel.

In early applications of carbon-steel pipes in fossil plants a tendency towards graphitization in the region of the welds at temperatures above 420 °C was noticed. Consequently, carbon-molybdenum steel was used in higher temperature applications, but the same effect was noticed in the long term use.

This brought about a change to chromium- molybdenum steels for steam pipes. They usually have 2.25 % Cr + 1 % Mo or 3 % Cr + 0.9 % Mo and display good high-temperature and corrosion stability.

A.4 Hydrogen in Metal

A.4.1 Hydrogen-Metal Relationship

The nature of the interaction depends principally on the chemical characteristics of the metal. Alkali and alkaline earth metals form hydrides, group IVB, VB, VIB form co-valent hydrides, group IIB, IIIB do not react with hydrogen in any way. Metals of group

IB, VIA, VIIA and VIII absorb hydrogen endothermically to form very dilute solid-solutions. These are called "endothermic occluders". Metals of group IIIA (except B and Al), IVA and VA absorb hydrogen exothermically to form "pseudo metallic" hydrides, called "exothermic occluders".

Iron belongs to the class of endothermic occluders. Manganese, probably chromium and possibly molybdenum are anomalous in belonging to both classes.

The nature of interstitial solutions of hydrogen in metals: Small atoms of non-metallic elements - hydrogen, boron, carbon, nitrogen and oxygen - can occupy octahedral or tetrahedral interstices in metal crystals. This introduction of a foreign atom into an interstice of a metal crystal involves a local strain and, usually, the metal becomes hard and brittle. The relation of the size of the interstice to the size of the atom plays an important role in the "solubility" of the element. But this is not the only effect, in the case of hydrogen, the electron interaction energy seems to play a main part in the phenomena of "solubility".

Most metals of the "C"-class [11], with the exclusion of gold and tungsten, not only adsorb hydrogen on their surfaces, but also show bulk occlusion. Hydrogen present in the bulk of a "C" metal may be combined, interstitially dissolved and rift occluded. It may occur in atomic, molecular and partially ionized forms, and each of these forms can undoubtedly influence the physical properties of the given metal in different ways. A particularly important material which exhibits this property are the Ti-V alloys used in jet engines.

A.4.2 Solubility

The solubility of hydrogen in pure iron is extremely low. Solubility undergoes a sudden increase on passing from alpha-phase to gamma-phase (approximately 900°C). A further

---

[11]Class "C" metals include Ti, V, Cr, Mn, Fe, Ni, Cu, Zr, Mo, Ag, Pt, Au, Pa, U and more.

sudden increase is seen upon melting. The significance of this for the end product is that comparatively large quantities may be absorbed during fabrication at high temperature, resulting in super-saturated steel at low temp. (Remedy: very slow cooling rates.) Furthermore, solubility is proportional to square root of the pressure.

Table 13. Solubility of Hydrogen in pure Iron at p = 1 atm

Temp. [°C]	cm^3 / 100 g	ppm by weight	atomic %
400	0.35	0.32	0.002
600	1.20	1.08	0.006
800	2.45	2.21	0.012
1000	5.50	4.95	0.026
1200	7.95	7.16	0.040
1400	11.20	10.08	0.060
1535 solid	13.32	12.00	0.067
1535 liquid	26.64	24.00	0.134

Units in which Hydrogen Content is Measured: Several units are used to measure the amount of dissolved hydrogen in a metal. In the following, the explanations of the units are given and including a conversion table:

Atomic Concentration: c   = atoms H per atom of the metal.

Relative volume: R.V.   = volumes of H_2 per volume of metal.

Weight percent: wt %   = grammes of hydrogen per 100 g metal.

Gas volume per metal weight: B = cubic centimeters of H_2 per 100 g metal.

When using parts per million (ppm): 1 ppm = 0.0001 wt % = 0.0873 R.V. = 1.11 cm³/100 g

Table 14. Conversion Factors for different units of hydrogen content in metal. With: ρ_{Fe} *= 7.88 g/cm³ ; atomic weight of Fe = 55.84*

Given Value ⇒ Computed Value ⇓	c	R.V.	wt %	B
c	1	6.33×10^{-4}	0.553	4.98×10^{-5}
R.V.	1580	1	875	7.88×10^{-2}
wt %	1.81	1.15×10^{-3}	1	8.92×10^{-5}
B	20'000	12.17	11'100	1

Dependence of Solubility on Pressure: This relationship is described by the square root law, generally applicable to endothermic occluders at all except high pressures, and at all temperatures:

$$s = k \times p^{1/2}$$
(A.1)

s: solubility; p: pressure; k: constant, dependent on temperature.

A.4.3 Solubility of Hydrogen in Steel as a Function of Alloying Elements

a.) Carbon. Measurements of the solubility of hydrogen in iron-carbon alloys are complicated by the formation of methane, and hence the few experimental data found in the literature are controversial. One effect is the solubility of hydrogen in molten iron, this diminishes with increasing carbon content.

b.) Manganese. Manganese has little influence on the solubility of hydrogen in ferritic steel. On the other hand, the solubility at 400°, 500° and 600°C in a steel containing 12.98% Mn and having in part an austenitic structure is much greater than in pure iron.

c.) Silicon. Experimental investigations showed that this alloying constituent lowers the solubility of hydrogen in steel.

d.) Aluminum. Little quantitative data exists, a decrease of the solubility has been observed for alloys containing up to 6 % Al.

e.) Chromium. Chromium shows an anomalous behavior, absorbing hydrogen endothermically or exothermically according to temperature. The following phenomena have been noted:

> (i) The solubility of hydrogen in chromium and in alloys of chromium and iron which have a bcc crystal lattice is always less than that in iron at a given temperature and pressure.

> (ii) Alloys containing 5 to 15 % Cr and having at a given temperature a fcc crystal lattice, dissolve more hydrogen than γ-iron.

> (iii) Alloys containing more than 15 % Cr, and thus having a bcc crystal lattice, dissolve less hydrogen than iron.

f.) Nickel. The solubility of hydrogen in nickel is several times greater than in iron. Alloys of iron with nickel dissolve hydrogen in amounts which depend on the percentage of nickel.

Table 15. Solubility of Hydrogen as a Function of Nickel Content

Temp.[°C]	300	500	700	900	1100
Solubility [cm^3 H_2 / 100g]					
Fe	0	0.8	1.8	3	6.7
3.3 % Ni	0	0.9	2	5.3	7.5
5.5 % Ni	0.3	1.0	2.1	5.6	7.7
72.4 % Ni	0.8	1.9	3.8	6	8.4

g.) Molybdenum. The presence of Mo in alloys with iron up to 33.6 at.% Mo has almost no effect on the hydrogen solubility.

h.) Tungsten. Tungsten does not dissolve detectable traces of hydrogen and its presence in steel lowers the occlusive capacity for hydrogen.

i.) Exothermic Absorbers: Vanadium, Titanium, Columbium, Zirconium and Tantalum. All exothermic occluders. when alloyed with iron, cause an increase in the hydrogen solubility: an increase which is particularly pronounced at low and medium temperatures.

j.) Chromium and Nickel.
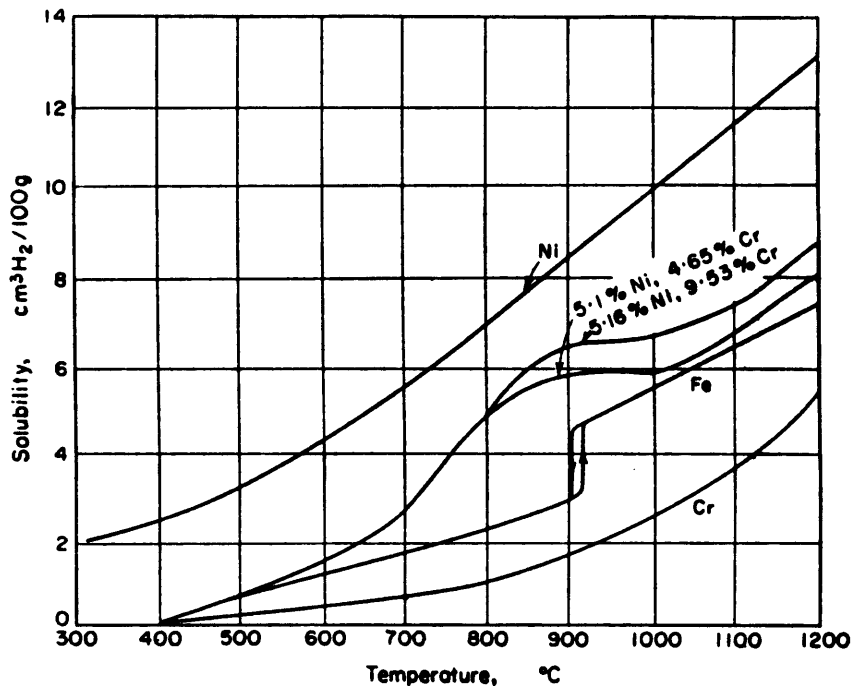
Figure 43. Solubility of Hydrogen as a Function of Chromium and Nickel Content

Influence of the Crystallographic Structure Under given conditions, the solubility of hydrogen is usually greater in metals or alloys having a fcc lattice (γ-iron, nickel, austenitic steels) than in metals or alloys having a bcc lattice (α-iron, δ-iron, chromium, ferritic steels). This has been attributed to the fact that in a model of a face-centered cube formed by spheres there are larger empty spaces than in the body-centered cube.

121

It is assumed that hydrogen occurs in iron and steel in three forms at least:

(a) interstitially dissolved (α-phase);

(b) bound by electrons taken from hydrogen atoms into the d-shell of iron atoms (β-phase);

(c) gas accumulated in blisters, cavities and voids.

Blisters, cavities voids and other "traps" for gaseous hydrogen inside the metal phase are filled with a mixture of molecular and atomic hydrogen under high pressure. The equilibrium conditions inside these traps are greatly altered as compared with the separated gas phase, since chemisorption and physical adsorption evidently occur on the highly active and greatly developed metal surface. Even though the absolute numbers for hydrogen dissolved in steel may seem small (around 10 to 20 ppm), it is misleading to think of this as the maximum amount in a real piece of steel. All three effects mentioned above account for considerably higher numbers, depending on the environment. Research in the area of dissolution of hydrogen in various metals is still ongoing, sometimes contradictory information supplied by different research groups can be encountered.

A.5 Diffusion and Permeation of Hydrogen Through Iron and Steel

A.5.1 Possible Mechanism of Hydrogen Flow through Metals

For a dissociating gas passing through a metallic wall the following processes can occur:

(A) At the ingoing surface

1.Dissociation of gas molecules into atoms.

2.Adsorption of gas atoms on the metal surface.

3.Passing of adsorbed atoms from the surface inside the metal phase, possibly partial or total ionization of gas atoms.

(B) Inside of the metal phase

4.Diffusion of dissolved atoms or ions through the metal phase.

(C) At the outgoing surface

        5.Passing of gas atoms or ions from the metal phase onto its surface.

        6.Desorption of gas from its surface.

        7.Recombination of desorbed gas atoms into molecules.

Theoretically, each of the above partial processes may be rate-determining for the whole phenomenon of gas passage through the wall. Processes (C) 5 to (C) 7 may evidently occur not only on the external surface of the metal but also on the surfaces of internal defects of its structure such as grain boundaries, cavities, impurities, non-metallic inclusions, dislocations, etc.

A.5.2 Application of Fick's Law to the Flow of Hydrogen Through Metal

Fick's second law, for change in concentration:

$$\delta c/\delta t = \delta/\delta x \ D \ (\delta c/\delta x) \qquad\qquad (A.1)$$

where D = Diffusion coefficient [cm^2 / $_s$] and c = concentration [^{g} / $_{cm^3}$].

To evaluate experimental results, the above equation must be integrated with defined boundary conditions. Assuming steady state, the gas quantity M passing through a wall of thickness d and surface A during a time period t will be expressed by:

$$M = DA \ [(c_1 - c_2)/ d \ ] \ t \qquad\qquad (A.2)$$

c_1 and c_2 are concentrations of the gas in the metal phase, just below the entering and outgoing surfaces respectively.

If A = 1 cm^2; d = 1 cm; t = 1 sec and c is expressed in cm^3 gas per cm^3 metal, then M is in cm^3 gas passing per sec through 1 cm^3 of the metal. Then we have:

$$M = D (c_1 - c_2) = P_a \qquad\qquad (A.3)$$

The value P_a is commonly called permeation rate or permeability. Since (c_1 - c_2) is proportional to the solubility of the gas in the given metal, the above formula indicates that the permeability P is a function of solubility [12]

A.5.3 Various Parameters that Effect Hydrogen Flow

Various parameters effect the flow respectively diffusion of hydrogen through a metallic phase:

-Thickness of the wall

-Pressure of the gas phase

-Temperature

-Crystallographic structure of the metal phase

-Concentration of diffusing substance upon the diffusion coefficient

-Grain size of the metallic phase

-Cold work and strain applied to the metallic structure

-Composition (and thus structure) of steel

Effects of Composition and Structure. Of all the common metals α-iron shows the maximum hydrogen permeability (at $0°C$). Some alloys of iron have greater permeability still, some of the principal additions and their known effects are listed bellow.

---

[12] The usefulness of this formula is relatively small for real gas-metal systems as one rarely knows the true concentration c_i or if D is independant of c.

a.) Carbon. The general statement is that the presence of carbon considerably diminishes the hydrogen permeation rate, and that the structural form of cementite greatly influences the permeability.

b.) Manganese. No clear indications can be found, it seems to play a small part in the flow of hydrogen through steel.

c.) Silicon. The general conclusion is that this element greatly diminishes the permeability.

d.) Sulfur and Phosphorus. The effects of these two elements are secondary factors and influence the entrance mechanisms of hydrogen into the metal. They "poison" some catalytic reactions, the hydrogen recombination reaction $2H \rightarrow H_2$ among others. Furthermore, sulfur and phosphorus contained in iron or steel may act in a similar way to their compounds added to an acid solution, since, under the action of acid on the sulfide or phosphide inclusions present on the surface of the sample, H_2S and PH_3 are formed.

e.) Chromium. Up to a Cr content of 20 % the permeability is greatly reduced with increasing Cr content to a value which is considerably below the value for pure iron. Above 20 % Cr the permeation rate increases again with increasing temperature.

f.) Nickel. First, there is a sharp increase in permeability with increasing Ni content up to 6 %. After that, a gradual decrease with growing Ni content up to approximately 80 % Ni is observed.

g.) Chromium and Nickel. An example with 1 % Cr added to a 3.28 % Ni-alloy showed greatly decreased hydrogen permeability at room temperature.

h.) Molybdenum. A presence of 1 to 10 % Mo content has no appreciable effect on the permeation rate.

From the preceding subchapter and this chapter it can be seen that there are three different processes involved in obtaining a homogeneous solution of hydrogen in metal:

a.) Surface adsorption.

b.) Solution in the region immediately below the surface.

c.) Diffusion of the hydrogen through the metal.

Therefore, if adsorption, dissolution and diffusion of hydrogen in steel can not definitely be precluded by physical or chemical properties of the system, a certain amount of hydrogen can always be expected. The effects of hydrogen on the properties of the metal, i.e. embrittlement, are discussed in the following chapter.

A.6 Mechanism of Embrittlement of Steel by Hydrogen

In general the deformation of metals occurs by means of movement of dislocations along certain preferred directions (" slip directions ") within the individual crystals of the metal. Under these conditions, the moving dislocations tend to accumulate at barriers, such as grain boundaries or hard precipitate particles situated at the end of slip plains. Such an accumulation of dislocations can then lead to the formation of an embryo micro crack and/or intensive local stress concentration. These stresses can activate a neighboring set of dislocations (slip system), however, the harder the material and the lower the temperature, the higher the stress has to be to initiate this effect. Consequently, these high stresses can lead to the formation of micro cracks. The result of this is that the metal fractures in a brittle manner, after having sustained only a very small amount of plastic deformation. Temperature plays an important role in this mechanism, as the general resistance of a metal to plastic deformation is lower at higher temperature. Brittle fracture can be of two types:

a.) Intergranular fracture, which propagates around the grain boundaries of a poly-crystalline specimen.

b.) Transgranular- or cleavage-fracture, which propagates across a particular plane within a crystal.

In any case, the fracture originates from the initiation of a micro-crack, which has been formed by the above mentioned accumulation of dislocations. Hence, any change in the stress concentration and the formation of micro-cracks is likely to enhance the possibility of brittle-fracture.

The effect of hydrogen on the dislocation-slip model has been the cause of extensive research. Various explanations have been given, some seemingly fitting in better with known facts than others. One description that fits in well with the dislocation-slip model and is generally agreed upon by large parts of the metallurgical-scientific community is the following:

Hydrogen embrittlement arises as the result of the formation of micro-cracks in hydrogen-containing materials. The formation of the micro-crack takes place in one of two ways:

> 1.) The micro-crack forms due to severe internal strains caused by the stress-induced formation of a local concentration of hydrogen in interstitial solution.

> 2.) The micro-crack forms as a result of the embrittling effect of hydrogen-rich constituents within the grains or at the grain boundaries of metals (reaction of alloying components with hydrogen).

Stress induced formation of local concentrations of hydrogen in iron and steel can be explained with the trap binding energy E_B of a defect in the crystalline structure of the metal. If E_B is larger than the lattice migration energy E_M of hydrogen in iron, hydrogen gets " caught " in the trap sites. There are four categories of traps:

> 1.) Point defects with weak interactions. Some trapping of hydrogen occurs, however, only enough to influence but not enough to control hydrogen embrittlement.

> 2.) Point defects with moderate to strong interactions. Larger amounts of hydrogen are trapped, having a stronger influence on embrittlement.

3.) Dislocations with moderate to strong interactions. The influence on embrittlement are similar in magnitude to 2.).

4.) Grain boundaries, interfaces and surfaces with strong interactions. These are the strongest two dimensional traps in the structure of a metal and have the ability to keep substantial amounts of hydrogen.

Generally, interfacial traps have high saturabilities and are present in the largest densities in the more microstructurally complicated high strength steels, therefore making these the most susceptible to hydrogen embrittlement.

APPENDIX B

Information on Spreadsheet Used for the Model

B.1 General Information

The spreadsheet program used for the modeling process is " Lotus 1-2-3 Release 4 " by Lotus Development Corporation, 55 Cambridge Parkway, Cambridge, MA 02142. This program runs in the graphical operating environment of " Windows 3.1 " by Microsoft Corporation, One Microsoft Way, Redmond, Wa 98052. It allows easy manipulation of numerical values, modifications can often be made with simple " Drag and Drop " technique. Files from other spreadsheet programs (e.g. " Excel " and " Symphony ") and earlier versions of Lotus 1-2-3 can be imported.

B.2 Example of the Spreadsheet

In the following, an example of the spreadsheet for the base case described in chapter 4 has been printed out. The first seven rows are for data input, the values for m, L and μ_{res} ("MuRes") are calculated from the input values. The figures are based on the resulting values in the vertical columns for N_{eH} ("N-e") and N_e without hydrogen ("Without H: N-e").

R2	R1	R0	MuFe	MuH	MuH2O	RoFe·	RoH2O	Obj.Width
10	9.05	9	0.15	22	15	7.88	1	10
p	N-Zero	Hor.Pixel-#	Pix-H.Size	CD-H.Siz	f-lens	N-Gamma		Obj.Height
200	5000000	1024	15	1.536	1	170000		10
		Vert.Pixel-#	Pix-V.Size	CD-V.Size				
		1024	15	1.536				

e_d	e_l	e_q	m	L
0.15	0.85	0.3	6.510417	0.004432
MuRes				
0.15437				

x	y-1	y-2	y-3	N-i(x)	N-itot(x)	Photscint	P-tot	P	N-e
0	0	0	0	5000000	5.0E+08	1.3E+13	2.0E+12	1941595	582478.6
0.05	0.998749	0	0	471608.9	47160890	1.2E+12	1.9E+11	183134.7	54940.42
0.1	1.410674	0	0	178102.8	17810278	4.5E+11	7.3E+10	69160.7	20748.21
0.15	1.725543	0	0	84606.29	8460629	2.2E+11	3.4E+10	32854.23	9856.27
0.2	1.989975	0	0	45281.23	4528123	1.2E+11	1.8E+10	17583.56	5275.069
0.25	2.222049	0	0	26161.01	2616101	6.7E+10	1.1E+10	10158.82	3047.646
0.3	2.431049	0	0	15961.71	1596171	4.1E+10	6.5E+09	6198.238	1859.471
0.35	2.622499	0	0	10151.34	1015134	2.6E+10	4.1E+09	3941.96	1182.588
0.4	2.8	0	0	6672.491	667249.1	1.7E+10	2.7E+09	2591.055	777.3166
0.45	2.966058	0	0	4506.1	450610	1.1E+10	1.8E+09	1749.805	524.9414
0.5	3.122499	0	0	3113.058	311305.8	7.9E+09	1.3E+09	1208.86	362.6579
0.55	3.270703	0	0	2192.956	219295.6	5.6E+09	8.9E+08	851.5668	255.47
0.6	3.411744	0	0	1571.184	157118.4	4.0E+09	6.4E+08	610.1206	183.0362
0.65	3.546477	0	0	1142.617	114261.7	2.9E+09	4.7E+08	443.7	133.11
0.7	3.675595	0	0	842.0517	84205.17	2.1E+09	3.4E+08	326.9847	98.09542
0.75	3.799671	0	0	627.9912	62799.12	1.6E+09	2.6E+08	243.8609	73.15828
0.8	3.919184	0	0	473.4273	47342.73	1.2E+09	1.9E+08	183.8409	55.15226
0.85	4.034538	0	0	360.4307	36043.07	9.2E+08	1.5E+08	139.9621	41.98863
0.9	4.146082	0	0	276.887	27688.7	7.1E+08	1.1E+08	107.5205	32.25615
0.95	4.254116	0	0	214.4806	21448.06	5.5E+08	87332630	83.28689	24.98607
1	3.408899	0.95	0	156.8177	15681.77	4.0E+08	63853336	60.89529	18.26859
1.105	2.901576	0.297018	1.370757	3.5E-15	3.5E-13	9.0E-09	1.4E-09	1.4E-15	4.1E-16
1.1	2.918721	0.302975	1.337909	8.9E-15	8.9E-13	2.3E-08	3.6E-09	3.5E-15	1.0E-15
1.15	2.763821	0.255782	1.636307	1.9E-18	1.9E-16	4.8E-12	7.6E-13	7.3E-19	2.2E-19
1.2	2.637274	0.225667	1.886796	1.5E-21	1.5E-19	3.8E-15	6.0E-16	5.7E-22	1.7E-22
1.25	2.530385	0.204307	2.106537	2.8E-24	2.8E-22	7.0E-18	1.1E-18	1.1E-24	3.2E-25

Without H

N-i(x)	N-itot(x)	Photscint	P-tot	P	N-e	Delta N-e
5000000	5.0E+08	1.3E+13	2.0E+12	1941595	582478.6	0
471608.9	47160890	1.2E+12	1.9E+11	183134.7	54940.42	0
178102.8	17810278	4.5E+11	7.3E+10	69160.7	20748.21	0
84606.29	8460629	2.2E+11	3.4E+10	32854.23	9856.27	0
45281.23	4528123	1.2E+11	1.8E+10	17583.56	5275.069	-4.4E-16
26161.01	2616101	6.7E+10	1.1E+10	10158.82	3047.646	0
15961.71	1596171	4.1E+10	6.5E+09	6198.238	1859.471	-3.3E-16
10151.34	1015134	2.6E+10	4.1E+09	3941.96	1182.588	0
6672.491	667249.1	1.7E+10	2.7E+09	2591.055	777.3166	-1.7E-16
4506.1	450610	1.1E+10	1.8E+09	1749.805	524.9414	0
3113.058	311305.8	7.9E+09	1.3E+09	1208.86	362.6579	0
2192.956	219295.6	5.6E+09	8.9E+08	851.5668	255.47	0
1571.184	157118.4	4.0E+09	6.4E+08	610.1206	183.0362	-2.8E-17
1142.617	114261.7	2.9E+09	4.7E+08	443.7	133.11	0
842.0517	84205.17	2.1E+09	3.4E+08	326.9847	98.09542	0
627.9912	62799.12	1.6E+09	2.6E+08	243.8609	73.15828	0
473.4273	47342.73	1.2E+09	1.9E+08	183.8409	55.15226	-3.5E-18
360.4307	36043.07	9.2E+08	1.5E+08	139.9621	41.98863	-3.5E-18
276.887	27688.7	7.1E+08	1.1E+08	107.5205	32.25615	0
214.4806	21448.06	5.5E+08	87332630	83.28689	24.98607	-1.7E-18
167.421	16742.1	4.3E+08	68170810	65.01275	19.50383	1.235239
3.6E-15	3.6E-13	9.2E-09	1.5E-09	1.4E-15	4.2E-16	8.5E-18
9.1E-15	9.1E-13	2.3E-08	3.7E-09	3.5E-15	1.1E-15	2.2E-17
1.9E-18	1.9E-16	4.9E-12	7.8E-13	7.4E-19	2.2E-19	3.9E-21
1.5E-21	1.5E-19	3.8E-15	6.1E-16	5.8E-22	1.8E-22	2.7E-24
2.8E-24	2.8E-22	7.1E-18	1.1E-18	1.1E-24	3.3E-25	4.5E-27

131

APPENDIX C

C.1 Graph of Mass Attenuation Coefficients for Various Elements
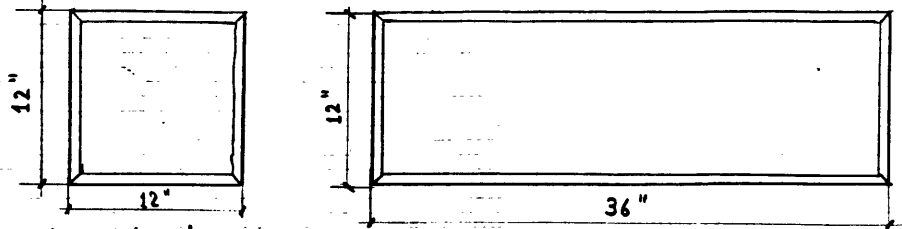
The mass attenuation coefficients are given for monoenergetic X-rays (lines) and for thermal neutrons (points).
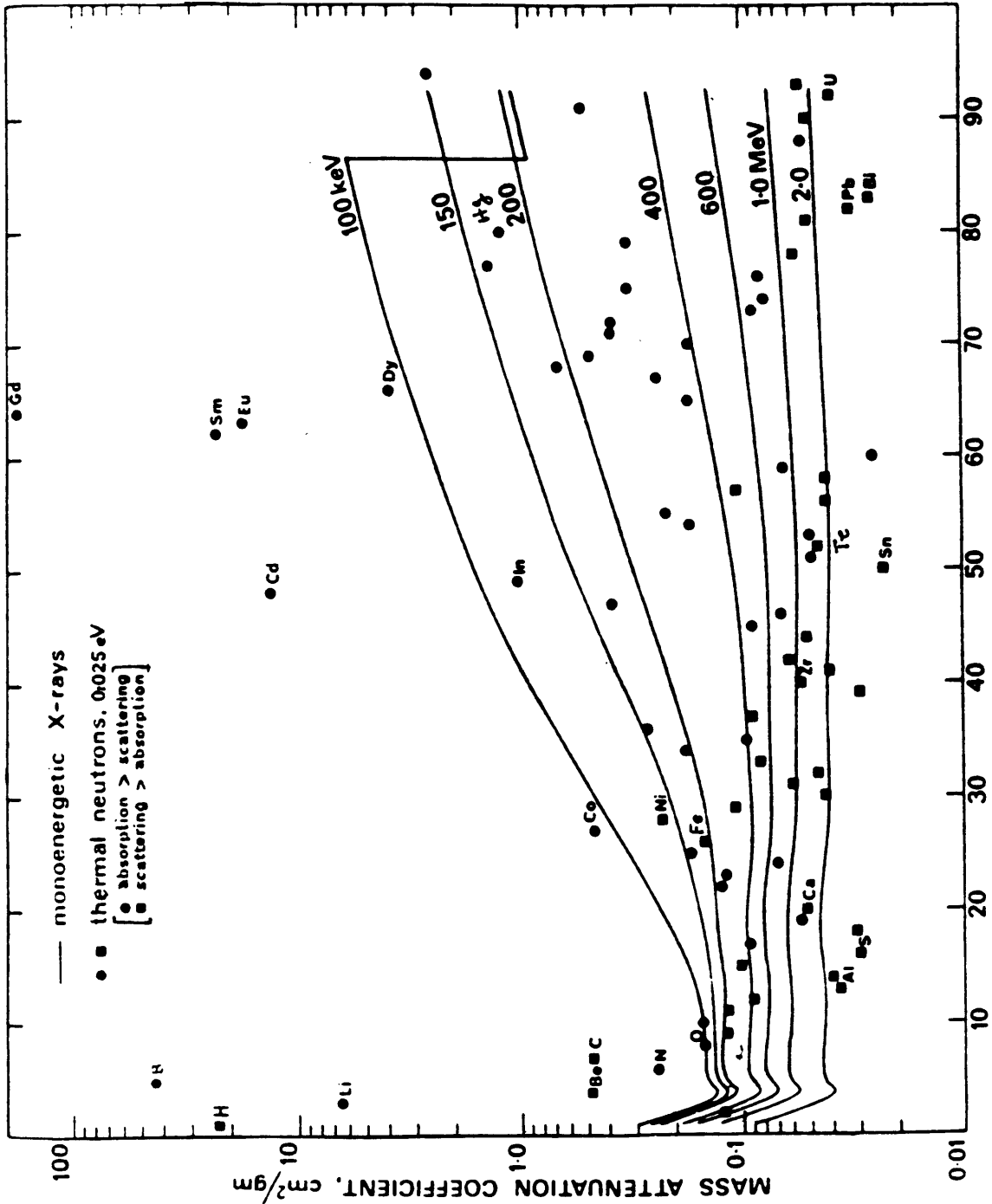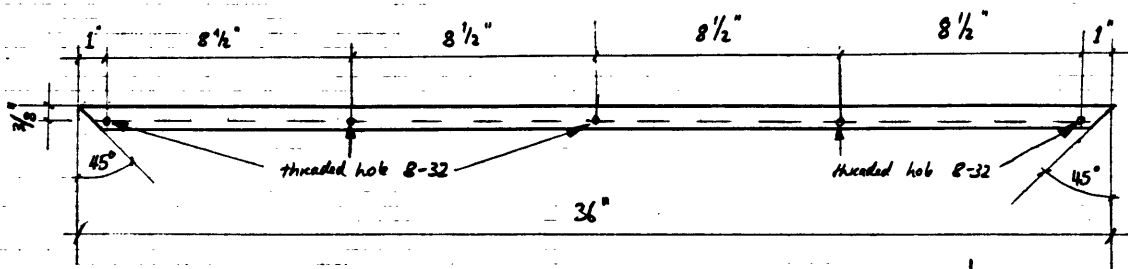
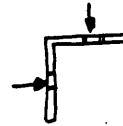## APPENDIX D

Construction Sketches for Aluminum Box

Aluminium Frame :

Welded at corners.
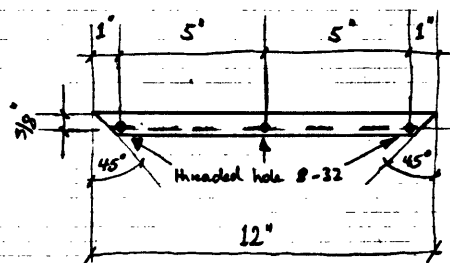
Made up out of $1/8 \times 3/4 \times 3/4$ profile :   4 pieces length 36" :

→ 8-32 threaded holes on both sides of L-profile
at same positions.

8 pcs length 12" :

→ 8-32 threaded holes on both sides of
L-profile at same position.

AL- plates

Thickness   0,050

4 pcs :   36" long × 12" high
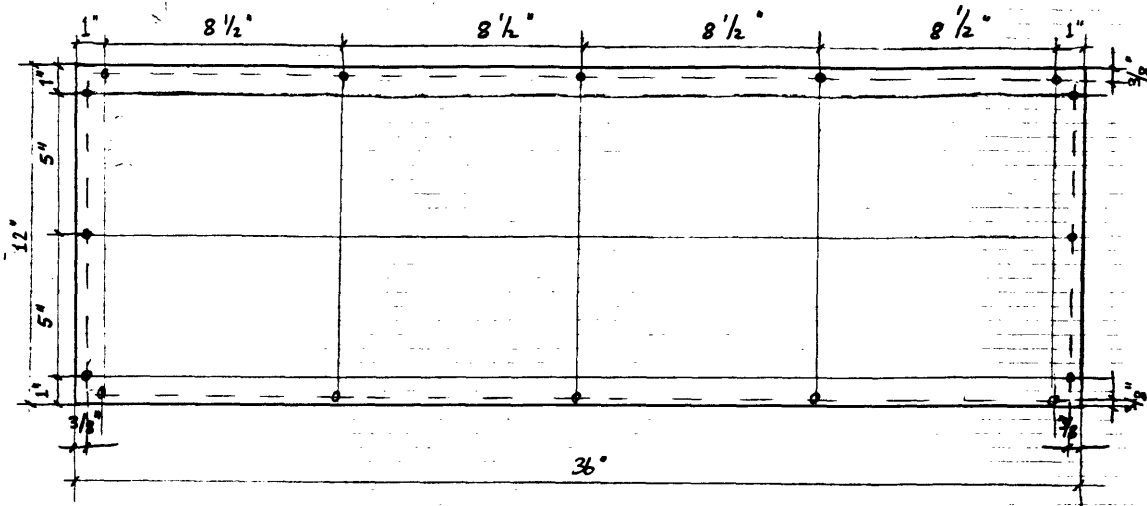
2 pcs :   12" long × 12" high
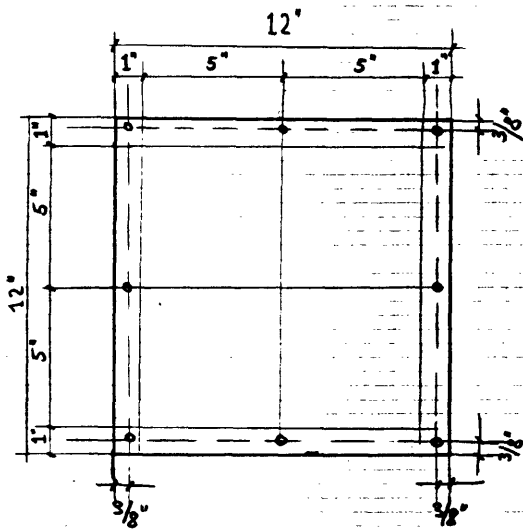
Diam. of all holes: 3/16"

134

Addtl. pieces of Al - L - profile

6 pcs :   11" long long .

```
┌─────────────────────────┐
├─────────────────────────┤
│          11"            │
└─────────────────────────┘
```
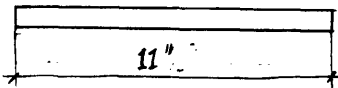
Addtl. piece of Al - plate :   (Thickness of other plates)

1 pcs :   12" long × 11 5/16" high

Material: Weldable AL   6061-T6 for frame
             AL 5052-H32 for plates

Ordered from: Pierce Aluminum Co., Inc.
                136 Will Drive
                P.O. Box 100
                Canton, MA 02021
                (617) 828-9005

PO #: GP-D- 393641

Info for using plastic screws 8-32 × ½":

In two opposing screw holes on profile, one screw has to be shortened

short screw

Technical Specifications for Princeton Instruments ST-138 Camera Controller and EEV CCD-Camera

ST-138

High Performance CCD Camera Controller

Overview

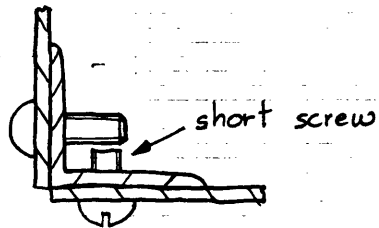The Model ST-138 is the highest performance CCD camera controller available from Princeton Instruments. Designed for demanding image acquisition, its key parameters are:

- Up to 12 bits/pixel at 1 MHz
- Noise 1-1.3 A/D counts RMS
  (total system, including detector)
- 1% Linearity
- Dual A/D converters:
  1 MHz A/D optimized for focusing and alignment
  Slower A/D optimized for high precision
- Individual pixel control for sophisticated readout:
  Full image at full resolution
  Subimaging
  N x M On-chip charge binning
  Patterned row and column skipping
  Frame transfer mode
  Kinetics mode: Ultra-fast readout of subimages. 1 μsec to > 100 μsec per line shift, dependent on CCD.
- Programmable delay between shift bursts.
  For example: Acquire 8 images of size 144 x 298 in 8 msec at 16 bit resolution.
- High speed dark current cleaning, < 1 msec/frame on some CCDs
- Sophisticated triggering and synchronization
- High speed burst DMA data transfer to main memory on IBM/AT or Macintosh computers.
- Special hardware for fast image display in a window on your computer screen. Our Microsoft* Windows™ based software supports:
  Digital intensity autoscaling
  Frame by frame live operation at full speed
  Linear and nonlinear intensity scaling
- Power for thermoelectric cooling, with ±0.050°C thermostating.
- Supports a wide variety of cooled CCD cameras:
  512 x 512 to 3,072 x 2,048
  Standard or MPP operation
  Thermoelectric or LN cooled
  Intensified CCD cameras, 18 or 25 mm intensifiers.
- Auxiliary digital and analog I/O, for complete experiment integration, all under software control.

A/D Converters and Architecture

It is often desirable to switch the operation of a scientific CCD camera quickly between two speeds. High speed operation is useful for focusing, alignment, and fast data collection. Lower speed operation is useful for achieving the lowest noise and highest dynamic range possible. Each speed has its own analog circuitry requirements and it is difficult to design a system that operates at both speeds without compromising.

To solve this problem without compromising either mode of operation, the ST-138 Controller has been designed to support two A/D converters, one "fast" and one "slow," each with its own optimized analog circuitry. The controller can switch back and forth between these two A/D converters almost instantly, under software direction. A/D converter combinations are listed in the table below.

Fast	Slow
1 MHz, 12 bits	430 kHz, 16 bits
1 MHz, 12 bits	None
500 kHz, 12 bits	150 kHz, 16 bits
500 kHz, 12 bits	None
430 kHz, 16 bits	150 kHz, 16 bits
430 kHz, 16 bits	None
None	150 kHz, 16 bits

A/D converter speed and precision describe the A/D converter only. System performance depends on the capabilities of the camera head as well. Not all CCD arrays can run at these speeds and provide more than 12 bits of precision.

The 12 bit 500 kHz and 16 bit 430 kHz A/D converters can be set to operate at 200, 100, or 50 kHz by selection of analog circuits under software control. Slower speeds offer substantially improved signal to noise operation.

The 150 kHz, 16 bit A/D converter can also be set to operate at 150 kHz or, by selection of analog circuits under software control, at 100 or 50 kHz, effectively trading speed for reduction of noise.

Cameras Supported

All Princeton Instruments CCD cameras can be operated with the Model ST-138. The following Princeton Instruments cameras are available for operation at 1 MHz.

- Kodak 768 x 512
- Kodak 1317 x 1035
- Kodak 2044 x 2033
- Kodak 3072 x 2048
- EEV 576 x 384

The detectors below operate at up to 500 kHz:

- Tektronix 512 x 512 front or back illuminated
- Tektronix 1024 x 1024 front illuminated
- EEV 1152 x 1242
- Thomson 576 x 384

Princeton Instruments also offers fiber coupled intensified CCD cameras based on the 576 x 384 arrays listed above, and lens coupled intensified CCD cameras based on any of the arrays listed above.

New cameras are constantly being added to this list. Contact your Princeton Instruments representative for up-to-date information.

Temperature Control

The ST-138 Controller provides power and control for thermoelectric cooling of PI CCD detectors. Front panel LEDs indicate when the temperature is fully regulated.

Precise subtraction of dark current is a key factor in many applications. To be able to subtract dark current precisely, its level must not fluctuate between measurement of the dark current level and measurement of the image. Because the dark current of most CCD arrays is an exponential function of temperature, doubling roughly every 4-7°C, precision temperature regulation is crucial. The ST-138 Controller regulates the temperature of the CCD array to ±50 millidegrees over the full operating temperature range. This translates into dark current stability of ±½% or better on most arrays.

Timing Modes

The timing mode used determines when an exposure is taken. The Model ST-138 supports the following timing modes:

Freerun

In this mode, the camera continuously reads out frames. The controller will continue to read out frames until the software instructs it to stop.

External Sync

This mode is similar to Freerun except that each time the camera is ready to begin an exposure, it waits to receive an external signal. Once this signal is received, the system waits for the duration of the preset exposure time, closes the shutter, and reads out the CCD. The shutter can either be opened before or after the external pulse is received.

External Trigger

This mode is similar to External Sync, except that the CCD goes into continuous fast clear operation while waiting for a trigger. When a trigger arrives, the row shift currently in progress (if any) is completed (typically a few microseconds, depending on the CCD array) and then shifting stops for the duration of the preprogrammed exposure period. This mode avoids the buildup of dark current and makes the dark current reproducible (which allows measurement and subtraction).

Store-Enable Triggering

Another trigger input can be used to determine whether data is to be stored. This allows a camera to be run continuously, storing frames asynchronously, i.e., only when an event has occurred during a readout/exposure cycle.

On-Chip Charge Binning Control

Rows:

During each frame digitizing cycle, each row of the CCD is shifted "vertically" into the serial shift register of the CCD. If another row has previously been shifted into the serial shift register and not read out, then the charge of the new line will be combined with the charge already there. This is called row binning.

In the ST-138 Controller, as few as one or as many as all rows can be binned together. In addition, unwanted data can be read without digitizing. This "skipping" is much faster than readout with digitizing.

Columns:

Once the correct number of rows have been shifted in parallel into the serial register of the CCD, the register is read out. This is done by clocking the serial register once for each pixel. When the charge in a given pixel is shifted out the end of the serial register, it enters a charge detecting capacitor. Here it can either be dumped (the pixel is skipped), digitized, or binned (for later digitizing).

Readout Mode Options

The flexible programming of the ST-138 allows the following common readout modes:

a) Readout and digitization of the whole array at full resolution.

b) Readout and digitization of a rectangular subsection of the array at full resolution. This results in a much higher readout rate and is useful for focusing.

c) Readout with N x M binning. This reduces resolution but increases the readout rate. Because N x M binning combines the charges from many pixels, the apparent sensitivity of the camera is increased, allowing shorter exposure times to be used.

d) Readout and digitization of rectangular bands of pixels, binned to give a one dimensional output. This mode of readout offers fast cross section readouts.

138

e) Readout with patterned row and column skipping. This allows the whole CCD or any part of it to be read out with lower resolution, but without binning. When working with live images, this allows you to zoom in and out on a big CCD array without changing exposure levels to compensate for binning. It also allows a large CCD array to be read out to a window on your computer screen, at a frame rate of that is determined by the window size and not by the CCD size. For focusing and alignment, this keeps the frame rate high, even as you zoom in and out on the image.

Readout Time Examples

The total readout time is a combination of several factors, including time to shift charge on the CCD array and time for digitization. Example readout times at 1 MHz are as follows.

576 x 384 Intensified CCD:
Full image at full resolution: 250 msec
Full image, binned 4 x 4: 26 msec
100 x 100 subimage at full resolution: 15 msec

3072 x 2033 CCD:
Full image at full resolution: 6.3 sec
Full image binned 8 × 8 (e.g., for alignment): 0.2 sec

In gated intensified systems, the CCD exposure time will generally be longer than the gate time, particularly if the light from multiple gate pulses is to be accumulated on the CCD array.

Array Cleaning Modes

When not acquiring data, the controller automatically cleans dark current from the CCD.

During acquisition, there are not normally any cleans between frames. There is however an Asynchronous mode for cleaning between digitized frames. The number of cleans is programmable.

Cleaning is a form of array readout in which all rows and columns are skipped. Two alternative strategies for charge binning during clean cycles are discussed below.

If the controller is programmed to bin all rows of the CCD and then sweep out their charge in one pass of the serial shift register, the "frame rate" of cleaning will be the highest. Depending on the vertical shift time possible with a particular CCD array, the time for each clean frame can be as low as 1 msec.

If instead, rows are binned in smaller groups and then clocked out of the serial register, the "frame rate" of cleaning may be slower, but the charge capacity of cleaning may be higher (e.g., for detectors without shutters). This mode is often recommended for cleaning an array from previously recorded intense images, as the faster mode may not clean the array completely.

Frame Transfer Operation

The ST-138 Controller supports operation of CCD detectors in frame transfer mode, where the array is divided into two equal sections. The area next to the serial shift register is called the "storage" area. The other area is the "image" area. The storage area is usually masked, either by aluminization on the CCD, a mechanical mask close to the CCD surface, or by design of the optics in front of the camera. Light falls on the image area only.

After each exposure period, the charge in the image area is rapidly shifted to the storage area. Once this is done, the next exposure period begins. During this exposure, the charge in the storage area is read out (only the storage area of the CCD is clocked).

Frame transfer operation allows readout to be overlapped in time with exposure, so the exposure duty cycle can become 100%, a sensitivity advantage when taking sequences of images or for continuous operation.

Frame transfer operation also allows pairs of exposures to be made fairly closely spaced in time. Spacing depends on the time required to shift the charge from the exposure area to the storage area, which can be less than 1 msec.

In intensified CCD detectors, the phosphor of the intensifier may have a decay time of several milliseconds. If this is unacceptable, PI offers a high speed phosphor option that reduces the decay time to under 1 μsec.

The ST-138 provides support for shutter operation with a frame transfer detector. If the exposure time is less than the readout time, then the controller will close the shutter to prevent excess exposure. In addition, even if no physical shutter is present, a non-zero "shutter close time" can be programmed. With it, the pause after the exposure can be used to let phosphors decay before readout of the CCD.

Kinetics Mode Operation

Charge can be shifted on a CCD array much faster than it can be read out with high precision. If all of a CCD is in darkness except for a small illuminated region, then multiple exposures can be made in fast sequence in the illuminated region, with just enough time between these exposures to shift the charge aside. When the whole CCD area is filled with these images, it can then be read out with high precision. This allows a burst of images to be taken at very high frame rates, while providing the high sensitivity, low noise, and high dynamic range of a slow-scan CCD camera. Normal high speed cameras cannot come anywhere close to this.

The ST-138 Controller first executes a sequence of shift bursts interleaved with exposure periods. Charge shift rates can be programmed to be from 0.6 to 9.6 μsec per line. Note however that not all CCD arrays can keep up with high vertical shift rates. The number of lines to be shifted

in each burst is usually set to the number of lines that are illuminated (with perhaps a little extra for spacing). The exposure periods can be from 0 to 3 sec, programmable in increments of 200 nsec. Because the high speed is beyond the capability of the mechanical shutter, no attempt is made to close the shutter between bursts.

An example of this mode is found in the Princeton Instruments data sheet *Very High Speed CCD Cameras*.

Special Hardware for Fast Image Display

In a high dynamic range camera, pixels are digitized to 12-16 bits of precision. Since most image displays only show 8 bits of gray scale depth, there is a need to map the high precision data to 8 bits for display. To determine what range in the 16 bit data is to be mapped to 8 bits, the system usually determines the minimum and maximum pixel values and scales between them. When done in software, this determination of min and max, followed by intensity mapping, can take several seconds per image. Historically, high dynamic range CCD cameras were therefore impractical for real time imaging, and difficult even to focus or align.

The ST-138 Controller solves this problem with digital circuitry to compute the min and max value of each frame in real time, and with a downloadable lookup table to convert pixel data, also in real time, from 16 bit format to 8 bits. This allows images to be displayed on computer screens in real time, with digital intensity autoscaling. Because the process is entirely digital, it does not introduce any noise (as analog gain controls can). Because the min and max are determined exactly, the entire dynamic range of the display can be used.

This digital approach is also better than an analog gain-control scheme because the scaling is known precisely: there is no question of calibration of the relative analog gain levels. The researcher is also not limited to a few fixed gain levels provided by the manufacturer or to the unknown calibration of a variable analog gain control.

Because it is so fast, this mechanism can be used to adjust the intensity scaling on every frame, for automatic image-by-image optimization. Because the mapping is controlled by the computer, absolute intensity information is not lost, as it is when analog cameras automatically set their own gains.

Accumulator

An optional card for the ST-138 allows data to be full-frame accumulated in the hardware of the controller. Up to 32 bits/pixel can be accumulated before data is read to the computer. Using this feature statistically increases S/N, while allowing data to be read at full speed.

Computer Interface

The ST-138 Controller has a high speed burst mode DMA interface that can sustain data transfers to IBM AT compatible computers at 2 Mbyte/second. Use of DMA means that the amount of data that can be taken is limited only by the memory capacity of the computer. The data is also immediately accessible to the microprocessor, for real time display or analysis.

ST-138 operation has been verified on ISA computers at 500 kilopixels/sec and EISA computers at 1 Mpixels/sec. The DMA circuitry of EISA computers, even when operating in ISA compatibility mode, is more efficient. This allows higher data rates and more computation to be done while data is being taken.

A high speed serial interface has been developed for use with AT, Macintosh, and other computers. This interface allows separation of the controller and the computer up to 100 ft. A fiber optic link increases this distance to 2 km.

Not all computers that claim to be 100% IBM AT compatible actually are. Princeton Instruments maintains a list of computers that have been verified for operation with its equipment. Consult your sales representative for specifics.

Peripheral I/O

Synchronization and/or control signals:

- External sync input: TTL low; up to $(1/t_{frame})$ Hz
- External shutter control input: TTL low to open
- Trigger output: TTL low at the start of data acquisition
- Notscan output: TTL high during exposure, low during readout
- Frame, line, and pixel clocks: TTL outputs
- Shutter drive monitor: TTL output, high during active shutter drive
- I/O inputs: 8 TTL lines
- Digital outputs: 8 TTL output, 4 inverted, 4 high voltage capable (60 V, 0.5 A switches)
- Analog input (optional): One input, 0 to +10 V used for normalization, e.g., compensating for light source variation.

Software

Princeton Instruments offers its WinView software package, based on Microsoft Windows, to operate the ST-138 Controller for imaging applications on IBM/AT computers. The IPLab Spectrum software is offered for operation on Macintosh computers. Separate brochures describe these software packages in detail. **PI**

These cameras utilize large format, high pixel density (close to 1.5 mega pixels) CCD arrays specifically designed for high resolution imaging. The large size pixels with their large well capacity ensures maximum light collection (with low f/no. optics) and wide linear dynamic range.

PI selects arrays of the highest grade in order to provide the utmost in performance: i.e., low blemish rate, maximum well capacity, lowest dark charge and readout noise, high sensitivity, minimum non-uniformity, and long term stability.

These cameras are operated by all Princeton Instruments universal controllers with interfaces to various computers. Various optical interfaces are available including microscope attachments and lens mounts. Customized interfaces can be developed upon request.

PERFORMANCE CHARACTERISTICS:

CCD Array:	EEV model 05-30, both standard and MPP versions
Format:	1152 x 1242 (26x28mm) each pixel 22.5 x 22.5μm
Full Well Capacity:	Standard Device: $\geq$500,000 electrons
	MPP Device: $\geq$200,000 electrons
Readout Noise:	4-6 electrons rms @ 50 KHz
	8-11 electrons rms @ 200 KHz
Spectral Range:	400-1080 or 190-1080 with UV-to-VIS conversion coating
Dynamic Range:	14-17 bits
Response Non-Linearity:	< 2% standard deviation for 18 bits
	<1% standard deviation for 14-16 bits
Response Non-Uniformity:	$\leq$+/- 3% over entire CCD area except for blemish regions
Blemish Specifications:	Maximum Number of Defects:
	Points: $\leq$20
	Clusters: $\leq$3
	Columns: $\leq$1
	Partial columns: $\leq$2
	Lower grade devices are available on request.
	Please call the factory for details.
Operating Temperature:	TE/CCD: -60°C with tap water circulation
	-70°C with coolant (<10°C) circulation
	-50°C with air fan circulation
	LN/CCD: -70°C to -130°C
Thermostating Precision:	+/- 40 millidegrees C over entire temperature range.
Typical Dark Charge:	TE/CCD @ -60°C: <1 e-/pixel-second for standard CCD
	<0.005e-/pixel-second for MPP CCD
	LN/CCD @ -120°C: <0.00015e-/pixel-second for std. CCD.

Princeton Instruments, inc.

Scan Rate: 25, 100 KHz user selectable (14 to 17 bits)
                        20 to 200 KHz user selectable (14 or 16 bits)
                        50 KHz to 500 KHz user selectable (12 or 14 bits)

Readout Time: Full Image: 8.1 second @ 200 KHZ
                                  3.3 second @ 500 KHz
                        Example: Reduced image resolution via binning 3x3:
                                        1.1 seconds @ 200 KHz
                                        0.58 seconds @ 500 KHz

SPECTRAL RESPONSE OF FRONT ILLUMINATED CCDs

FRONT-ILLUMINATED

QUANTUM EFFICIENCY (%)

WAVELENGTH (nm)

* WITH UV—COATING